

PICOSECOND AND SUBPICOSECOND OPTICAL
PROPERTIES OF GaAs/Al_xGa_{1-x}As QUANTUM
WELLS AND SUPERLATTICES

By

ABDELLATIF BOUCHALKHA

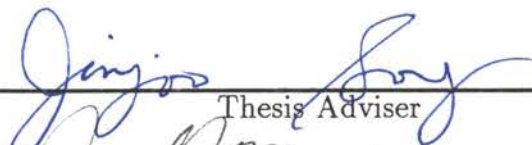
Bachelor of Science
Central State University
Edmond, Oklahoma
1986

Master of Science
Oklahoma State University
Stillwater, Oklahoma
1989

Submitted to the Faculty of the
Graduate College of the
Oklahoma State University
in partial fulfillment of
the requirements for
the Degree of
DOCTOR OF PHILOSOPHY
May, 1993

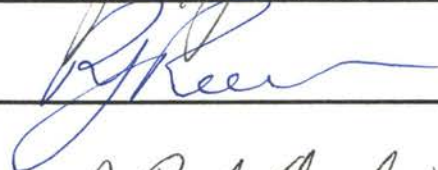
PICOSECOND AND SUBPICOSECOND OPTICAL
PROPERTIES OF GaAs/Al_xGa_{1-x}As QUANTUM
WELLS AND SUPERLATTICES

Thesis Approved:

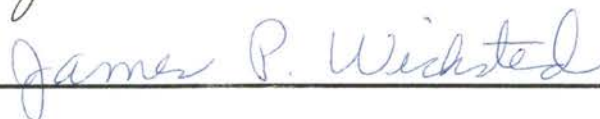



Thesis Adviser











Dean of the Graduate College

ACKNOWLEDGMENTS

I would like to acknowledge the help and support of several people without whom this work would not have been possible. At first, I would like to sincerely thank my thesis advisor, Dr. Jin-Joo Song, for giving me the opportunity to work and collaborate with her. I am very grateful to her for the continued support, training, advice, and guidance to name just a few. Special thanks and appreciation are also extended to my other thesis committee members, Dr. James P. Wicksted, Dr. Joel J. Martin, Dr. Roger J. Reeves, and Dr. J. Paul Devlin. I am deeply in debt to Dr. Dai-Sik Kim at AT&T Bell Lab. for the many hours of fruitful discussions and collaborations. I like to thank Dr. John F. Klem at Sandia National Lab. for kindly providing us with the many samples required for this study. Extended thanks go to all members of our group and office mates.

More importantly, I am very grateful to God, my Mom, and my Dad for their blessings. Special thanks are extended to my brothers, sisters, family members and friends for their constant support. This work is dedicated to my mother Fatna and my father Boujemaa.

Financial support for this work was provided by the Office of Naval Research and the Department of Energy.

TABLE OF CONTENTS

Chapter	Page
I. INTRODUCTION	1
II. SAMPLE DESIGN AND PREPARATION	4
Growth Method	4
Sample Structures	6
Sample Preparation	10
III. EXPERIMENTAL METHODS	11
Picosecond Raman Scattering	11
Pulse Width Measurements	16
Picosecond Raman Setup	19
Degenerate Four Wave Mixing (DFWM)	22
IV. THEORETICAL BACKGROUND	27
Bulk GaAs	27
Rate Equations	27
Fröhlich Interaction	30
Intervalley Scattering	31
Nonparabolicity	33
Phonon Models in GaAs/Al _x Ga _{1-x} As QW's	34
Slab Model	35
Guided Mode Model	37
Huang and Zhu Model	37
Microscopic Models	38
Hot Electron Cooling in GaAs/Al _x Ga _{1-x} As QW's	39
Carrier-Carrier Cooling	39
Carrier-Phonon Cooling: Fröhlich Interaction	40
Carrier-Phonon Cooling : Deformation Po- tential Scattering.	43
V. CONFINED-TO-PROPAGATING LO PHONON TRANSITION	44
Introduction	44
Phonon Confinement	45
Experimental Results	49
Discussion and Conclusions	56

Chapter	Page
VI. LO PHONON PENETRATION DEPTH MEASUREMENTS . . .	62
Introduction	62
Experimental Results	63
Discussion and Conclusions	70
VII. QUANTUM BEATS AND EXCITON DEPHASING MEASUREMENTS	74
Introduction	74
Experimental Results and Discussion	75
Quantum Beats	80
Wavelength Dependent DFWM Lineshapes	83
Power Dependence of DFWM Signal	87
Temperature Dependence of DFWM Signal	87
ZnSe Epilayer results	91
Conclusions	98
VIII. SUMMARY	99
BIBLIOGRAPHY	101
APPENDICES	107
APPENDIX A - REMOVING THE GaAs SUBSTRATE	108
APPENDIX B - DETAILS ON THE PUMP AND PROBE EXPERIMENT	110

LIST OF TABLES

Table		Page
I.	List of parameters describing our GaAs/Al _x Ga _{1-x} As samples. The samples with (*) are pairs grown at different times for comparisons	9

LIST OF FIGURES

Figure	Page
1. Essential components of an MBE machine	5
2. Typical band diagram of GaAs/Al _x Ga _{1-x} As quantum wells	7
3. Schematic representation of the structure of our samples	8
4. A schematic diagram of the pulse compressor	12
5. Spectra of the dye laser pulses	14
6. Femtosecond dye laser cavity and spacial filter	15
7. Schematic diagram of the autocorrelator	17
8. Autocorrelation trace of our laser pulses	18
9. Picosecond Raman scattering setup	20
10. DFWM experimental setup	23
11. Ti:Sapphire laser output power and pulse width as a function of wavelength tuning	25
12. A schematic representation of our substrate-removed SL sam- ple	26
13. A schematic representation of the GaAs band structure	32
14. A comparative diagram of the displacement and potentials from different phonon models	36
15. Phase space distribution of the phonon occupation in a QW	41
16. Phase space distribution of the phonon occupation in bulk GaAs	42
17. Phonon dispersion curves for bulk GaAs, bulk AlAs, and GaAs/AlAs SL illustrating the Brillouin zone folding	46

Figure	Page
18. Typical Stokes and anti-Stokes picosecond Raman spectra	50
19. N_q versus laser power for bulk GaAs and two QW samples	53
20. Hot phonon generation rate as a function of L_b for $x=0.4$ and $x=1$ series	54
21. Hot phonon generation rate at two different excitation energies for $x=0.4$ series	57
22. Picosecond Raman scattering Stokes (a) and anti-Stokes (b) spectra obtained from a sample with $x=0.2$ and $L_z=L_b=70 \text{ \AA}$. The arrows indicate the AlAs-like modes	64
23. The generation rates of GaAs LO phonons plotted as a function of L_b for $x=0.3$ series	66
24. Hot phonon generation rates of the GaAs LO phonons as a function of L_b for several series of samples with $x < 0.3$	67
25. A plot of the GaAs LO phonon penetration depth λ into the $\text{Al}_x\text{Ga}_{1-x}\text{As}$ barriers as a function of x	69
26. PLE data of our GaAs/ $\text{Al}_{0.3}\text{Ga}_{0.7}\text{As}$ sample together with our laser pulse spectrum	76
27. DFWM signal as a function of the time delay between the pump and probe pulses	77
28. Diffracted signal showing quantum beats between HH and LH excitons	81
29. Log scale plot of the DFWM signal as a function of excitation energy detuning from the HH resonance	84
30. Linear scale plot of the DFWM signal as a function of energy detuning from the HH resonance	85
31. Log scale plot of the DFWM signal lineshape at several laser powers .	88
32. Linear plot of the DFWM signal as a function of the laser power . . .	89
33. DFWM signal lineshape at different lattice temperatures	90
34. Photoluminescence data of our ZnSe epilayer sample together with the laser pulse spectrum at two different energies	92

Figure	Page
35. DFWM signal from the ZnSe epilayer sample	94
36. Log scale plot of the ZnSe DFWM signal as a function of laser detuning from I_3 resonance	96
37. Linear scale plot of the ZnSe DFWM signal as a function of laser detuning from I_3 resonance	97
38. A schematic diagram of the pump and probe configuration used in DFWM experiments	111

CHAPTER I

INTRODUCTION

The optical properties of GaAs/Al_xGa_{1-x}As quantum wells (QW's) and superlattices (SL's) have been the subject of extensive investigations ever since the first fabrication of these heterostructures [1,2]. Optical spectroscopy is a nondestructive experimental method that allows for many repeated measurements on the same specimen. When a laser light beam with sufficient energy hits the sample many carriers in the sample are photoexcited to higher energy in the conduction band leaving behind holes in the valence band. After some elapsed time the carriers will eventually relax back to their ground state and recombine with the holes by emitting photons. This thesis concentrates mainly on the early stages of this relaxation process namely the first few picoseconds after excitation. We, therefore, study the ultrafast carrier dynamics and their properties in the GaAs/Al_xGa_{1-x}As semiconductor quantum wells (QW's) and superlattices (SL's).

Despite the continuing interest during the last decade, the dependencies of the properties of optical phonons on alloy composition in zincblende SL's and multiple quantum wells (MQW's) are still largely unknown. This is true even for such model systems as GaAs/Al_xGa_{1-x}As SL's and MQW's [4-7]. In the case of Al_xGa_{1-x}As barriers, alloy fluctuations make theoretical treatments of phonon properties rather complicated [5,8,9]. However, for the simpler GaAs/AlAs system optical phonon confinement has been demonstrated even when the GaAs wells are only a few monolayers thick [4,10,11]. Primarily because of the lack of information on LO phonon properties as a function of x, the so-called 2-dimensional (2-D) picture is routinely used to describe LO phonons and their scattering with electrons

in GaAs/ $\text{Al}_x\text{Ga}_{1-x}\text{As}$ quantum wells (QW's) [4,5]. Simply considering the limiting case of x or the barrier width approaching zero is enough to reveal the inadequacy of the 2-D picture [12–14]. In this study we will try to clarify some of the issues concerning the LO phonon nature and show that the GaAs LO phonons are not always confined as the literature implies. Instead, we show that the question of whether the LO phonons are confined or propagating should be answered carefully depending on the value of x and the thickness of the $\text{Al}_x\text{Ga}_{1-x}\text{As}$ barrier. This is important in the ultrafast device applications of these heterostructures since the primary relaxation mechanism of the carriers in these materials is through phonon emission.

The ultrafast relaxation of the carriers is also addressed on a much faster time scale than picosecond Raman scattering. In this case we use degenerate-four-wave-mixing (DFWM) to investigate the carrier and exciton dephasing times in a GaAs/ $\text{Al}_{0.3}\text{Ga}_{0.7}\text{As}$ superlattice and a ZnSe epilayer. The time scales considered here are on the order of a few hundred femtoseconds. This area is attracting a lot of interest these days mainly due to the new laser capabilities available. In particular, the recent invention of the self modelocked femtosecond Ti:sapphire laser has opened the doors for many new experimental techniques and helped reduce the signal-to-noise ratio. This is apparent from the recent literature.

The thesis is organized into several chapters that can be grouped under four major parts. The first part of the thesis concerns Chapter I which gives an introduction to the subject of the thesis and Chapter II which deals mainly with the sample parameters and preparation. Chapter III gives a detailed outlook on the experimental methods used in this study. The second part of the thesis is composed of Chapter IV and gives an overview of the theory needed to help understand the results of this study. The third part of the thesis is composed of three chapters dealing with the experimental findings of this study. This includes chapters V, VI, and VII. Chapter V addresses the picosecond Raman scattering results in the case of $x=0.4$ and $x=1$. Chapter VI treats the measured phonon penetration depth as a function of x . Chapter VII discusses the results of our subpicosecond degenerate

four wave mixing (DFWM) on both a GaAs/Al_{0.3}Ga_{0.7}As multiple QW sample and a ZnSe epilayer sample. The last part of the thesis is Chapter VIII which summarizes the results and conclusions of this study.

CHAPTER II
SAMPLE DESIGN AND PREPARATION
Growth Method

Among the most widely known semiconductor devices that explore the 2-D motion of the carriers are the quantum well lasers and the heterostructure transistors. In fact quantum Hall structures are already being used as standard resistors in many national bureau of standards laboratories. The growth and preparation methods for these heterostructure devices play crucial roles in their performance. The most commonly used materials are the well known III-V semiconductor compounds especially GaAs/ $\text{Al}_x\text{Ga}_{1-x}\text{As}$ heterostructures. Molecular Beam Epitaxy or MBE is a near-perfect growth technique that has a highly detailed control of the crystal growth [1-3]. Abrupt interfaces and controlled layer thicknesses down to the atomic monolayer size are typical for this method.

MBE is an epitaxial growth process that involves the deposition of one or more atomic and molecular beams of the constituent elements on a crystalline bulk material kept at a specific temperature in an ultra-high-vacuum (UHV) environment. The essential components of an MBE machine are shown in Figure 1. The molecular beams are generated from the evaporation cells (labeled In, Ga, etc...) kept at a precise temperature and equipped with accurate externally controlled shutters. Operation of these shutters allows for abrupt change of the molecular beam species in order to grow different layers of materials or uniformly mix several compounds to form an alloy. The molecular flux initiation or termination lasts only a tenth of a second while the growth rate is on the order of 5 Å of layer thickness per second. The substrate is maintained at a typical temperature of about 500-700 °C. The lower the substrate temperature the better since this minimizes the diffusion of the deposited atoms.

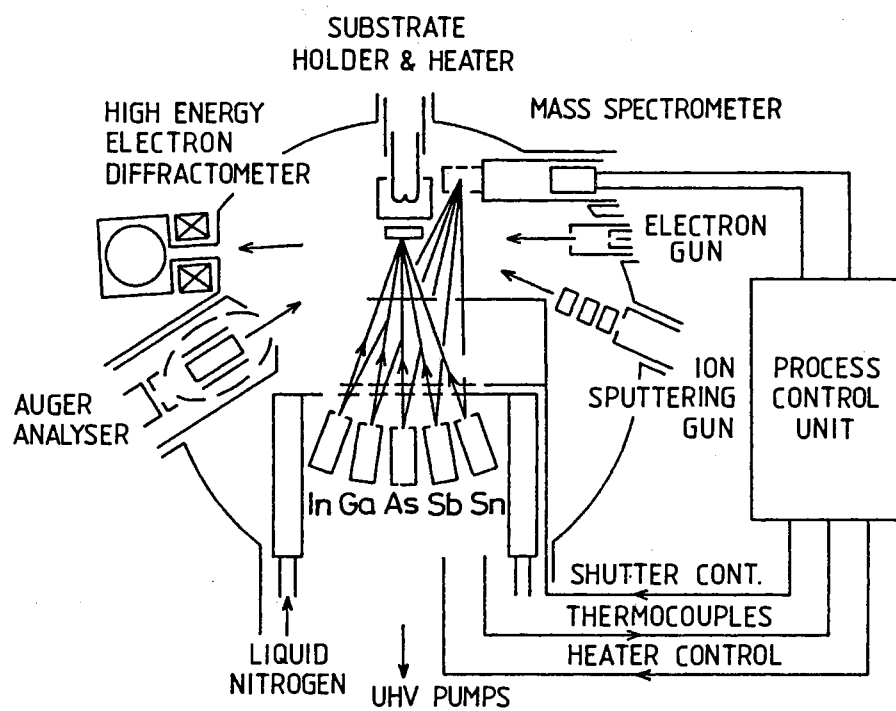


Figure 1. Essential components of an MBE machine (from Reference 3)

The substrate material quality and cleanliness is a crucial parameter in making these small structures. The substrate is mechanically polished and etched then introduced into the UHV chamber and deoxidized by heating. The UHV environment allows for the implementation of powerful 'in situ' analytical techniques that allow for monitoring each step of the growth sequence. First, the surface quality of the substrate is checked by Auger electron spectroscopy which analyses the chemical composition of the 5 to 10 Å outer atomic layer. The intensity of the molecular beams is precisely measured with a computer controlled mass spectrometer that is also utilized to detect any leak in the vacuum system and measure the various background gases such as water vapor. Reflection high-energy electron diffraction (RHEED) patterns are used during atomic layer growth to monitor the smoothness of the deposited film. RHEED analysis also provides a very useful means of measuring the layer thicknesses. In addition TEM and x-ray techniques have shown extremely precise sample information on the microscopic scale range [1,2].

Sample Structures

The GaAs/Al_xGa_{1-x}As heterostructure samples we used for this study are all grown on [100]-oriented GaAs substrates. The GaAs and AlAs have a cubic lattice with lattice constants of 5.6533 Å and 5.6611 Å respectively [15]. This leads to a very small lattice mismatch (about 0.14%) between these compounds allowing for the entire composition of Al_xGa_{1-x}As to be lattice matched on GaAs substrates. In these types of structures the GaAs layers are referred to as wells while the Al_xGa_{1-x}As layers as barriers. For thick and high enough barriers the electrons are well confined in the wells and can be treated in the standard 'particle in the box' quantum mechanics picture. These quantum well structures are usually represented by square wells as shown in Figure 2. The parameters L_w and L_b represent the well and barrier thicknesses, respectively. The typical structure of our samples is shown schematically in Figure 3. A complete list of all the GaAs/Al_xGa_{1-x}As samples used in this study is shown in Table I.

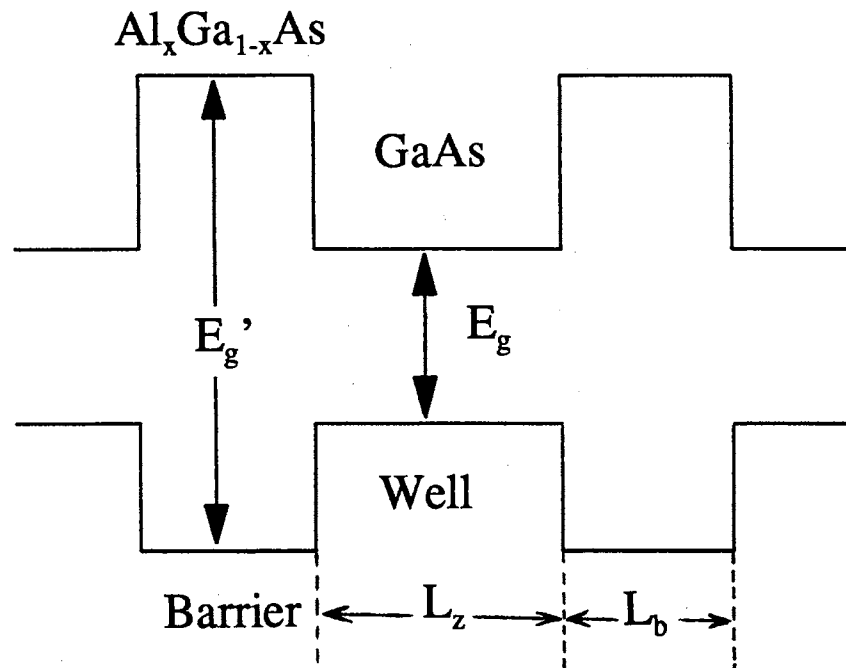


Figure 2. Typical band diagram of GaAs/Al_xGa_{1-x}As quantum wells

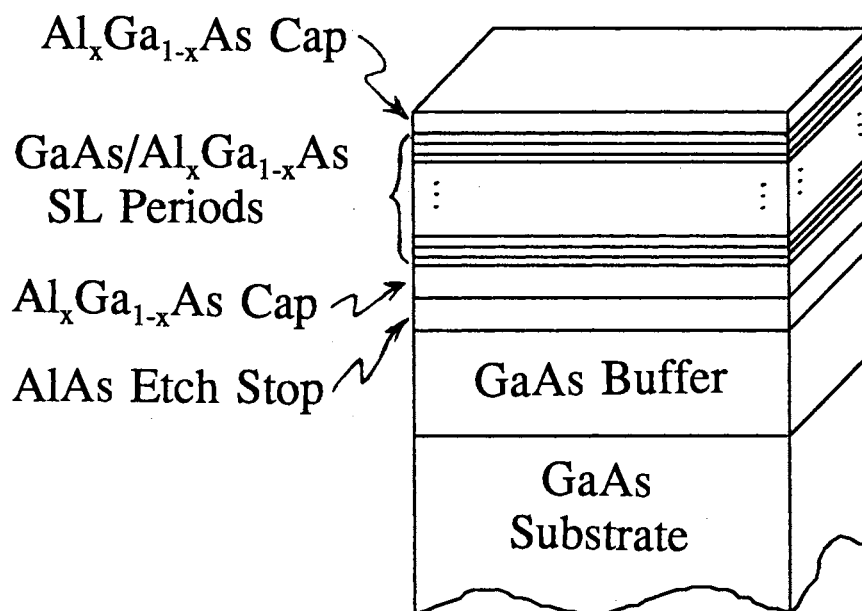


Figure 3. Schematic representation of the structure of our samples

TABLE I

GaAs/Al_xGa_{1-x}As SAMPLE PARAMETERS

x	L _z (Å)	L _b (Å)
1	100	6, 8, 11, 20, 100
0.4	100	5, 10, 15*, 20*, 25, 30, 40, 50
0.3	100	6, 23, 37, 51, 76, 100, 150
0.2	150	35, 70, 120, 180
0.2	70	70
0.18	70	30, 150
0.12	100	8, 31, 150

*Two samples grown at different times

All of our samples were grown by MBE method and most of them were provided by Dr. J.F. Klem at Sandia national laboratory. From a large piece of each sample ($\sim 10 \times 20 \times 0.8$ mm) we usually cleave a small portion (typically $4 \times 4 \times 0.8$ mm) on which we conduct our experiments. The nominal sample parameters are determined precisely during the growth and supplied with the samples. In addition, the parameters of some samples have been independently checked in another laboratory by x-ray diffraction and the results are consistent with Table I. Other critical samples have been grown a second time with duplicate parameters. These samples are clearly labeled in Table I. Before we conduct our experiments the samples are always degreased and cleaned in a trichloroethylene solution placed in an ultrasonic water bath. The cleaning process is repeated several times as needed. Immediately after that the samples are placed inside a cryostat for low temperature measurements.

Sample Preparation

Some other experiments involving the transmission of the laser beam through the sample required a delicate preparation of the samples. This is because of the opacity of the GaAs substrate which has to be removed in order to conduct these experiments. An outline of this technique is given in Appendix A.

CHAPTER III

EXPERIMENTAL METHODS

Picosecond Raman Scattering

Over the past few years, laser pulses have become shorter and shorter down to just a few cycles of the laser frequency [16]. Several techniques had to be employed to reach such ultrashort pulses. Modelocking and pulse compressing in a single-mode fiber [17,16] are commonly used in addition to the use of saturable absorbers in colliding pulse modelocked dye lasers [18,19].

In our time resolved Raman scattering experiments the picosecond laser source used is a modelocked Spectra-Physics Nd:YAG laser model 3800. The repetition rate of this laser is 82 MHz and the emission wavelength is at 1.06 μm . The pulse duration of the output pulses is about 90 ps with an average power of about 10 W. The next stage in our setup is a Spectra-Physics pulse compressor model 3695 shown schematically in Figure 4. Inside the pulse compressor, the 10 W/ 90 ps pulses from the YAG laser are focused tightly with a microscope objective into a 50 μm diameter fiber. This is a 20 m long single-mode fiber used to chirp the laser pulses. The output pulses are then reflected several times out of a negative-group-velocity-dispersion grating allowing the compression of the pulses in time. The pulses are then frequency doubled in a KTP crystal to the 532 nm wavelength and have an autocorrelation trace of about 2 ps. the average power output at this stage is about 800 mW and is enough to drive two independent femtosecond dye lasers. Most of the picosecond Raman scattering experiments we conducted are done at the 532 nm wavelength after the pulse compression. This is because these pulses are spectrally clean and have a relatively short bandwidth of about 7 cm^{-1} . This is important since the Raman modes we are measuring are typically about

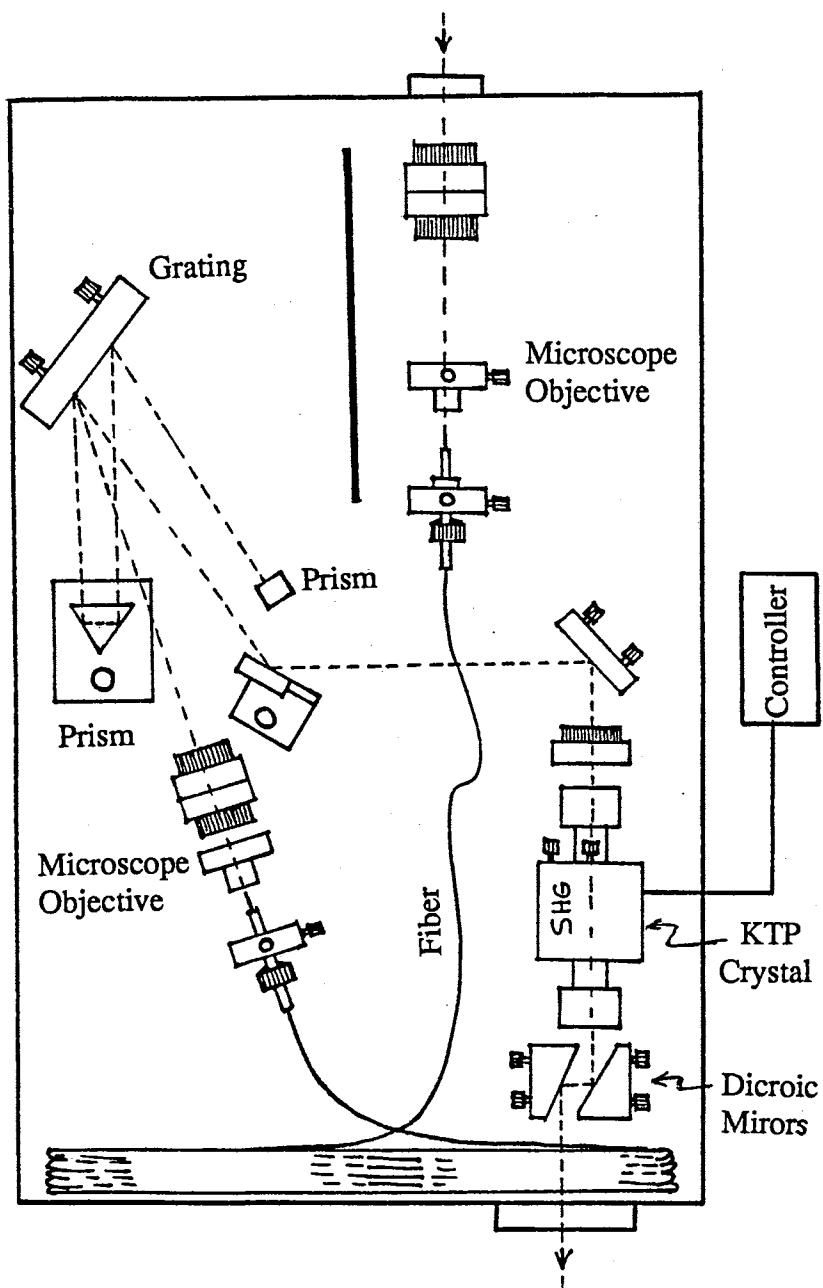


Figure 4. A schematic diagram of the pulse compressor used in the experiment

300 cm^{-1} away from the laser line. The average powers used in our experiments range from about 5 mW to about 150 mW at the sample.

For the wavelength dependent picosecond Raman scattering experiments, the situation is a little more involved technically due to the interplay and trade-off's involved between the pulse width, the band width, and the power and stability of the laser. We used a Spectra-Physics femtosecond dye laser model 3500 operating with a Rhodamine 6G (R6G) dye that can be tuned from 575 nm to 635 nm. The subpicosecond pulses that result from pumping this dye laser directly with the 2 ps pulses from the compressor are consequently too broad spectrally (about 50 cm^{-1}) and can not be used in a Raman scattering study of modes that are about 300 cm^{-1} close to the laser line. The spectrum of these pulses is shown by the solid curve in Figure 5. Due to the uncertainty principle, by increasing the time duration of our laser pulses we can reduce their linewidth. In this case, we completely bypass the pulse compressor and frequency double the output of the YAG laser to obtain pulses of about 30 ps duration at 532 nm with an average power of about 1.5 W. These pulses are then used to synchronously pump our dye laser. The output pulses are about 2 ps long but still spectrally broad (about 25 cm^{-1}) for our experimental requirements. The spectrum of these pulses is shown by the dotted curve in Figure 5. Our first approach to reducing the linewidth of our laser pulses is to introduce a second birefringent filter inside the dye laser cavity. Figure 6 shows the location of the birefringent filter inside the dye laser cavity. This has reduced the spectral bandwidth of the pulses but they were not spectrally "clean" due to the broad dye fluorescence and other light present in the cavity that still makes it through the dye laser optics. A spectral filter was then necessary to eliminate all this spurious light. We have to keep in mind that every extra step taken in improving the spectral shape of our pulses costs us some loss of the laser power. The spectral filter used is shown in Figure 6. This consists of a special collinear output prism that is a combination of three regular prisms precisely matched and mounted to keep the main output wavelength relatively collinear with the input beam while the other component wavelengths are deviated. An adjustable slit is then used to

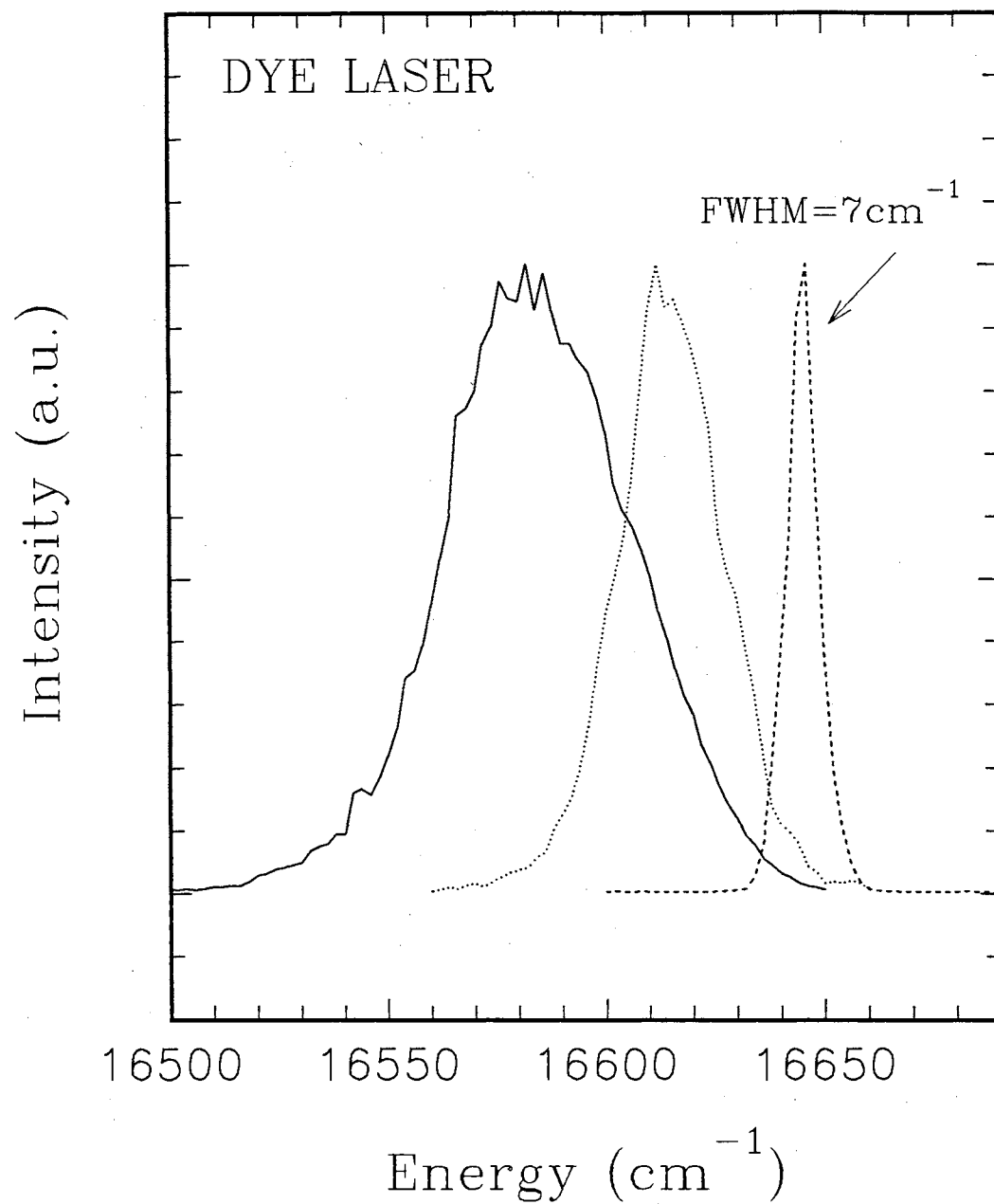


Figure 5. Spectra of the dye laser pulses under different conditions as explained in the text

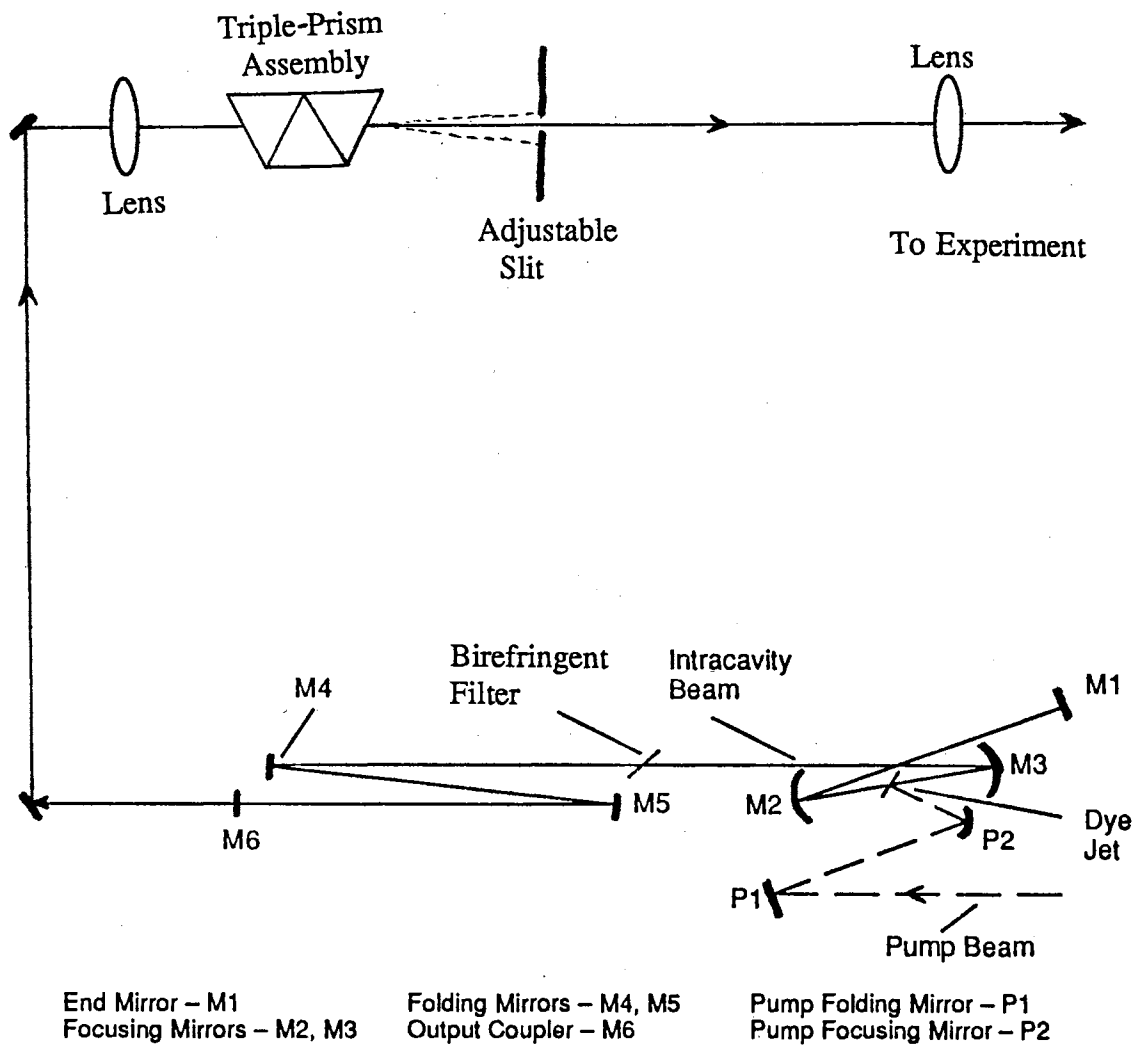


Figure 6. Schematics of the femtosecond dye laser cavity and spatial filter

block all the secondary lines and shoulders of the laser line. In Figure 5 we show by the dashed curve the spectrum of the final pulses obtained. The linewidth of these pulses is about 7 cm^{-1} with an autocorrelation of about 3 ps (or ~ 2 ps after sech^2 lineshape). The average usable power obtained for the experiment is about 30 mW at the sample location.

Pulse Width Measurements

The duration of our laser pulses is measured with an Inrad autocorrelator model 5-14B. A sketch of this is shown in Figure 7. The principle of operation of this equipment is based on the second harmonic generation by non-collinear mixing of two pulses in a nonlinear crystal. Essentially, the incoming pulse is split into two parts inside the autocorrelator. One pulse is delayed in time with respect to the other by retardation in a glass block. The two pulses are then recombined inside the nonlinear crystal to generate the second harmonic signal. The measured intensity of this signal ($I_{2\omega}$) depends on the amount of time delay (τ) between the two pulses as follows[20]

$$I_{2\omega}(\tau) = \int_{-\infty}^{+\infty} I_{\omega}(t) I_{\omega}(t + \tau) dt \quad (1)$$

where I_{ω} is the laser pulse profile. This leads to a relation between the pulse width (t_{real}) and the autocorrelation trace measured t_{auto} (i.e. the full-width-half-max of $I_{2\omega}$):

$$t_{real} = \alpha \times t_{auto}$$

where α is a constant that depends on the shape of the pulses. For instance, $\alpha \simeq 0.707$ for sech^2 shape pulses. Note that the autocorrelation trace width is always larger than the actual pulse width. Figure 8 shows an autocorrelation trace of our subpicosecond Ti:sapphire laser pulses. The nonlinear crystals used in the autocorrelator are a KDP or BBO crystal depending on the wavelength of the laser pulses used. Both crystals have very small thicknesses of about 0.5 mm

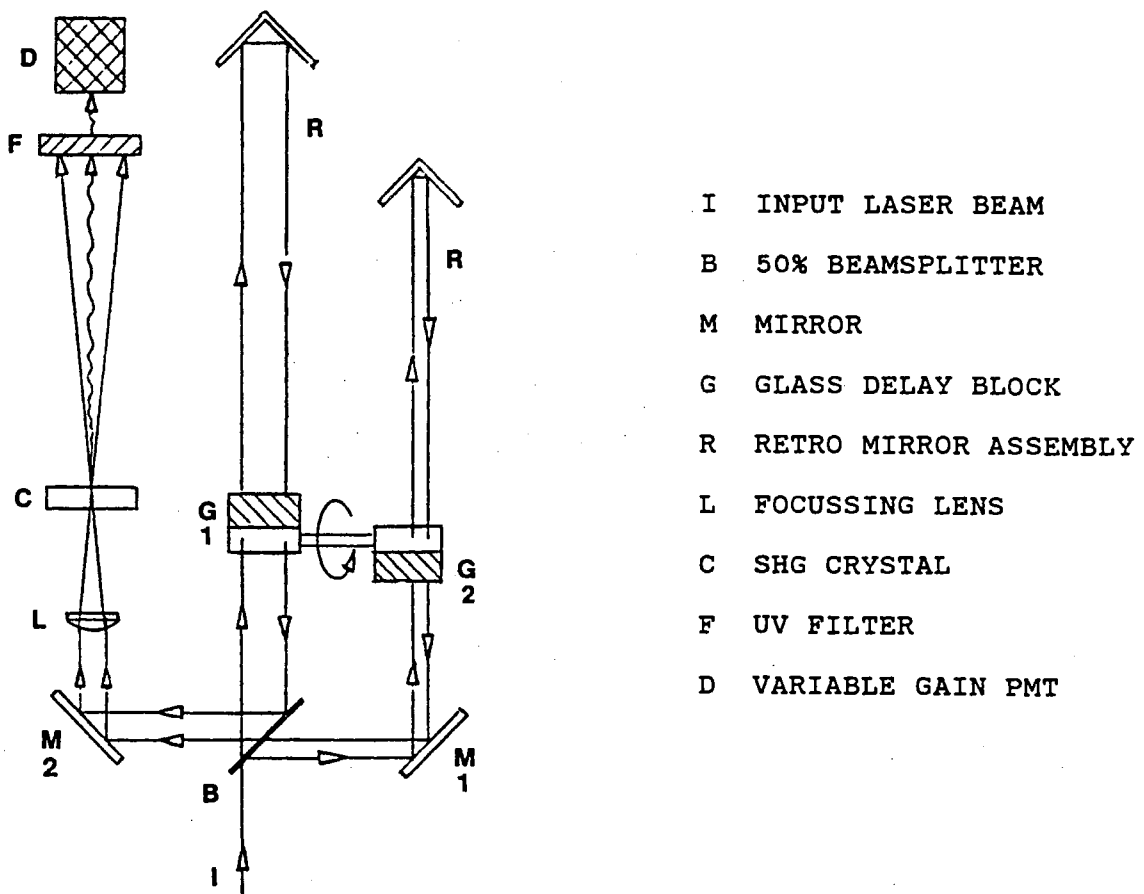


Figure 7. Schematic diagram of the autocorrelator used to measure our laser pulse width

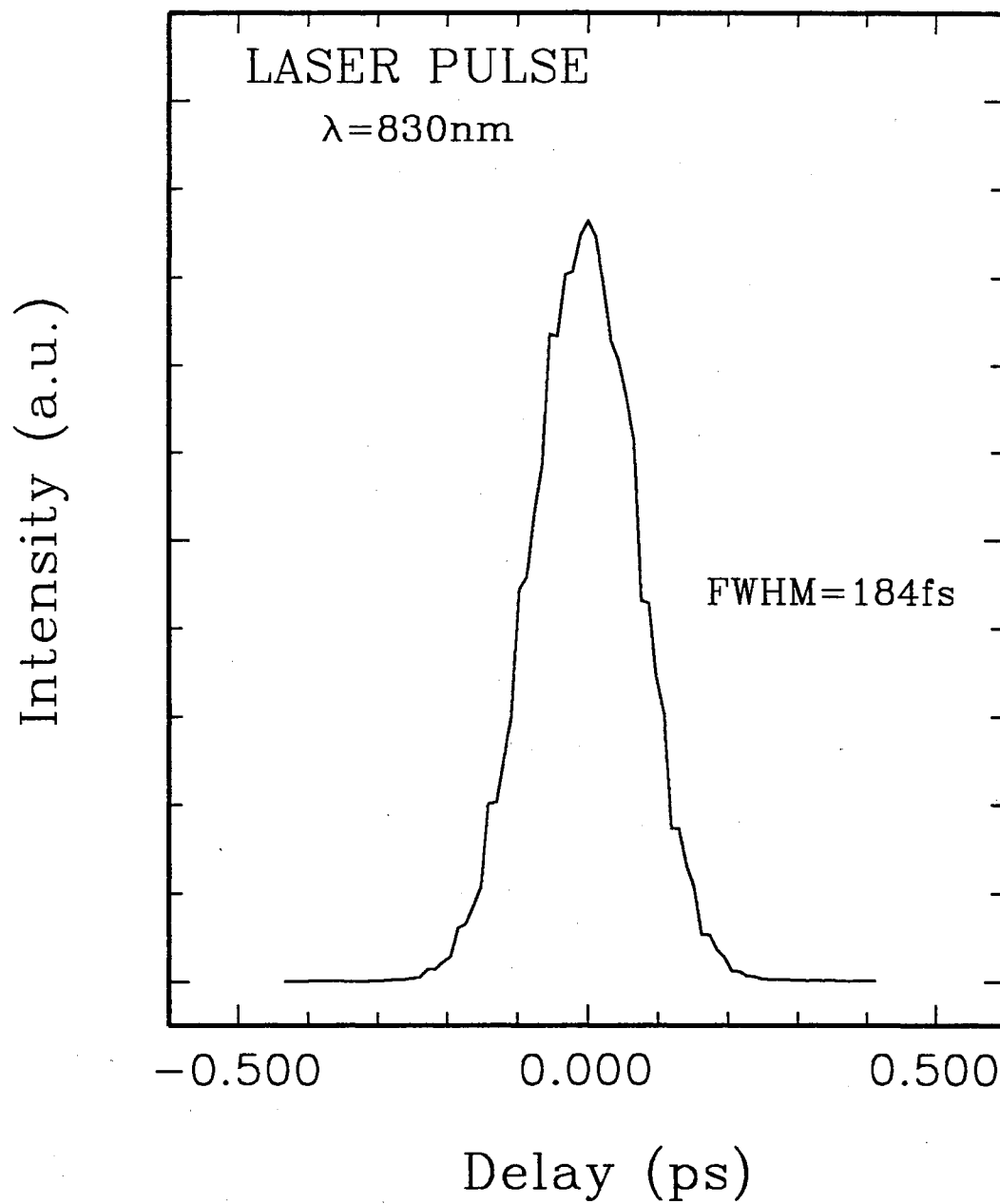


Figure 8. Autocorrelation trace of our Ti:sapphire laser pulses

to increase the time resolution. We also utilize two separate sets of glass delay-blocks for femtosecond or picosecond operation depending on the time resolution required. We can measure pulse widths from less than 50 fs to about 100 ps. In other instances we have also measured the width of our laser pulses using our four-wave-mixing setup. The results are very consistent with each other.

Picosecond Raman Setup

After all the conditioning and shaping of the laser pulses it is now possible to conduct our Raman experiments using the dye laser. Figure 9 shows our picosecond Raman scattering setup. Note that the femtosecond dye laser is not shown in the figure for simplicity. Its position is directly in front of the pulse compressor. This experimental arrangement is similar to a cw Raman scattering setup except for the excitation source which is, now, picosecond pulses. This allows for a time resolution on the order of the duration of the laser pulse as long as the laser pulse duration t is such that $\tau_{e-LO} < t < \tau_{LO}$. Where τ_{e-LO} and τ_{LO} are, respectively, the electron-LO phonon interaction time and the LO phonon lifetime. For GaAs LO phonons $\tau_{e-LO} \simeq 200$ fs and $\tau_{LO} \simeq 7$ ps at 5 K [21–25]. This is satisfied quite well with our 2 ps laser pulses. Our time resolved Raman scattering technique is referred to as one-beam-pump-and-probe since the same laser pulse is used to both excite and probe the hot electron and hot phonon populations [26–28]. This is possible since light scattering is an instantaneous process and the Raman scattered light will only exist as long as the laser pulse is in the sample. The time delay in our experiment is fixed by the laser pulse duration. There are other time resolved Raman scattering experiments that employ separate pulses for pumping and probing the hot phonon population. The main advantage of these is the possibility to study hot phonon population buildup or decay as a function of time. This experimental technique is widely used to measure the hot phonon lifetime (τ_{LO}) [21–24]. There are, however, several disadvantages of this technique over the one-beam-pump-and-probe method. At first, this technique requires the probe

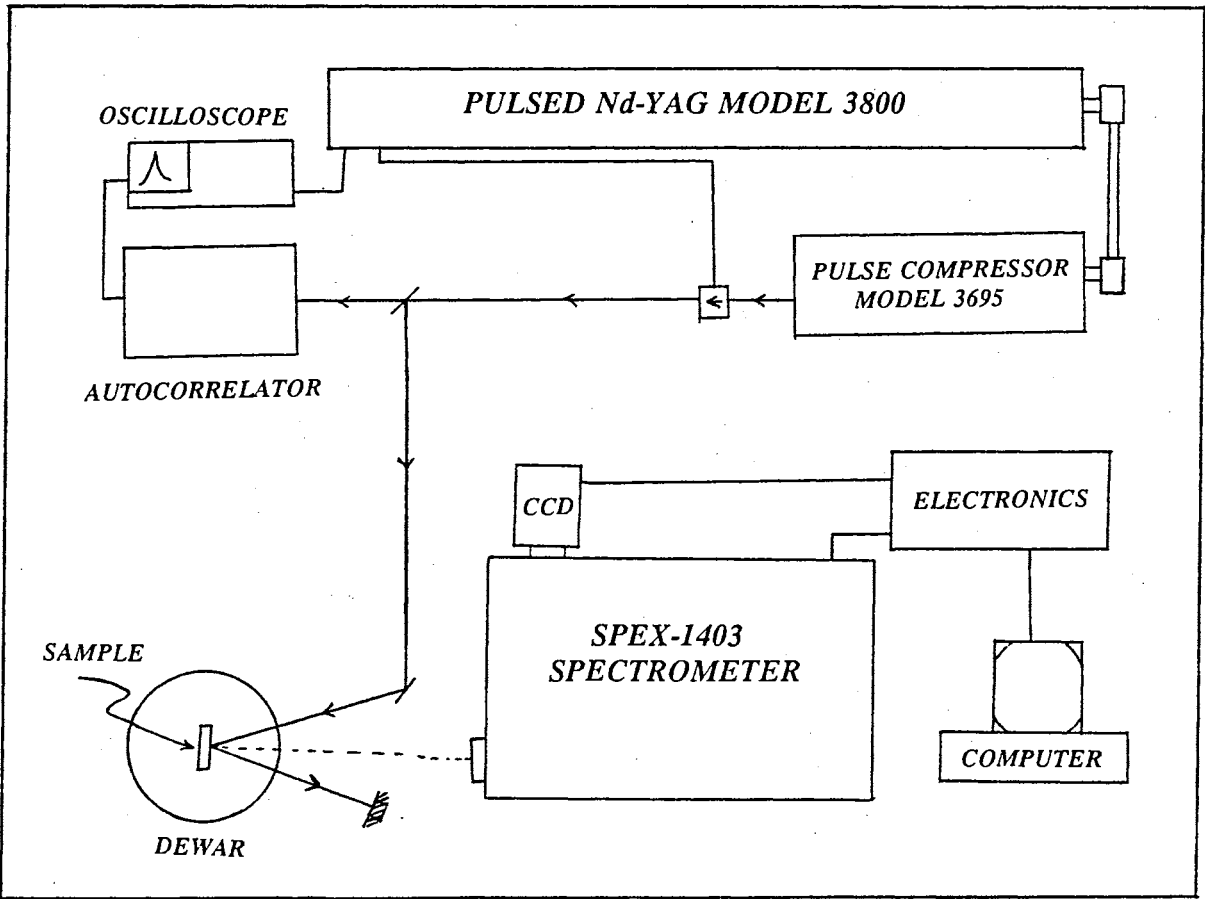


Figure 9. Schematic diagram of our Picosecond Raman scattering setup

beam to be attenuated at least 10 times compared to the pump beam in order to avoid creating a significant phonon population by the probe beam. This will reduce the overall phonon population excited. In addition, the problem of spatial and time overlap of the pulses on the sample create additional uncertainties. Also, the Raman scattered light caused by the pump and probe beam has to be spatially separated in the case of degenerate pump and probe experiments.

Our picosecond Raman scattering experiments are performed in the standard backscattering geometry on several series of GaAs/Al_xGa_{1-x}As SL's grown by MBE on [100]-oriented GaAs substrates . In each series L_b varies while x and L_z remain constant. A summary of our sample parameters is given in Table I. In the technique we use; an optical pulse creates a hot electron distribution which generates hot phonons via relaxation. This same pulse also probes the hot phonon occupation number, which is determined through the Stokes and anti-Stokes Raman intensities. The details of the experimental procedures and data analysis is discussed in Chapter V. The excited carrier densities in our experiments are estimated by measuring the laser spot size on the sample. These carrier densities are then adjusted in order to yield a phonon occupation number (N_q) of about 0.3 for bulk GaAs. The excited carrier densities are intentionally made low (<10¹⁷ cm⁻³) so that the experimental N_q varies linearly with the incident laser power, P. A plot of N_q versus P for the bulk GaAs LO phonon can be found in Figure 19 of Chapter V. Our experiments are conducted at temperatures ranging between 172 K and 16 K with similar results. At temperatures larger than about 50 K, a correction for the thermal phonon population must be taken into account when extracting N_q from the Stokes and anti-Stokes intensities. In our experiment since we measure the linear dependence of N_q on P we obtain the following expression for N_q:

$$N_q \approx N_{th} + \left(\frac{\Delta N_q}{\Delta P} \right) P$$

where N_{th} is the thermal phonon population which is negligible at low temperature. The term in parenthesis is the slope of the line and is proportional to the hot phonon generation rate for a fixed time delay between the pump and probe pulses.

The incident light is polarized along the [110] direction to take advantage of the high efficiency of the spectrometer gratings. The scattered light is collected and analyzed through a standard Spex triple monochromator model 1877 or Spex double monochromator model 1403. The photon counting system used is a Charge-Coupled-Device or CCD multichannel detector made by Photometrics. The detector area composed of 512 by 512 pixels has a very high sensitivity and spatial resolution which depend mainly on the spectrometer used. All the components of the experimental setup are interfaced to a personal computer model 386.

Degenerate Four Wave Mixing (DFWM)

Among the most commonly used pump-and-probe experiments is the so-called degenerate-four-wave-mixing (DFWM). This is considered one of the simplest time resolved pump-and-probe spectroscopic techniques. The setup used for performing these experiments is shown schematically in Figure 10. In this experiment, two laser pulses propagating along \mathbf{k}_1 and \mathbf{k}_2 interact inside a sample to coherently generate a signal along the background-free direction $2\mathbf{k}_2 - \mathbf{k}_1$. The interaction between the pump and probe pulses creates a transient polarization grating which self-diffracts part of the probe beam into the $2\mathbf{k}_2 - \mathbf{k}_1$ direction. The signal is spatially filtered with a pinhole and measured with a PMT as a function of the time delay between the pump and probe pulses. To improve the signal to noise ratio, we use the standard technique known as difference-frequency lock-in amplification. In this method both the pump and probe beams are chopped with frequencies f_1 and f_2 . The signal is then detected at the difference-frequency $f_1 - f_2$. The PMT we use is a Hamamatsu side-on tube model 928 with an applied voltage of about 700 Volts. The lock-in amplifier used is an EG&G model 504. A program was written to interface both the lock-in amplifier and the stepper motor on the optical delay line to a 286 personal computer. Additional details about this experiment can be found in Appendix B.

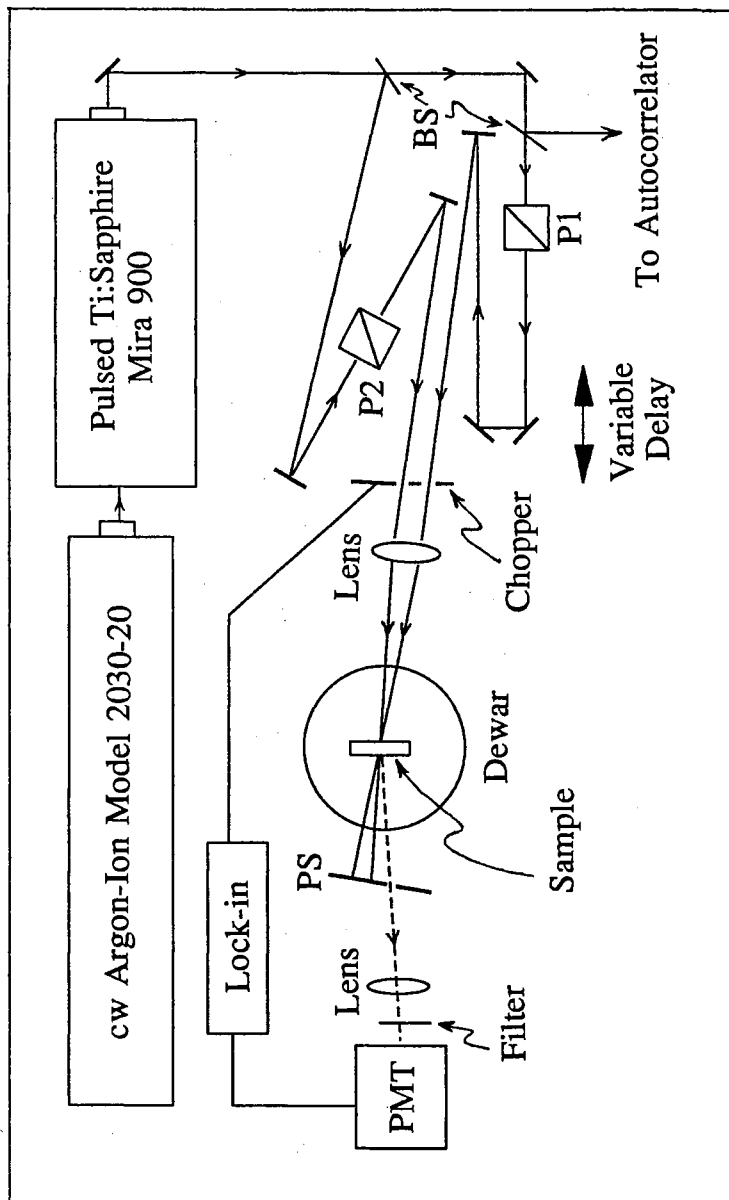


Figure 10. A schematic diagram of our DFWM setup. P1 and P2 are polarizers, BS is a beam splitter, and PS is a pinhole-screen

The time resolution of this experiment is only limited by the duration of the laser pulses. The laser source used in these experiments is composed of two component lasers. A Spectra-Physics Argon ion laser model 2030 operating at 8 watts in the multiline configuration is used to pump a state-of-the-art Coherent Ti:sapphire laser model Mira-900. The Mira laser uses the Kerr-lens effect of the Ti:sapphire crystal to mode lock itself and output transform-limited laser pulses as short as 120 fs (with a sech^2 shape). The output has a tuning range from about 800 to 900 nm with an average output power of about 1.5 watts at the peak wavelength. Figure 11 shows typical laser power and pulse width as a function of the wavelength tuning range.

In other experiments on II-VI semiconductor compounds we use a LiIO_2 crystal to frequency double the output of the Mira. This allows us to reach excitonic resonances in these compounds with femtosecond pulses. After second harmonic generation we obtain tunable UV pulses with a duration of less than 130 fs and an average power of about 160 mw.

It is important to note that in order to conduct the DFWM experiments on our semiconductor heterostructures we must make sure that the sample is somewhat transparent to our laser excitation. This is accomplished by removing the GaAs substrate from our samples as discussed in Appendix A. The effective thickness of the sample is then reduced to a few microns only. This makes the sample relatively transparent to radiations just above the band gap. Figure 12 shows a substrate-removed superlattice (SL) sample and the pump and probe geometry used for these experiments.

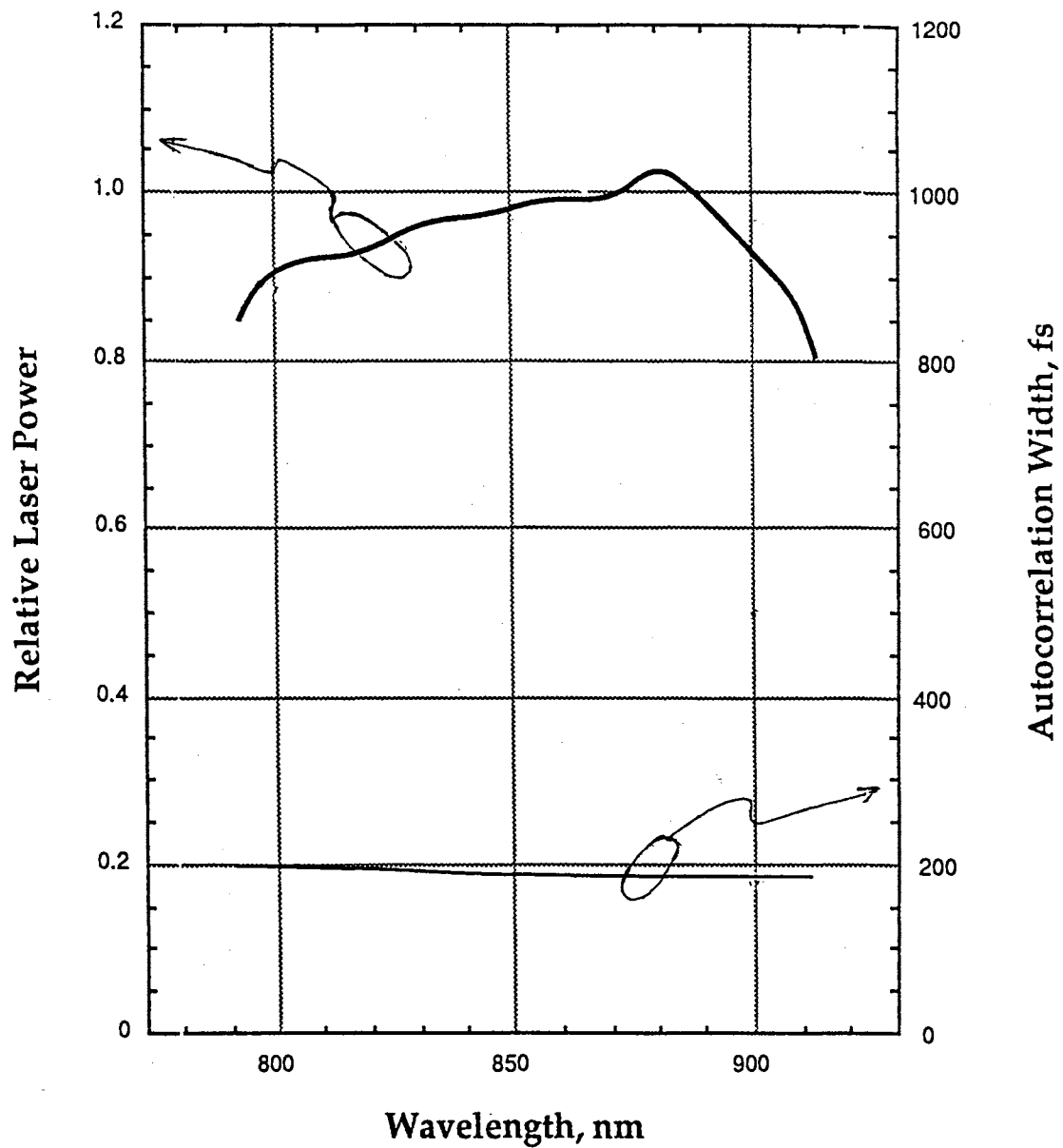


Figure 11. Ti:sapphire laser output power and pulse autocorrelation width as a function of wavelength tuning

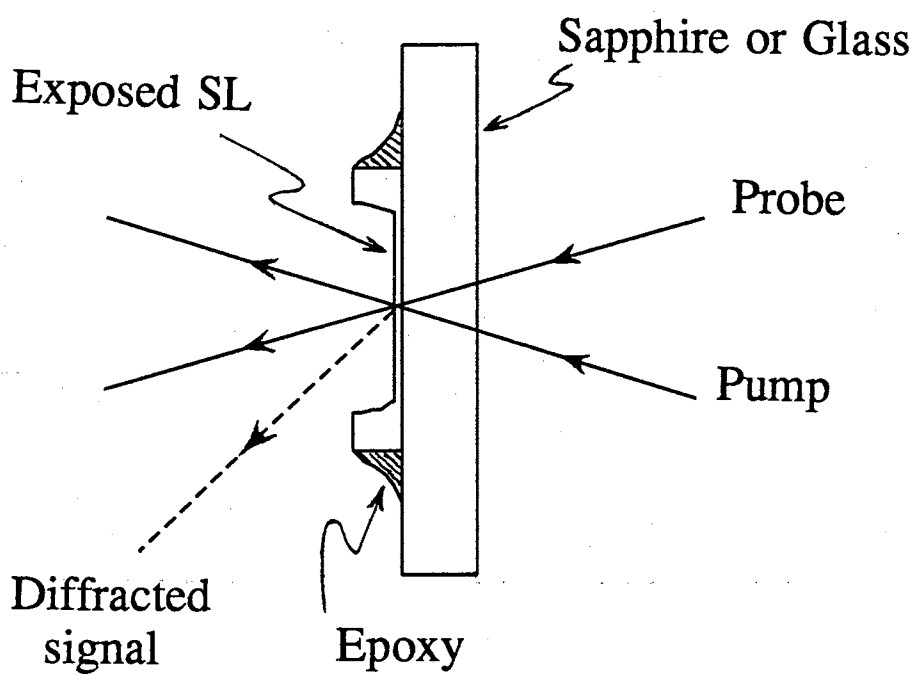


Figure 12. A schematic representation of our substrate-removed SL sample and the pump and probe geometry used in the DFWM experiments

CHAPTER IV

THEORETICAL BACKGROUND

The most practical and commonly used model to describe the hot electron interaction with hot phonons is based on solving the Boltzman equations for phonons and electrons . In the literature, only the GaAs bulk case is treated rigorously. An attempt by Pötz et al.[29] in considering the QW case will be referred to later in this chapter. This model represent an adaptation of the bulk model with incorporation of the main physics involved in a QW case. Some of the assumptions used in this model are the use of bulk optical phonon modes and infinite barriers (i.e. thick AlAs layers). The model also assumes parabolic bands. We will, first, discuss the electron and phonon dynamics in bulk GaAs and then discuss the QW case.

Bulk GaAs

Rate Equations

The semiclassical Boltzman equations for carriers and phonons are used to describe the transport properties of the particles in the medium. Essentially, one assumes that a free-particle trajectory is interrupted by instantaneous scattering events. The quantum-mechanical scattering probabilities are calculated to yield the physical properties of interest. The Boltzman equation for the various types of carriers in a semiconductor can be written in the following general form

$$\frac{df}{dt} = \left(\frac{df}{dt}\right)_{exc} + \left(\frac{df}{dt}\right)_{c-ph} + \left(\frac{df}{dt}\right)_{c-c} + \left(\frac{df}{dt}\right)_{c-c'} + \left(\frac{df}{dt}\right)_{loss} \quad (2)$$

where f is the carrier occupation. The first term in Equation 2 is due to photoexcitation of the carriers. The terms labeled c-c and c-c' refer to carrier-carrier scattering of the same and different types respectively. Carrier-phonon scattering is represented by the term labeled c-ph. The loss term is dominated by non-radiative recombination of electrons and holes.

For bulk materials with parabolic bands the absorption of a photon energy $\hbar\omega > E_g$ creates an e-h pair with kinetic energies

$$E_{exc}^{(j)} = \frac{(\hbar\omega - E_g)m_e m_h}{(m_e + m_h)m_j}, \quad j = e, h \quad (3)$$

Where m_j is the electron or hole effective mass. Photoexcitations from the light hole (LH) and split-off hole (SOH) bands are usually neglected for GaAs bulk due to their small contributions for excitations near the bottom of the conduction band. The free carrier absorption will change the effective carrier density by the following approximate rate

$$G_{fca} = \frac{\alpha_{fca}}{\alpha_\omega} G(\omega; t) \quad (4)$$

where $G(\omega; t)$ are the rates of change of the e-h density due to one- and two-photon absorption:

$$G_j(\omega; t) \simeq \frac{1}{3} \frac{\alpha_\omega^{(j)} I_\omega^j(t)}{j \hbar\omega}, \quad j = 1, 2 \quad (5)$$

where j labels the one and two photon process and $I_\omega^j(t)$ is the excitation power density. Using Equation 2 we can write the rate equations for the change of carrier densities (n) and energy (E) respectively

$$\frac{dn(t)}{dt} = \left(\frac{dn(t)}{dt} \right)_{exc} + \left(\frac{dn(t)}{dt} \right)_{iv} + \left(\frac{dn(t)}{dt} \right)_{loss} \quad (6)$$

$$\frac{dE(t)}{dt} = \left(\frac{dE(t)}{dt} \right)_{exc} + \left(\frac{dE(t)}{dt} \right)_{c-ph} + \left(\frac{dE(t)}{dt} \right)_{c-c'} + \left(\frac{dE(t)}{dt} \right)_{loss} \quad (7)$$

The term labeled iv in Equation 6 represents the carrier density change due to intervalley scattering. The energy transfer between carriers and phonons and carriers and other types of carriers is contained in the terms labeled c-ph and c-c'. The energy change due to c-ph interaction can be written as follows,

$$\left(\frac{dE(t)}{dt}\right)_{c-ph} = - \sum_j \sum_i^{\text{modes couplings}} \hbar\omega_j \left(\frac{dN_j(\mathbf{q}, t)}{dt}\right)_{ph-c,i} \quad (8)$$

Using the Boltzman equation for phonons we can express the phonon generation rate as follows [26,29],

$$\frac{dN(\mathbf{q}, t)}{dt} = \left[\sum_{\text{carriers couplings}} \sum \left(\frac{dN(\mathbf{q}, t)}{dt}\right)_{ph-c} \right] + \left(\frac{dN(\mathbf{q}, t)}{dt}\right)_{ph-ph} \quad (9)$$

Using Fermi's "Golden rule" one can express the ph-c term in the following form [29-31]

$$\begin{aligned} \left(\frac{dN(\mathbf{q}, t)}{dt}\right)_{ph-c} &= \frac{2\pi}{\hbar} M(q) \times \sum_{\mathbf{k}} f(\mathbf{k}, t) [1 - f(\mathbf{k} - \mathbf{q}, t)] \times [N(q, t) + 1] \\ &\times \delta(E(k - q) - E(k) + \hbar\omega) - f(k, t) [1 - f(k - q, t)] \\ &\times N(q, t) \times \delta(E(k) - E(k - q) + \hbar\omega) \end{aligned} \quad (10)$$

where $f(\mathbf{k}, t)$ is the electron occupation number. $M(q)$ is given by the interaction Hamiltonian $H^{(\pm)}$ for phonon emission and absorption and the corresponding quantum-mechanical transition amplitudes as follows [26,29]:

$$\left| \langle k \mp q, N_q \pm 1 | H^{(\pm)} | k, N_q \rangle \right|^2 = M(q) \cdot \left(N_q + \frac{1}{2} \pm \frac{1}{2} \right) \quad (11)$$

where we have simplified the notation of $N(\mathbf{q}, t)$ to N_q . For the Fröhlich and deformation potential carrier-phonon interactions we have, respectively, the following expressions for $M(q)$ [29,30]

$$M_F(q) = \frac{1}{V} 2\pi e^2 \hbar\omega_{ph} \left(\frac{1}{\epsilon_\infty} - \frac{1}{\epsilon_0} \right) \cdot \frac{1}{q^2} \quad (12)$$

and

$$M_{ij} = \frac{1}{V} \frac{D_{ij}^2 \hbar}{2\rho\omega_{ph}} \quad (13)$$

where D_{ij} is the appropriate deformation potential for scattering between valleys i and j , ω_{ph} is the frequency of the phonon involved, and ρ is the material density. In Equation 12 we have neglected the LO phonon dispersion and used just the zone-center frequency. This is justified by the $1/q$ dependence of the Fröhlich interaction which leads to small- q phonons domination of this scattering.

Fröhlich Interaction

For the Fröhlich interaction, we can rewrite Equation 9 in a more general form using the results of Equations 10 and 12:

$$\frac{dN_q}{dt} = \frac{1}{q^3} \cdot [-A_q N_q + B_q (N_q + 1)] + \left(\frac{dN_q}{dt} \right)_{ph-ph} \quad (14)$$

Where A_q and B_q are given by

$$A_q = \frac{2m^{*2}\omega_{LO} e^2}{\hbar^4} \left(\frac{1}{\epsilon_\infty} - \frac{1}{\epsilon_0} \right) \int_{E_{q1}}^{\infty} f(E_K) [1 - f(E_K - E_{LO})] dE_K \quad (15)$$

$$B_q = \frac{2m^{*2}\omega_{LO} e^2}{\hbar^4} \left(\frac{1}{\epsilon_\infty} - \frac{1}{\epsilon_0} \right) \int_{E_{q2}}^{\infty} f(E_K) [1 - f(E_K + E_{LO})] dE_K \quad (16)$$

with

$$E_{q1} = \frac{(E_q - E_{LO})^2}{4E_q}, \quad E_{q2} = \frac{(E_q + E_{LO})^2}{4E_q}, \quad E_q = \frac{\hbar^2 q^2}{2m^*} \quad (17)$$

E_{q1} and E_{q2} are, respectively, the minimum energies required by an electron to absorb or emit an LO phonon with wavevector q .

The ph-ph term in Equation 14 is related to the phonon decay and can be written as

$$\left(\frac{dN_q}{dt} \right)_{ph-ph} = -\frac{N_q - N_{eq}}{\tau_{LO}} \quad (18)$$

where τ_{LO} is the LO phonon lifetime. N_{eq} is the LO phonon occupation number at thermal equilibrium with the electrons at T_e and is given by

$$N_{eq} = \frac{1}{\exp\left(\frac{\hbar\omega_{LO}}{k_b T_e}\right) - 1} \quad (19)$$

A theoretical calculation of τ_{LO} is quite complicated and can only give an estimate at best. An approximate lattice-temperature dependence of τ_{LO} is given by the following expression [32]:

$$\tau_{LO}(T) = \tau_{LO}(0) \frac{1}{1 + 2 \left[\exp\left(\frac{\hbar\omega_{LO}}{2k_B T}\right) - 1 \right]^{-1}} \quad (20)$$

Where $\tau_{LO}(0)$ is the zero-temperature limit. This expression gives a room temperature (RT) value of $\tau_{LO}(RT) \approx \frac{\tau_{LO}(0)}{3}$ which gives a rather large change of τ_{LO} with T compared to the measured values. For instance bulk GaAs has $\tau_{LO} \simeq 7$ ps at 5 K and $\tau_{LO} \simeq 4$ ps at RT [7]. This has led most theoreticians to rely on the experimental values for τ_{LO} in their calculations.

Combining Equations 14 and 18 we have completed the expression of the phonon Boltzman equations. These are inhomogeneous linear first-order differential equations that can be solved by direct numerical integration or by using ensemble-Monte Carlo techniques. Under the assumption of nondegenerate electrons with Boltzman distribution and temperature T_e one can integrate Equation 14 to obtain [26,27,30]:

$$\frac{dN_q}{dt} = 2\omega_{LO} \frac{e^2}{\hbar c} \sqrt{\frac{2\pi^3 m^* c^2}{k_b T_b}} \left(\frac{1}{\epsilon_\infty} - \frac{1}{\epsilon_0} \right) \cdot \frac{n_e}{q^3} \cdot \exp\left(\frac{-E_{q2}}{k_b T_e}\right) \cdot \left(1 - \frac{N_q}{N_{eq}}\right) - \frac{N_q - N_{eq}}{\tau_{LO}} \quad (21)$$

Intervalley Scattering

Intervalley scattering is due to the deformation potential electron-phonon interaction as given by Equation 13. This scattering mechanism involves large- q phonons which are not observable by light scattering experiments. Intervalley scattering is represented by arrows 2 and 3 in Figure 13 where we show a schematic representation of the GaAs band structure. This is a very fast process whose main effect is to reduce the electron population in a given valley. For electrons with

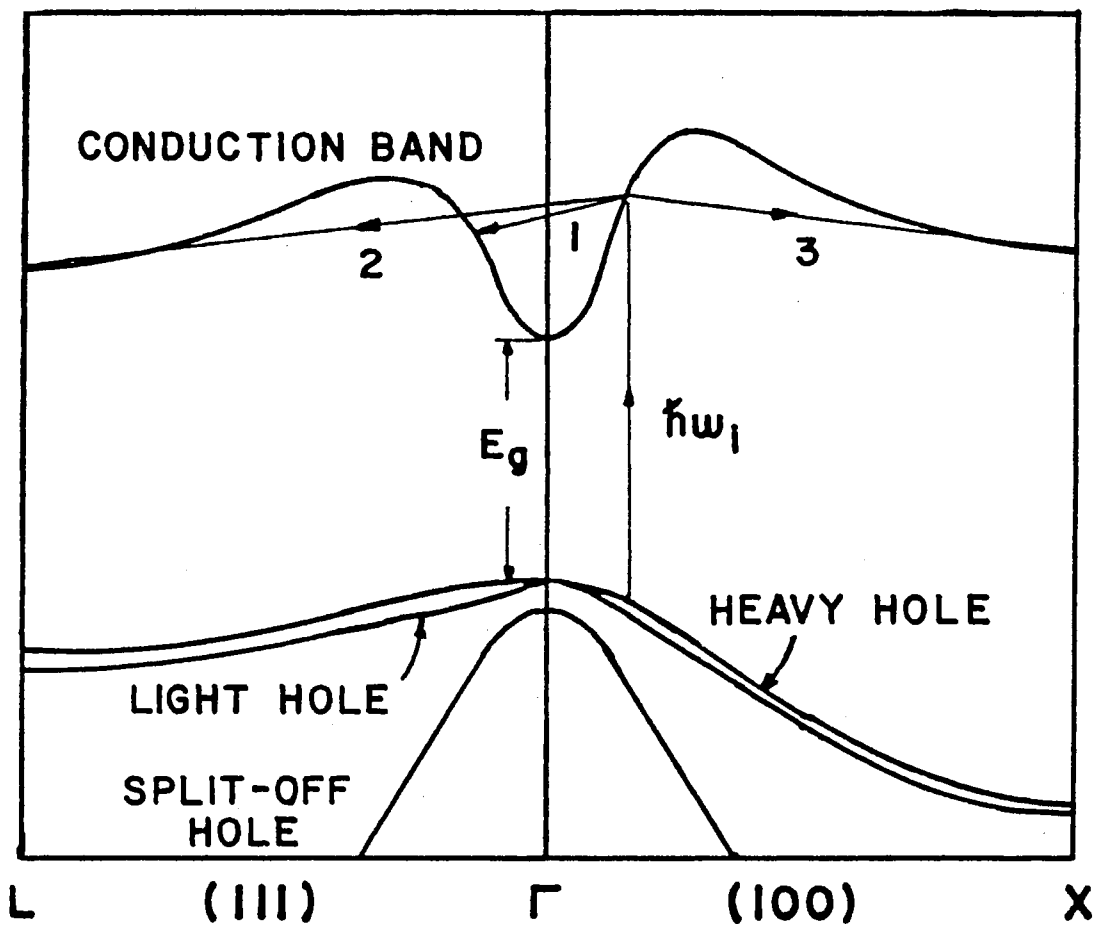


Figure 13. A schematic representation of the GaAs energy band structure. Arrow 1 indicates intravalley scattering while 2 and 3 indicate intervalley scattering

energy E in the i^{th} valley, the rate of change of their occupation number is given by [26,31]

$$\begin{aligned} \frac{\partial f_{i-j}(E_j)}{\partial t} = & -\frac{D_{ij}^2 m_j^{3/2}}{\sqrt{2\pi\hbar^3 \rho \omega_{ij}}} \{N_{ij} \sqrt{E_i + \hbar\omega_{ij} - \Delta E_j} \\ & + (N_{ij} + 1) \sqrt{E_i - \hbar\omega_{ij} - \Delta E_j}\} \cdot f_i(E_i) \end{aligned} \quad (22)$$

Where N_{ij} is the occupation number of the zone-edge phonons with frequency ω_{ij} . ΔE_j is the minimum energy of the j^{th} valley measured from the bottom of the conduction band. m_j is the density-of-states mass of the electrons in the j^{th} valley,

$$m_j^{3/2} = (m_j^x m_j^y m_j^z)^{1/2} \quad (23)$$

In the case of our experiment the electrons are initially excited into the Γ valley. The electrons that have sufficient energy will immediately undergo intervalley scattering. This process is very fast and occurs within the first 100 fs after excitation [16,25,33]. Once in the X or L valley, the electrons will take a long time to return to the Γ valley due to the large effective mass in these valleys. The return time of the electrons is on the order of 10 ps or more [51]. Thus, for the time scale of our experiment which is about 2 ps the electrons that undergo intervalley scattering are essentially lost and their subsequent effect is minor. We have in fact experimentally verified this by exciting the electrons above and below the energy threshold for Γ -to-X intervalley scattering and observed practically no difference in our measured hot phonon generation rates.

Nonparabolicity

The theory at hand assumes parabolic bands which is not a bad approximation for low energy electrons. However, when the carriers are excited higher up in the conduction band the nonparabolicity of these bands becomes important and must be considered as can be seen in Figure 13. The main effect of nonparabolic bands is to decrease the e-ph interaction time, thus increasing the hot phonon

generation rates. This is discussed in great details by Collins and Yu [26,30]. The decrease in τ_{e-LO} is estimated to be about 20 % for a Γ electron with energy $E=500$ meV in GaAs bulk. The nonparabolicity of the conduction band in GaAs bulk is expressed within the Kane model by the following expression [34]:

$$\frac{\hbar^2 k^2}{2m^*} = E_k + \alpha E_k^2 + \beta E_k^3 \quad (24)$$

Where α and β are constants estimated to be about 0.577 (eV)^{-1} and 0.047 (eV)^{-2} .

Phonon Models in GaAs/ $\text{Al}_x\text{Ga}_{1-x}\text{As}$ QW's

Mesoscopic semiconductors are considerably more complicated to treat theoretically than bulk materials. Due to the added symmetry in the z-direction, drastic changes occur in both the electronic properties and the phonon modes. Quantum confinement of the carriers occurs and results in the appearance of electronic subbands. Thus, the simple plane-wave approximation used in the bulk case is no longer valid. In addition, these subbands can become highly non-parabolic for narrow QW's. This is especially true for the hole bands where the heavy-hole (HH) and light-hole (LH) mixing is very important [35,36]. The e-h generation process is also influenced by the presence of subbands which leads to an "initial" electron energy distribution that is far from being monoenergetic as in the bulk case.

On the other hand, the phonon spectrum is also quite different from that of bulk materials. Due to the folding of the Brillouin zone, several modes with large q become accessible to Raman scattering (see Figure 17 in the next Chapter). In addition, special interface modes appear with dispersion curves overlapping those of the confined modes and adding more complications to any theoretical treatment of the QW problem. Despite the theoretical complications involved, several phonon models can be found in the literature. The inherent complexity of the problem generated a lot of controversies among these models as one would expect. In the following we will give a brief account of each of these models and give an update

as to which of them most reliably describes the phonon modes in 2D systems. The origin of the z-axis is taken at the center of the well layer.

Slab Model

This model was first developed by Fuchs and Kliever to study dielectric slabs of relatively large thicknesses (i.e. several μm) [37,38]. The model was recently modified and adapted to study phonon modes in semiconductor QW structures [39–41]. The slab model uses purely electrostatic boundary conditions at the interfaces leading to Fuchs-Kliever modes with antinodes at the interfaces where the potentials vanish. Both the displacement (u_z) and potentials (V) obtained from this model are shown in Figure 14. This model predicts two types of modes in the GaAs frequency region. The confined modes have the following potentials [42]:

$$\Phi_n(z) = c \cdot \begin{cases} \cos(q_z z), & n = 1, 3, 5, \dots \\ \sin(q_z z), & n = 2, 4, 6, \dots \end{cases} \quad (25)$$

with

$$c = \left[\frac{\hbar(\omega_{LO}^2 - \omega_{TO}^2)}{\epsilon_\infty \omega_{LO} A L_z} \right]^{1/2} \cdot \frac{1}{(q_z^2 + q_{\parallel}^2)^{1/2}}$$

where A is the in-plane normalization area and q_z is the phonon wavevector in the growth direction (see Equation 29 in the next Chapter). The other modes predicted have a strong dependence on the in-plane wavevector q_{\parallel} which is in the plane of the QW layers. The potentials and displacements for these modes are also shown in Figure 14. Expressions for the potentials of these modes can be found in References [39,40,43]. The interface modes are usually Raman active only near an electronic resonance which is not the case in our experiments. Therefore, we do not observe these modes.

It is clear that the "mechanical boundary condition" which requires continuity of the displacement at the interfaces is not satisfied by this model. However, the overall shape of the potentials resembles more or less those of the microscopic calculation which is the most reliable.

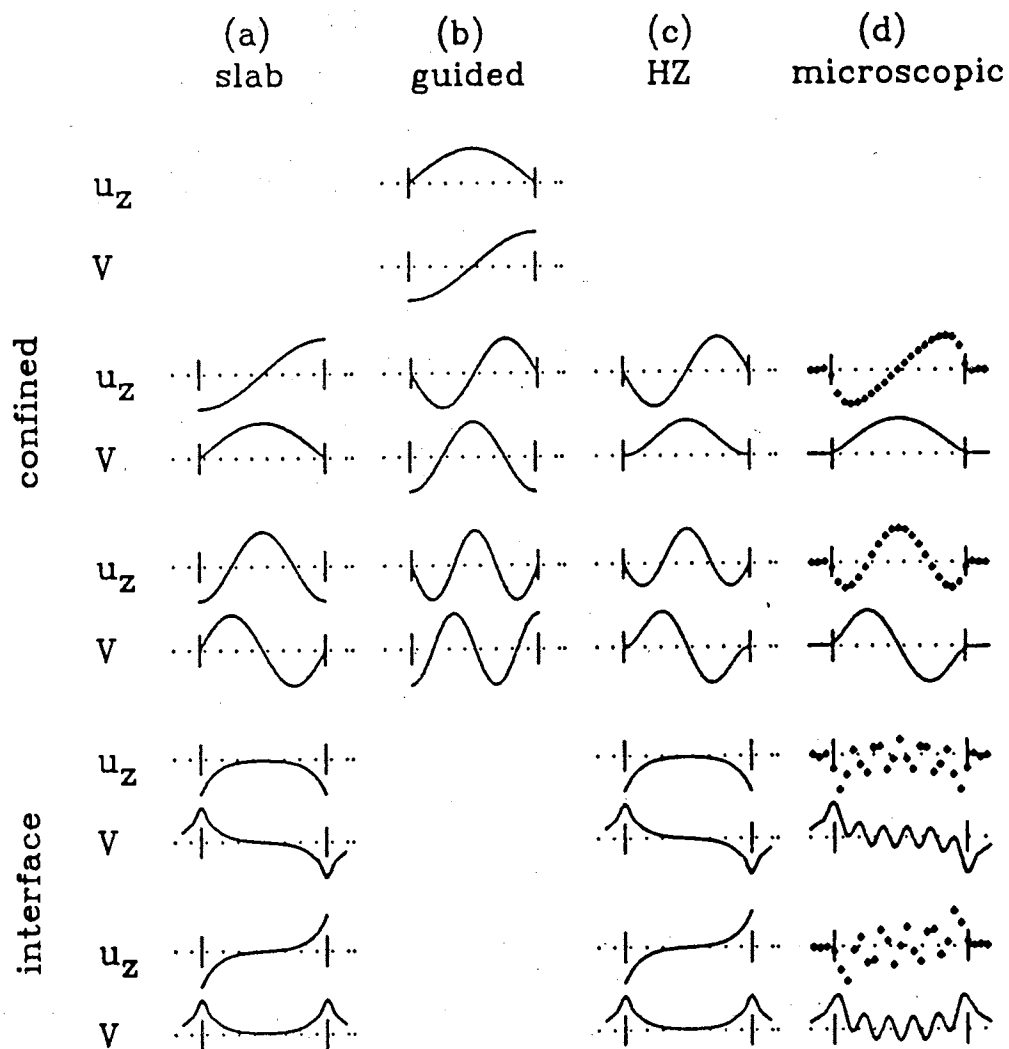


Figure 14. A comparison between the displacement and potentials calculated from different phonon models. The small vertical lines indicate the boundaries of the well layer. The plots are for $q_z=0$ and $q_{||}=0.15 \text{ \AA}^{-1}$ (from Reference 42)

Guided Mode Model

This is usually referred to as the continuum model. The main difference between this model and the slab model is the boundary conditions used. In this case phonon confinement is imposed by requiring vanishing displacement at the interfaces. This, of course, will automatically eliminate the existence of interface modes which constitute one of the major drawbacks of this model. The only modes predicted by this model are the confined modes which have the following potentials [5,42,44]:

$$\Phi_n(z) = C \cdot \begin{cases} \sin(q_z z) + const, & n = 1, 3, 5, \dots \\ \cos(q_z z) + const, & n = 2, 4, 6, \dots \end{cases} \quad (26)$$

Ridley et al. uses this type of modes with $const=0$ meaning that the potentials have antinodes at the boundaries [44]. This approximation may not be too bad if the barriers are very high (i.e. AlAs layers) and the layer thicknesses are not too small ($L \geq 100 \text{ \AA}$).

Huang and Zhu Model

In an attempt to critically modify the continuum model as applied to 2-D semiconductors, Huang and Zhu (HZ) have developed a model that satisfies both the electrodynamic boundary conditions and the continuity of the displacements at the interface [45,46]. This is based on a "microscopic" type of approach to the dielectric continuum model. They, essentially, modeled the superlattices formed with materials A and B as simple cubic lattice of oscillators, associated with corresponding electric dipoles. This is possible if one uses a rigid shift $\Delta\omega_0^2$ of the dispersion of material B with respect to A. This shift is then considered as an added perturbation (not necessarily small) to a lattice of A oscillators. The phonon potentials developed for the confined modes in this model are expressed in the following form [42,45]:

$$\Phi_n(z) = C' \cdot \begin{cases} \sin\left(\frac{\mu_n \pi}{L_z} z\right) + C_n \frac{z}{L_z}, & n = 3, 5, 7, \dots \\ \cos\left(\frac{n \pi}{L_z} z\right) - (-1)^{n/2}, & n = 2, 4, 6, \dots \end{cases} \quad (27)$$

with $\mu_3 = 2.86$, $\mu_5 = 4.91$, $\mu_7 = 6.95$, $C_3 = 1.95$, $C_5 = -1.98$, $C_7 = 2.00$, and C' is

$$C' = \left[\frac{\hbar(\omega_{LO}^2 - \omega_{TO}^2)}{2\epsilon_{\infty}\omega_{LO}A} \right]^{1/2} \cdot \left\{ \int_{-L_z/2}^{L_z/2} dz \left[q_{\parallel}^2 \Phi_n^2(z) + \left(\frac{\partial \Phi_n(z)}{\partial z} \right)^2 \right] \right\}^{-1/2}$$

The original expression of the phonon modes in this model have caused a lot of confusion due to a rather strange numbering of the confined modes [45]. It also added to the already existing controversy on which of the modes are represented by sines and which are represented by cosines. It was not until very recently that some promising attempts were made to clarify the origin of this confusion [42,47]. On one hand, the sophisticated microscopic calculation by Rucker et al. successfully presented a rigorous and solid ground for comparing all the phonon models [42]. On the other hand, the recent reformulation of the slab model has led Weber [47] to the conclusion that the $n=1$ mode simply does not exist in the HZ model and the odd modes numbering should start at $n=3,5,7\dots$ as shown in Equation 27. Thus the odd modes numbering is augmented by two compared to the continuum model while the even modes retain the same numbering. The HZ model is thus far the most widely accepted model in describing the electron-LO phonon interactions in QW's and SL's.

Microscopic Models

These types of models are rather complicated and difficult to use. Most of them require a lot of computer time and power. They are usually used in very simple sample structures to test other easier models such as those presented above. Recently a very sophisticated microscopic model was presented by Baroni et al. and Rucker et al.[11,48]. The model is based on first-principles calculations of the phonon modes in a 2-D semiconductor system using norm-conserving pseudopotentials in a density-functional linear-response theory. In their report, Rucker et al.[42,48] pointed out the inadequacy of the guided mode model in describing

the e-ph interactions in a 2-D semiconductor. The results of this model have led to resolving the long-standing controversy between the guided mode model that predicts small e-ph scatterings compared to the other models. As a result of this the guided mode model is becoming more and more questionable whether it can properly describe the phonon modes in 2-D semiconductor systems.

Hot Electron Cooling in GaAs/Al_xGa_{1-x}As QW's

Carrier-Carrier Cooling

Due to carrier confinement and the appearance of subbands, a detailed theoretical account of carrier-carrier (c-c) scattering is very complicated. Both intrasubbands and intersubbands scatterings have to be considered in addition to the nonparabolicity of the valence bands in narrow wells. Intrasubband c-c scattering has been studied previously in absorption experiments and found to be extremely fast. For instance, c-c scattering times on the order of 25 fs have been reported recently [16] for moderate carrier densities ($\sim 10^{18}$ cm⁻³). Intersubband carrier scattering was also measured using time-resolved Raman scattering and found to be on the subpicosecond range [24,49,50]. Considering the interaction times involved, it is important to note that c-c scattering is the most important cooling mechanism for the hot carriers in the initial 100 fs. This process will cool down the electrons to a nonequilibrium Fermi-Dirac distribution [27]. Intervalley scattering is the second most important initial cooling mechanism since it takes typically less than 100 fs to scatter an electron from the Γ valley to the X or L valley [16,25]. The return of the electrons from the satellite valleys to the Γ valley is a long time process because of the different density of states mass involved [51]. This process will not be important in the time scale of our picosecond Raman experiments.

Carrier-Phonon Cooling: Fröhlich Interaction

This is the main path for cooling the Γ valley electrons and generating the nonequilibrium phonon population studied in our experiments. This phonon build up leads to the so-called "hot phonon effect" which is manifested in the slowing down of the carrier cooling due to reheating by absorption of hot phonons. This was once a controversial issue among scientists until concrete experimental and theoretical evidence was reported by several groups [26,29,52,53]. The presence of this non-equilibrium phonon population is only possible due to the long phonon lifetime ($\tau_{LO} \simeq 7$ ps at 5 K) [21–24,54] compared to the e-LO phonon scattering time which is on the order of 200 fs [7,25,55]. Even for bulk GaAs, the theoretical models for calculating the phonon lifetimes are rather complicated and only give estimated values. The experimental results, however, are more accurate and show practically no difference between the phonon lifetimes in bulk GaAs and a variety of GaAs/ $\text{Al}_x\text{Ga}_{1-x}\text{As}$ QW samples and bulk $\text{Al}_x\text{Ga}_{1-x}\text{As}$ alloys [21–24,54].

The matrix element of the Fröhlich interaction is proportional to $1/q$ (see Equation 12) causing this scattering process to be dominated by small q phonons. This is clearly seen in the phase space distribution of the hot phonon occupation shown in Figure 15 at several times after excitation for a single QW. This result is obtained by Pötz and Kocevār assuming bulk GaAs phonons [29]. The distribution is clearly weighted heavily near the small q region at times $\tau_{e-LO} < t < \tau_{LO}$. Notice the drastic reduction of the small- q phonons after about 5 ps due to the LO phonon decay. Notice also the drastic reduction of the large- q phonons after 5 ps illustrating their involvement in the rapid process of intervalley scattering. In QW's, due to confinement of the modes the minimum phonon wavevector probed by Raman scattering experiments is $\frac{\pi}{L_z}$. This q is quite large compared to the minimum q for bulk. For comparison, we show in Figure 16 the calculated phase space phonon occupation number for bulk GaAs case [30]. This increase in the minimum phonon wavevector will significantly reduce the Fröhlich scattering in

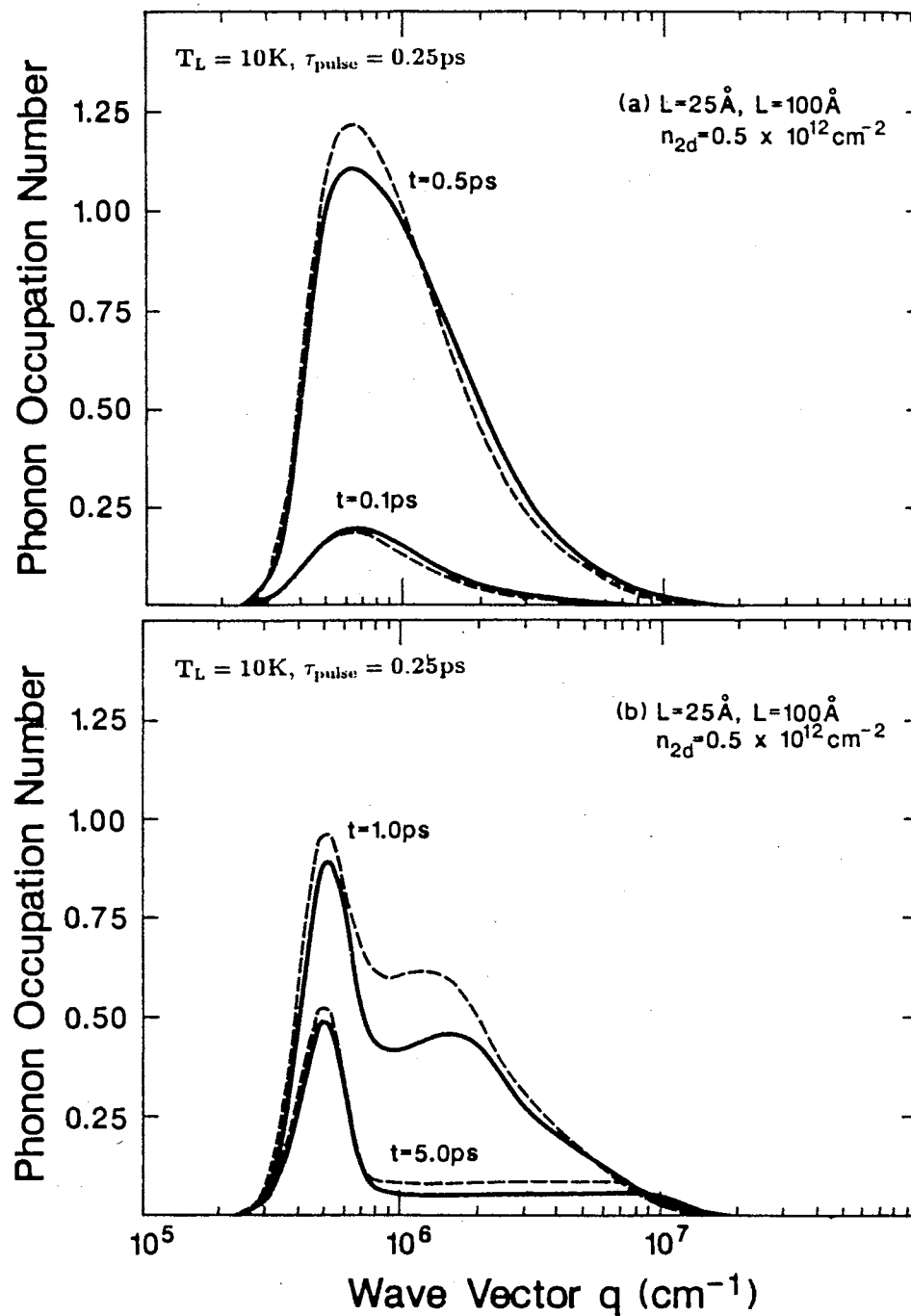


Figure 15. Phase space distribution of the hot phonon population at different times after excitation for a GaAs quantum well. The solid (dashed) curve is for $L_z=25 \text{ \AA}$ (100 \AA) (from Reference 29)

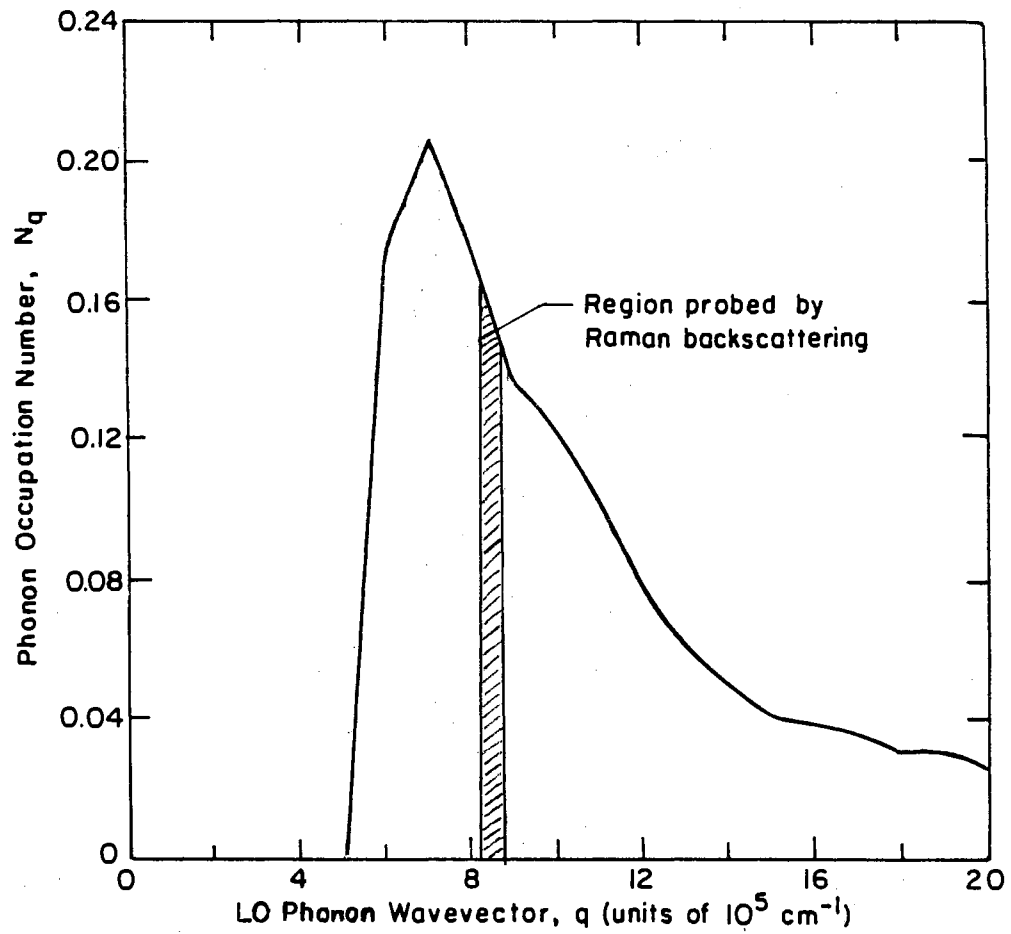


Figure 16. Phase space distribution of the hot phonon population at a time delay of about 3 ps for bulk GaAs. The marked region is for an excitation at 532 nm (from Reference 30)

QW's compared to bulk GaAs. This is clearly seen in our experiments as will be discussed in the following two chapters.

Acoustic phonons, on the other hand, have long interaction times with the electrons; on the order of tens of picoseconds [29]. Thus, their role in the cooling process of hot carriers comes in much later times and will not be significant in the time scale of our experiments.

Carrier-Phonon Cooling : Deformation Potential Scattering.

The matrix element for this c-ph interaction is either independent of q or proportional to \sqrt{q} . Thus, this process is more efficient for interactions involving large- q phonons. For instance, intervalley scattering would be the most efficient deformation potential scattering since it involves mostly zone-edge phonons with large q . From the deformation potential scattering selection rules, the following phonons can participate in the intervalley scatterings indicated on the left hand side [56]:

$$\begin{aligned}
 \Gamma &\iff X, && \text{X point LO phonons} \\
 X &\iff X, && \text{X point LO phonons} \\
 X &\iff L, && \text{all L point phonons} \\
 L &\iff L, && \text{X point LO and LA phonons} \\
 \Gamma &\iff L, && \text{L point LO and LA phonons}
 \end{aligned}$$

For instance, the scattering by TO and TA phonons are forbidden for a Γ to X and a Γ to L valley.

CHAPTER V

CONFINED-TO-PROPAGATING LO PHONON TRANSITION

Introduction

The problem of localization of elementary excitations in solids is of fundamental importance in physics [57]. Recently, there has been considerable interest in the confinement of phonons in GaAs/Al_xGa_{1-x}As superlattices (SL's) and multiple quantum wells (MQW's) [4,9,58-66]. This has been particularly so in connection with the ultrafast hot carrier relaxation in these systems through the Fröhlich electron-LO phonon interaction [5,21-24,30,49,67-69]. The nature of the LO phonon confinement affects the electron-LO phonon scattering rate which governs much of the ultrafast hot electron relaxation. It is well known that optical phonons in GaAs/AlAs SL's or MQW's are almost perfectly confined due to the large difference in the frequencies of the optical phonons in these two materials [58-60]. The optical phonons confined within the GaAs layers (referred to as wells) are believed to penetrate only one monolayer into the AlAs layers (barriers) and vice versa [9,58-63]. When the barrier is an Al_xGa_{1-x}As alloy instead of AlAs, the problem of phonon confinement becomes more complicated [4,64,65]. For instance, the penetration depth of the GaAs LO phonons into the Al_xGa_{1-x}As barriers is still unknown. Since there exists a partial overlap in energy between the GaAs and GaAs-like LO modes, especially for small x, it is possible that the LO phonon wave functions extend over several periods [62,64,65]. This leads to the concept of propagating optical phonons much like that of folded acoustic phonons [58,59,64]. The question of whether the optical phonons are confined or propagating thus should be answered depending on the value of x as well as the layer widths.

In this chapter we discuss the dependence of confined and propagating optical phonons in SL's on the barrier width L_b . Using the time resolved Raman

scattering technique described in Chapter III, we have investigated the two series of GaAs/Al_xGa_{1-x}As SL's with x=0.4 and x=1. Each series was grown with a fixed L_z=100 Å while the L_b's varied. Our most exciting findings are: (1) LO phonons in the GaAs/Al_xGa_{1-x}As SL's make a transition from the confined to the propagating regime when the barrier width becomes thinner than 20 Å for x=0.4 and 11 Å for x=1. (2) the transition is very sharp, occurring within 5 Å of the barrier thickness for both series.

Phonon Confinement

SL's and QW's are formed by alternatively growing two different materials one on the top of the other. Although the GaAs and AlAs are lattice matched to within about .1% there is however a large difference in the cation masses between the two materials. This corresponds to $\omega(\mathbf{k})$ branches for the optical phonons that are well separated and rather flat for the bulk materials. Typical dispersion curves are shown in Figure 17 for bulk GaAs and AlAs. Thus, a phonon mode with a given frequency in one material has no counterpart of the same frequency in the other. The optical phonons are thus confined to one material or the other and decaying exponentially beyond the interfaces. The SL structure enhances the periodicity in the z direction allowing for the folding of the Brillouin zone into a mini-Brillouin zone or SL Brillouin zone. This folding causes new modes to appear at the zone center ($\mathbf{k}=0$). These modes can now be Raman active and accessible by optical experiments. Figure 17 illustrates in (a) the zone folding for a GaAs/AlAs SL with L_z=5 ML (or monolayer, where 1ML \simeq 2.83 Å for GaAs) and L_b=4 ML [63].

The confinement of optical phonons in GaAs/AlAs SL's and QW's has been demonstrated experimentally using cw Raman scattering, first by Jusserand et al. [61]. Several peaks have been observed with down shifted frequencies from the bulk LO phonon frequency. These modes are labeled LO_n where n=1,2,3... and n=1 being the highest frequency or first confined mode. From a linear chain model with alternating AB/AC structure where A=As, B=Ga, and C=Al, we can obtain

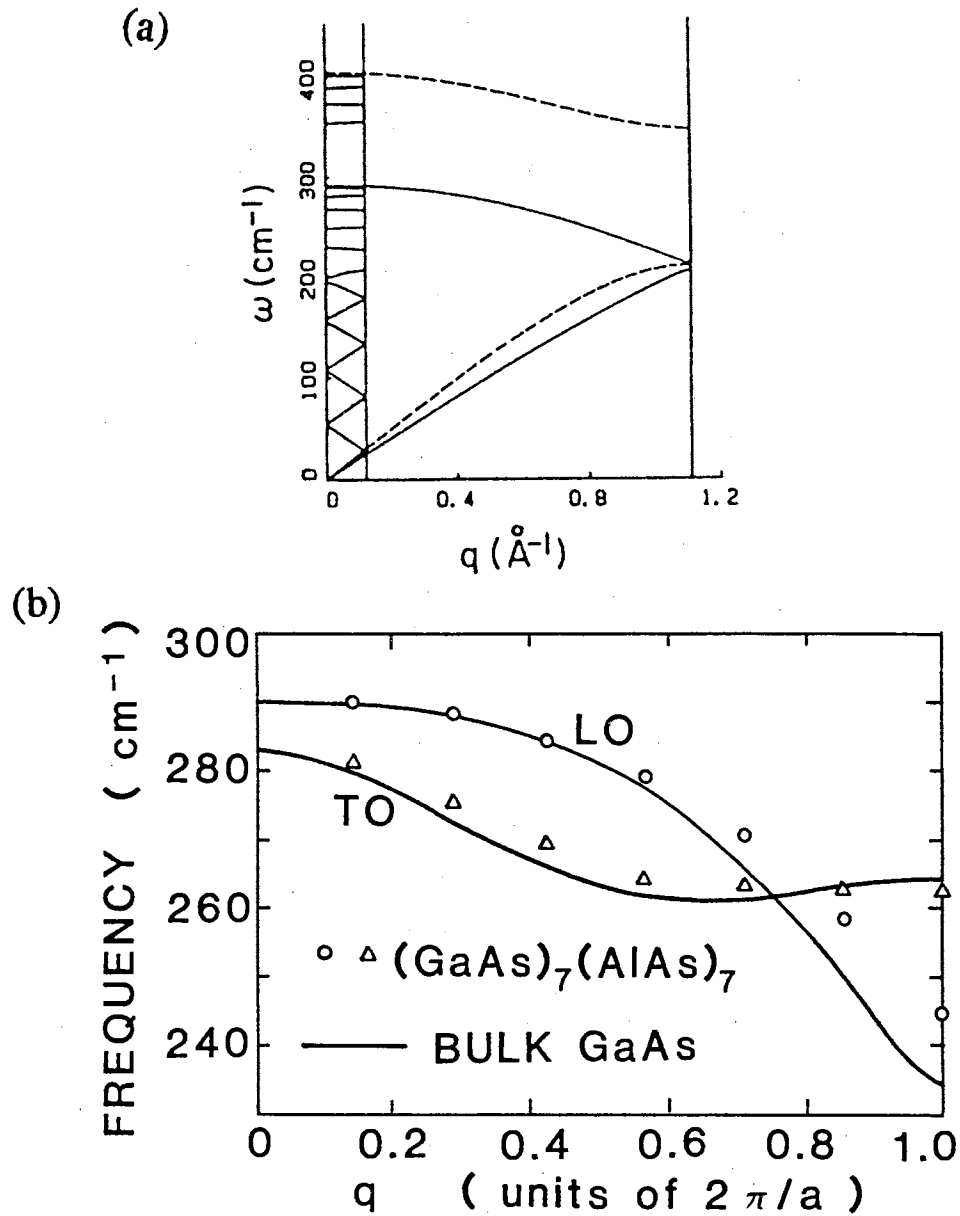


Figure 17. (a) Calculated phonon dispersion curves for $L_z=5$ ML, $L_b=2$ ML, and $x=1$ showing the Brillouin zone folding. Superimposed are the GaAs bulk (solid) and AlAs bulk (dashed) dispersion curves. (b) Calculated and measured GaAs LO and TO frequencies for $L_z=L_b=7$ ML and $x=1$ (from References 63 and 70, respectively)

an expression for the quantized phonon wave vector in the z direction as follows [59];

$$q_z = \frac{n\pi}{(n_1 + 1)a_1}, \quad n = 1, 2, 3, \dots \quad (28)$$

Where n_1 is the number of monolayers of a specific material and a_1 is the monolayer thickness (i.e. $a_1 = 1$ ML). Equation 28 is usually approximated by the expression obtained from a particle in the box type of analysis. This is given by [4]

$$q_z = \frac{n\pi}{L}, \quad n = 1, 2, 3, \dots \quad (29)$$

Where $L = n_1 a_1$ is the thickness of the layers. Equation 29 is a reasonably good approximation as long as the difference between L and $(n_1 + 1)a_1$ is not too large as is the case for small layer thicknesses.

From the cw Raman spectrum we can then map out the LO phonon dispersion curves for the bulk constituents materials of an SL sample. This is done by associating each of the LO_n peak observed in the cw Raman experiment with the corresponding wave vector determined from Equation 28. This is particularly important for materials such as AlAs which are not available in the bulk form. Figure 17 shows in (b) the measured and calculated GaAs bulk phonon dispersion curves for the LO and TO modes obtained from an SL sample with $L_z=L_b=7$ ML [70]. The cw Raman selection rules are such that the even modes ($n=2,4,6,\dots$) and odd modes ($n=1,3,5,\dots$) are observed in the polarized and depolarized Raman spectra, respectively [4].

Previously, most of the information concerning the confinement of LO phonons in SL's and MQW's has been obtained from cw Raman scattering [4,9,58–64]. In a cw Raman experiment, the confinement is observed in the form of a shift in the LO phonon frequency to lower energy, or the observation of multiple peaks with down shifted frequencies [4]. However, the frequency shift is too small to observe unless the quantum well is much thinner than 100 Å due to the relatively flat LO phonon dispersion curve. It is also very difficult to resolve the question of confined or propagating LO phonons by cw Raman scattering even when the

wells (or barriers) are substantially thin such that multiple peaks corresponding to different points in the Brillouin zone are observed. Another technique to probe phonon confinement in SL's and MQW's has been discussed recently by Kim and Yu [27,28,66,71]. This is the same technique described in Chapter III and referred to as one-beam-excite-and-probe. As shown in Figure 16 of Chapter IV, Raman active LO phonons usually occupy a narrow strip of the LO phonon phase space distribution, typically with nonequilibrium phonon occupation numbers near the peak of the distribution [26,30]. In bulk materials, the Raman active wave vector ($q=q_0$) is determined by the energy-momentum conservation of the scattering process. In our backscattering configuration we have

$$q_0 = \frac{4\pi n}{\lambda} \cos \theta = 8.4 \times 10^5 \text{ cm}^{-1} \quad (30)$$

where n is the index of refraction ($n=3.6$ for GaAs), λ is the laser wavelength, and θ is the incidence angle external to the sample (i.e. the angle between the normal to the sample and the incident laser). For confined optical phonons, q is primarily determined by the L_z 's as can be seen in Equation 29. Away from resonance, the first quantized LO phonon mode is the most Raman active [58,59]. For the GaAs LO mode of our samples this corresponds to

$$q_z = \frac{\pi}{L_z} = 3.1 \times 10^6 \text{ cm}^{-1} \quad (31)$$

This difference in the q between bulk and confined phonons has a significant effect on the phonon generation rates. This is due to the $1/q$ dependence of the Fröhlich electron-LO-phonon interaction Hamiltonian which is responsible for the nonequilibrium phonon distribution. Using Equations 30 and 31, the $1/q$ dependence results in the following factor:

$$\beta = \left(\frac{q_z}{q_0} \right)^2 = \left(\frac{3.1 \times 10^6 \text{ cm}^{-1}}{8.4 \times 10^5 \text{ cm}^{-1}} \right)^2 \simeq 13$$

Thus, about a factor of 13 reduction is expected in the generation rate of the confined LO phonons compared with that of bulk LO phonons.

Using this technique, Kim and Yu have recently observed a continuous reduction of the hot phonon generation in a series of GaAs/AlAs samples with decreasing well widths [27,66]. This observation was explained by the increasing Raman wave vector with decreasing L_z 's, thus resulting in a small generation rate due to the $1/q$ dependence. Unlike confined phonons, propagating phonons can have Bloch wave vectors equal to those in bulk materials [4,63]. This results in a bulklike generation rate of the Raman active phonons. Since our picosecond Raman scattering technique is very sensitive to the magnitude of q , it has proved to be an ideal tool to investigate whether optical phonons are confined or propagating in SL's.

Experimental Results

Typical hot phonon Stokes and anti-Stokes Raman spectra are shown in Figure 18. The peaks labeled LO_1 are the GaAs Stokes and anti-Stokes phonons in the well layers. The other peak labeled LO'_1 is the Stokes component of the GaAs-like LO phonon from the barrier layers. Notice in particular the drastic reduction of the anti-Stokes peak LO_1 in (b) as L_b increased from 5 Å to 50 Å due to confinement. The 7 cm^{-1} width of the laser pulses used is narrow enough to resolve both the GaAs and GaAs-like LO peaks for the $x=0.4$ series. In this chapter, we will mainly concentrate on the GaAs LO phonons unless otherwise specified. In order to determine the hot phonon population N_q from our Raman spectra, we have to measure the Stokes (I_S) and anti-Stokes (I_{AS}) integrated intensities. These intensities are related to N_q through the Raman cross sections as follows:

$$I_S(\omega_i) = I_0 \sigma_S(\omega_i) \cdot (N_q + 1) \quad (32)$$

$$I_{AS}(\omega_i) = I_0 \sigma_{AS}(\omega_i) \cdot N_q \quad (33)$$

where σ_S and σ_{AS} are the Raman cross sections for Stokes and anti-Stokes respectively and I_0 is the excitation intensity. For nonresonant Raman scattering it is known that the following relation holds [26,72]:

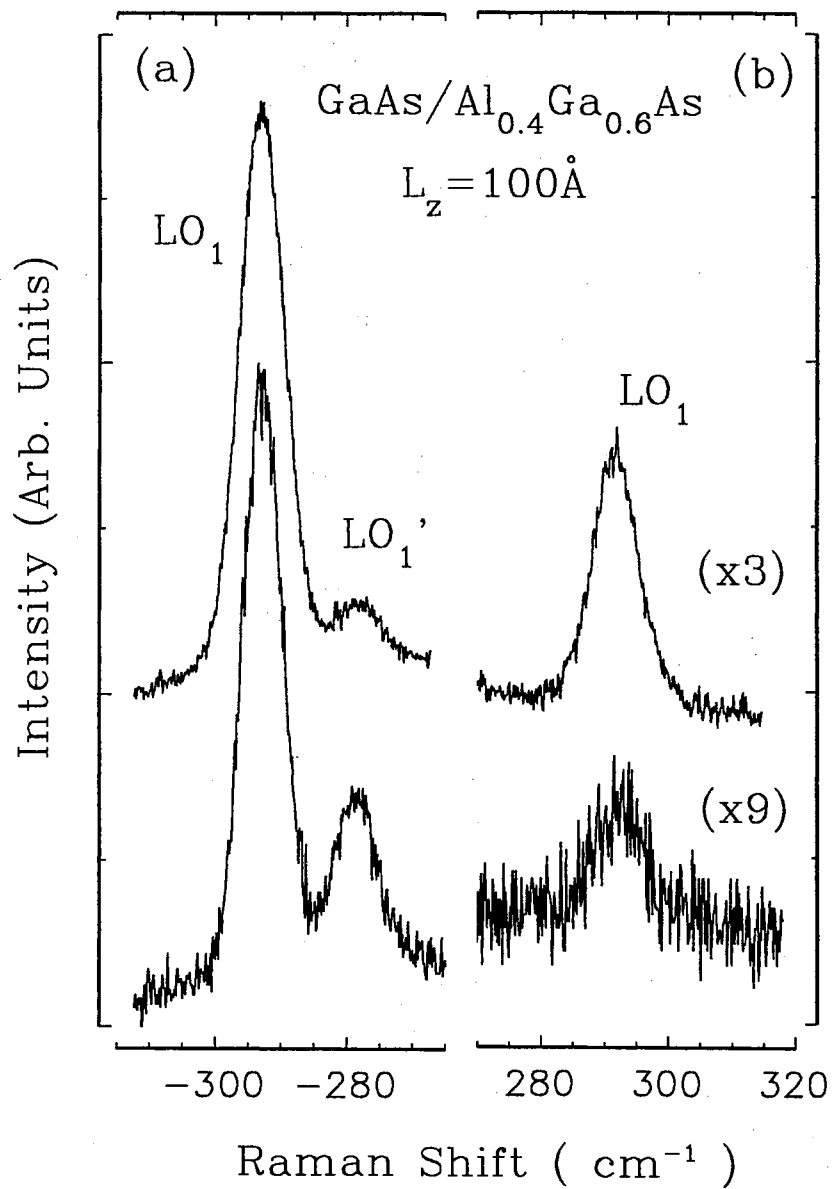


Figure 18. Typical Stokes (a) and anti-Stokes (b) Picosecond Raman spectra. The upper and lower spectra are for $L_b = 5 \text{ \AA}$ and $L_b = 50 \text{ \AA}$, respectively ($T = 16 \text{ K}$)

$$\sigma_S(\omega_i) = \sigma_{AS}(\omega_i) \quad (34)$$

Using this to solve Equations 32 and 33 for N_q we obtain the following result:

$$N_q = \frac{1}{\frac{I_S}{I_{AS}} - 1} \quad (35)$$

It is important to note that we always keep a bulk GaAs sample in the dewar next to our SL samples. The purpose of this is to normalize our measured phonon populations to that of bulk GaAs and minimize the sources of error. The bulk sample also provides us with a reference point to keep our experimental conditions the same from day to day. This is done by adjusting the excited carrier density to yield $N_q \simeq 0.3$ for bulk GaAs.

At resonance with an excitonic transition Equation 35 no longer holds. This is due to the invalidity of Equation 34 since, in general, the Stokes and anti-Stokes Raman scattering cross sections would be affected differently by the resonance. The effect of any such resonances has been carefully checked by measuring the Stokes intensity as a function of the lattice temperature between 15 and 300 K. This is possible since the change in the band gap energy over this temperature range is much larger than the LO phonon energy. No significant enhancement was found except for the samples with $x=0.4$, $L_b=20$ Å, and $x=1$, $L_b=6$ Å. To compensate for the resonance effect on these samples, we have performed our experiments at 170 K and used the thermal phonon population to obtain a correction factor. The thermal phonon population is given by

$$N_{th} = \frac{1}{\exp\left(\frac{\hbar\omega_{LO}}{kT}\right) - 1}$$

N_{th} is then measured at very low carrier densities (to reduce the hot phonon population) by enlarging the laser spot size on the sample. The correction factor is then obtained by comparing the calculated and measured N_{th} .

In our experiments, we measure the dependence of N_q on the laser power P to extract the low carrier density regime. A plot of N_q versus P is shown in

Figure 19 for two QW samples and bulk GaAs. Notice the linear dependence that prevails at low powers which increases our data redundancy. The slope of this line (dN_q/dP) is measured and compared to that of bulk GaAs. Considering the linear dependence of N_q on P , the laser pulse duration, and the low carrier densities used in our experiments, we can rule out the presence of any phonon relaxation effects. This is due to the fact that the Raman active LO phonon population in our case is still rising and has not yet reached its maximum (at ~ 2 -3 ps) [21,22,30,68,69]. This is consistent with experiments that showed the LO phonon lifetime to be rather insensitive to alloying or superperiodicity [21,22,24,68]. Thus, dN_q/dP is proportional to the average generation rate of the Raman active LO phonon (dN_q/dt) for a fixed laser pulse width. We directly use dN_q/dt as our experimental data. A plot of dN_q/dt normalized to that of bulk GaAs is shown in Figure 20 as a function of L_b for two series of GaAs/ $Al_xGa_{1-x}As$ SL's with $x=1$ and $x=0.4$.

For SL's with $x=0.4$ and $L_b \geq 20 \text{ \AA}$, or those with $x=1$ and $L_b \geq 11 \text{ \AA}$, the dN_q/dt 's are around 10 % that of bulk GaAs. The fact that we observe almost the same dN_q/dt over such wide ranges of x and L_b indicates that the hot phonon generation is rather insensitive to the detailed electronic band structure. This is probably because the momentum-energy conservation of the electron-phonon scattering, which would result in smaller dN_q/dt with increasing electron confinement [27,44,66], is relaxed due to the interface imperfections [21,22,24,64]. As a result, the hot phonon generation rate is mainly governed by the number of photoexcited electrons and the magnitude of the Raman active wave vector, not by the detailed electronic band structure. The confined phonons in both $x=0.4$ and $x=1$ series are also consistent with the off-resonance Raman selection rules [58,59].

In Figure 18 we have seen the presence of the GaAs-like barrier phonon peak (LO'_1). There are two other Raman active modes called AlAs and AlAs-like present in the barrier layers. We have found dN_q/dt of these barrier phonons to be too small in these samples even when the barrier was sufficiently thick to allow for a significant Raman cross section. This is easily understood since the barrier

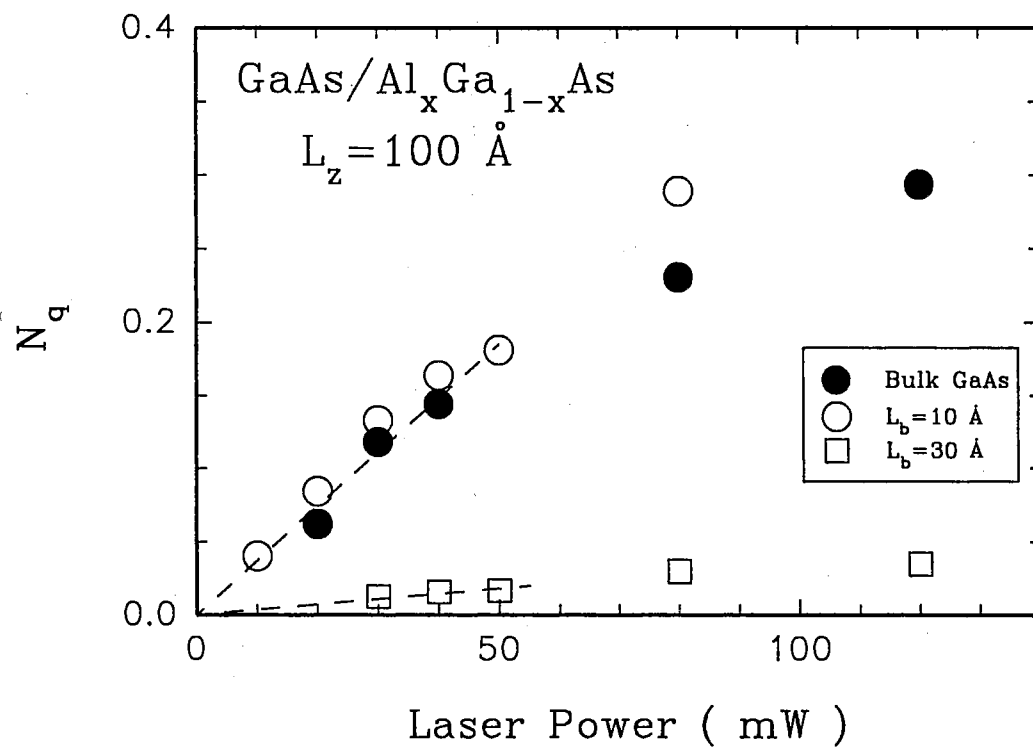


Figure 19. N_q versus the laser power for bulk GaAs and two QW samples illustrating the drastic difference between the confined and propagating LO phonons

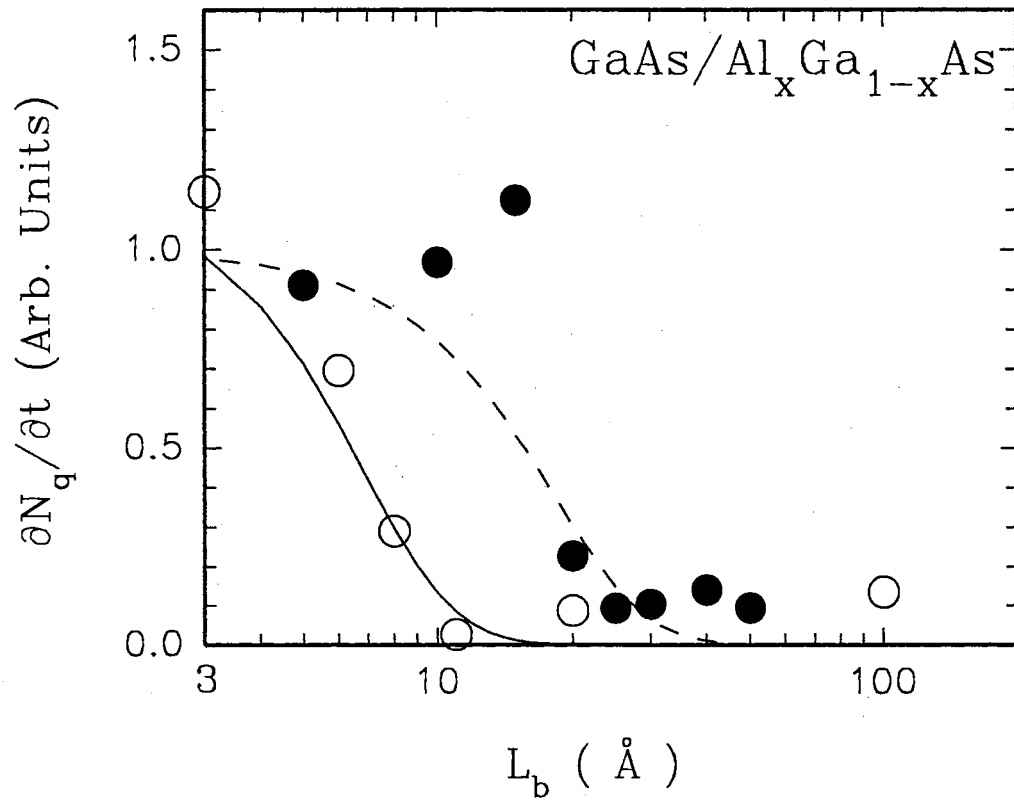


Figure 20. Measured hot phonon generation rates of GaAs LO phonons as a function of L_b for $x=1$ (open circles) and $x=0.4$ (solid circles). The curves are fits described in the text

phonons are now faced with the 100 Å thick GaAs layers acting as "phonon-barriers". In addition, most of our samples have barrier layers that are at most half the thickness of the GaAs wells leading to a larger q for these phonons and a much smaller dN_q/dt compared to that of confined GaAs LO phonons. From this observation, we conclude that the GaAs-like, AlAs-like, and AlAs LO phonons of the barriers are all well confined for $x=1$ and $x=0.4$. In addition, it is also important to note that the excited hot carriers will have much lower excess energy in the barrier region leading to very small populations of the barrier phonons.

Between $L_b=15$ Å and 20 Å for the $x=0.4$ series, and $L_b=6$ Å and 11 Å for the $x=1$ series, dN_q/dt shows a sudden increase to almost the same value as that of bulk GaAs. The Raman active nonequilibrium phonon population of bulk GaAs is already close to the peak of the hot phonon distribution. This excludes effects such as interface imperfection and electron confinement to be possible causes to this sudden increase in dN_q/dt . These factors tend to broaden the nonequilibrium distribution and thus decrease the generation efficiency relative to bulk GaAs [21,22,27,66]. Another possible factor is intervalley scattering which is important in picosecond and subpicosecond cooling of the hot electrons. As discussed in Chapter IV, it only takes about 100 fs or less to remove the high energy electrons from the Γ valley [16,25,27,28,25,69,71]. However, Kim and Yu have recently shown that intervalley scattering rates are essentially the same for bulk GaAs and quantum wells of the order of 100 Å or larger [66]. This can be easily understood since intervalley scattering involves zone edge phonons. These phonons have large wave vectors and are not measurable by a light scattering experiment. Furthermore, the electrons that undergo intervalley scattering are not very efficient in producing Raman active hot phonons since they remain mostly in the L or X valley within our time scale [33]. Therefore, the effect of intervalley scattering on our samples is practically constant.

We have also performed our picosecond Raman scattering experiments using the dye laser described in Chapter III. The purpose of these experiments is to check for any energy dependent effects such as band structure and intervalley

scattering. We have performed similar picosecond Raman scattering experiments at different excitation energies. We checked for intervalley scattering effects on our measured hot phonon generation rates by exciting the carriers just above and below the X valley minima. Our results showed no significant change in the measured hot phonon generation rate. Therefore, the effect of intervalley scattering on our measurements should be very small and negligible. In Figure 21 we show the measured hot phonon generation rate for the $x=0.4$ series at 2.33 eV and 2.10 eV excitations. It is clear from the figure that the results are very similar indicating that any band structure effects due to the variation in L_b is minimal. Our results are, thus, due to changes in the phonon properties.

Discussion and Conclusions

There is the possibility that the property of the interface phonons could be crucial in determining the penetration and the coupling of the optical phonons across the barriers since some of these phonons can penetrate the adjacent layers as much as the confined phonons do [73]. In general, these modes are not Raman active unless near a strong resonance as we mentioned in Chapter IV [64]. This is not the case in our experiments, therefore we do not observe such interface phonons. In addition, Tsen et al. have shown in a recent letter that the hot electron interaction with the interface phonons in GaAs/AlAs superlattices is weak for $L_z=70$ Å and decreases with increasing L_z [72]. In our samples with large L_z (100 Å), we expect the contribution of the interface phonons to our measured GaAs LO phonon population to be relatively small.

Due to the large range of x and L_b 's considered in our experiments, it is necessary to consider the effects of the energy band structure variations with L_b in more detail. We have, therefore, conducted photoluminescence (PL) and photoluminescence excitation (PLE) measurements on each sample series [74]. We have also calculated the electronic band structures using Schulman and Chang's tight binding model [35]. The observed changes in the electronic energy levels are rather slow and gradual although L_b changes over a wide range of values. This is

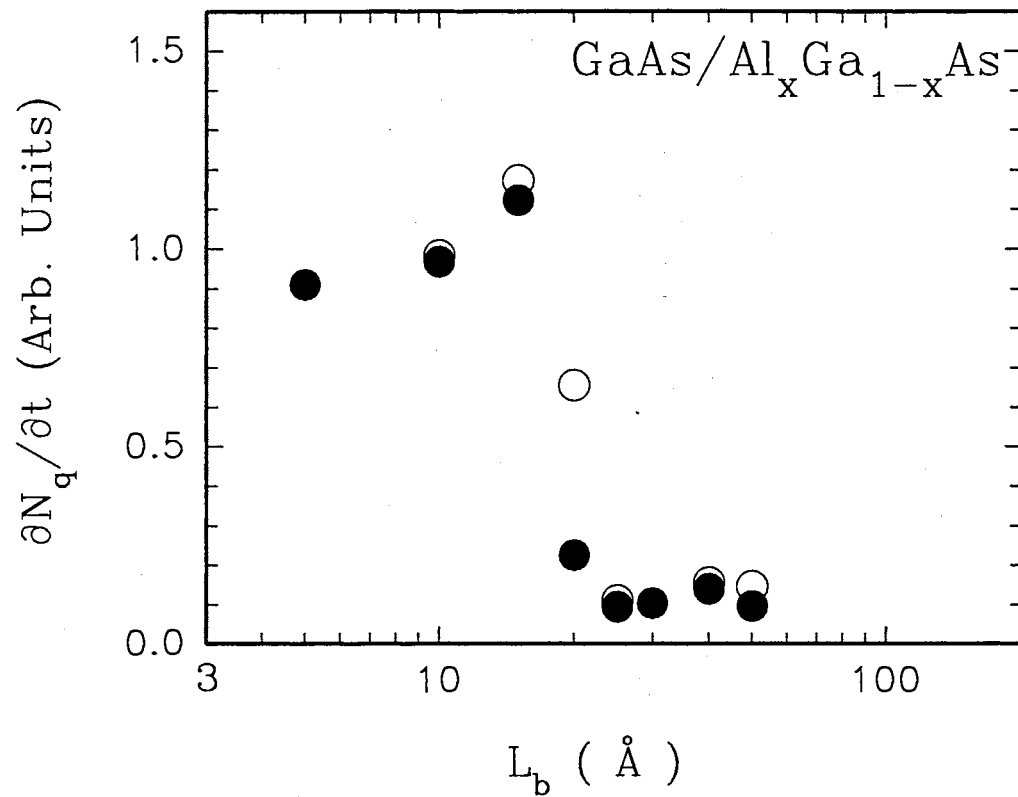


Figure 21. GaAs hot phonon generation rate as a function of L_b at two different excitation energies: 2.33 eV (solid circles) and 2.10 eV (open circles) for $x=0.4$

in contrast with our observed transitions at $x=1$ and $x=0.4$. Therefore, the effects of the electronic band structures variations with L_b only have a minor influence on our observed phonon generation rates. This is well supported by our results shown in Figure 21 where we observe a similar sharp transition for $x=0.4$ at two different excitation energies. Therefore, the observed changes in the phonon generation rates are mainly due to the changes in the phonon confinement.

From all of the above considerations, we conclude that the bulklike nonequilibrium phonon population observed in some of our SL samples is only possible if we have bulklike, extended optic phonon wave functions. Therefore the sudden increase in dN_q/dt is a clear indication of a sharp transition from the confined to the propagating optical phonons. The transition occurs when the LO phonon wave functions of adjacent wells begin to have phase coherence by coupling to each other in the barriers. This is the first time such transition from confined to propagating phonons has been observed [14]. To our knowledge, the transition we observe is thus far the sharpest localized-to-delocalized transition of any elementary excitations in SL's where only the layer widths are varied. The two observed transitions are rather sharp and reflect the unique capability of time resolved Raman scattering in probing the extent of LO phonon wave functions.

To show that the phonon generation rates of the propagating optic phonons can be indeed bulklike, we consider a wave function of a propagating Raman active mode that can be written in the following Bloch form:

$$\Psi(z) = U_q(z) \cdot \exp(iq_0z) \quad (36)$$

where $U_q(z)$ has the periodicity of the superlattice and q_0 is equal to that of bulk GaAs [9,75]. This mode is dominated by the bulklike Fourier component $\exp(iq_0z)$ when $U_q(z)$ corresponds to the first quantized mode (i.e. the half-wavelength mode with its peaks in the center of the GaAs wells as shown in Figure 14 of Chapter IV). In the limiting case of $L_b=0$, we obtain the bulk wave function since $U_q = 1$ in this case. Therefore, the phonon generation rate of the propagating Raman active mode is similar to that of bulk, consistent with our results.

The exact treatment of the phonon generation rates as a function of L_b is a rather involved theoretical problem and is beyond the scope of this chapter. As we have discussed in Chapter IV, a rigorous calculation of the electron-phonon interaction in QW structures is a rather complicated problem that still challenges theoretical physicists. In the following we will try to get some qualitative understanding of the observed dependence of dN_q/dt on L_b by applying a simple Fourier analysis to the phonon modes. We start by considering the Bloch form for the symmetric phonon wave function as in Equation 36 where now:

$$U_q(z) = \begin{cases} \cosh\left(\frac{z}{\lambda}\right) & \text{for } -L_b < z < 0 \\ A \cos\left(q\left(z - \frac{L_z}{2}\right)\right) & \text{for } 0 < z < L_z \end{cases} \quad (37)$$

with z being the coordinate along the growth direction and λ is a decay constant. The constant A can be determined from matching the two functions at the interface ($z=0$). This gives

$$A = \frac{1}{\cos\left(\frac{qL_z}{2}\right)} \quad (38)$$

We can Fourier expand Ψ to first order and obtain,

$$\exp(iq_0z) \cdot \cosh\left(\frac{z}{\lambda}\right) = b_0 \exp(iq_0z) + \dots \quad -L_b < z < 0 \quad (39)$$

$$A \exp(iq_0z) \cdot \cos\left(q\left(z - \frac{L_z}{2}\right)\right) = a_0 \exp(iq_0z) + \dots \quad 0 < z < L_z \quad (40)$$

Where a_0 and b_0 are the first Fourier expansion coefficients and are easily expressed as

$$b_0 = \frac{2\lambda}{L_b} \sinh\left(\frac{L_b}{\lambda}\right) \quad (41)$$

$$a_0 = \frac{4A}{qL_z} \sin\left(\frac{qL_z}{2}\right) \quad (42)$$

To first order approximation in the expansion of Ψ the GaAs phonon generation rate can be expressed in the following form:

$$\frac{dN_q}{dt} \propto \frac{|a_0|^2}{|a_0|^2 + |b_0|^2} \quad (43)$$

After substitution of a_0 and b_0 we get the following approximate expression for the hot phonon generation rate,

$$\frac{dN_q}{dt} \propto \frac{1}{\left[\frac{q^2 L_z^2}{4} \cot^2 \left(\frac{q L_z}{2} \right) \right] \frac{\lambda^2}{L_b^2} \sinh^2 \left(\frac{L_b}{\lambda} \right) + 1} \quad (44)$$

As we can see, Equation 44 clearly follows the trend that the GaAs LO phonon generation rate should increase with increasing well size L_z . In addition, the expression also shows a barrier with dependence of this generation rate similar to our experiment. The GaAs LO phonon wave function decays exponentially as it penetrates the barrier layer. This LO phonon penetration depth is fixed for a given x value of the barrier. We believe that when the barrier becomes thin enough the exponential decay is not complete and the phonon wave functions in adjacent wells are able to couple to each other in the barrier. This is manifested by an increase in the Fourier component (a_0) of the wave function. We have used Equation 44 with $q=q_0$ and λ as an adjustable parameter to fit our data for $x=1$ and $x=0.4$. The fit predicts rather well the observed phonon transition for both series of samples as shown in Figure 20. The values obtained for λ are 3 Å and 8 Å for $x=1$ and $x=0.4$, respectively. These values of λ will be discussed further in the next chapter. For the moment, it suffice to say that λ is related to the GaAs LO phonon penetration depth into the barriers.

As a conclusion to this chapter we would like to summarize what we have done so far. We have performed a systematic study of the generation of hot LO phonons in GaAs/ $\text{Al}_{0.4}\text{Ga}_{0.6}\text{As}$ and GaAs/AlAs SL's as a function of L_b . Using time resolved Raman scattering we have observed a sharp transition from confined to propagating LO phonons in both series of samples. This is the first time such a transition of LO phonons in GaAs/ $\text{Al}_x\text{Ga}_{1-x}\text{As}$ SL's and QW's has been

reported. We have therefore shown that the question of confined or propagating optic phonons in SL's should be answered carefully depending on the barrier widths and the alloy concentrations. A simple theoretical approach based on a Fourier analysis of the phonon modes was used to fit our hot phonon generation rate data. Good agreement was obtained between the data and calculation.

CHAPTER VI

LO PHONON PENETRATION DEPTH MEASUREMENTS

Introduction

The two-mode behavior of the optical phonons in the $\text{Al}_x\text{Ga}_{1-x}\text{As}$ barriers allows for considerable overlap in energy between GaAs and GaAs-like LO phonons (in the barrier) for small x . Similarly, the interface phonon modes also have dispersion curves lying between those of the different GaAs confined modes [4,8,42]. Therefore, it is possible to have extended optical phonon wave functions with folded zones much like acoustic phonons for small values of x . The possibility of propagating LO phonon modes in GaAs/ $\text{Al}_x\text{Ga}_{1-x}\text{As}$ SL's and MQW's has been suggested previously [4,9,63]. Recently, it has been shown using cw Raman scattering in ultrathin superlattices that the AlAs-like modes are indeed confined in the alloy barrier [76]. Whether the LO phonons are confined or propagating will have important consequences on the physics as well as the device applications of these GaAs/ $\text{Al}_x\text{Ga}_{1-x}\text{As}$ structures. This is because the electron-LO phonon interaction has strong effects on the hot electron mobility [77].

In this chapter, we investigate LO phonon confinement in several series of GaAs/ $\text{Al}_x\text{Ga}_{1-x}\text{As}$ SL's with aluminum concentrations ranging from $x=0.12$ to $x=1$. Using the time-resolved Raman scattering technique described in Chapter III we can determine the penetration depth of GaAs LO phonons into the alloy barrier regions. Our new and most important findings are: (1) the observation of a rapid increase in the GaAs LO phonon penetration depth (λ) into the $\text{Al}_x\text{Ga}_{1-x}\text{As}$ barriers as x decreases (for instance, λ is about 40 Å for $x=0.3$ and >80 Å for $x=0.2$); (2) the observation of extended unconfined GaAs LO phonons regardless of the barrier thickness for $x<0.3$. Thus, for most SL's with well-widths (L_z 's) of 100 Å or less, the GaAs LO phonons may be regarded as bulklike for $x<0.3$.

Experimental Results

In Figure 22 we show a picosecond Raman scattering spectra taken at 16 K from a QW sample with $x=0.20$ and $L_z=L_b=70$ Å. Through a careful lineshape fit to the spectra the hot phonon occupation numbers of AlAs-like (indicated by arrows), GaAs-like, and GaAs LO modes are determined. We have found the GaAs and GaAs-like LO phonons to show significant occupation numbers compared to bulk GaAs ($N_q \simeq 0.3$), whereas AlAs-like modes have an occupation number about 16 times smaller than that of bulk GaAs. Even after corrections for the number of modes [21,78,79], the higher frequency of the AlAs-like modes, and the smaller excess energy in the barrier, this is still 6 times less than what one would expect if the AlAs-like LO modes are propagating. These results indicate that both the GaAs and GaAs-like LO phonons are unconfined whereas the AlAs-like modes are confined. This is expected since the dispersion of the AlAs-like LO phonons in the barrier does not allow modes with frequencies corresponding to those in the GaAs well as discussed in Chapter IV.

The fact that the GaAs-like LO modes and the AlAs-like LO modes, both primarily in the barrier, show such a large (a factor of 4) difference in their hot phonon generation rates unequivocally demonstrates the unique capability of our technique to probe the spatial extent of the optical phonon wave functions. The comparison of our results with those of bulk GaAs and $\text{Al}_x\text{Ga}_{1-x}\text{As}$ alloys [7,21,78,79] indicates that under our experimental conditions, the hot phonon generation rate is determined primarily by the spatial extent of the Raman active LO phonons in the growth direction and the number of photoexcited electrons. This is true in spite of the considerable variation in the electronic band structure from sample to sample and the excitation energies ranging between 2 and 2.33 eV.

We have performed picosecond Raman experiments similar to those in the previous chapter on several series of samples with different x . The purpose of this study is to investigate the effect that x has on the observed confined-to-propagating

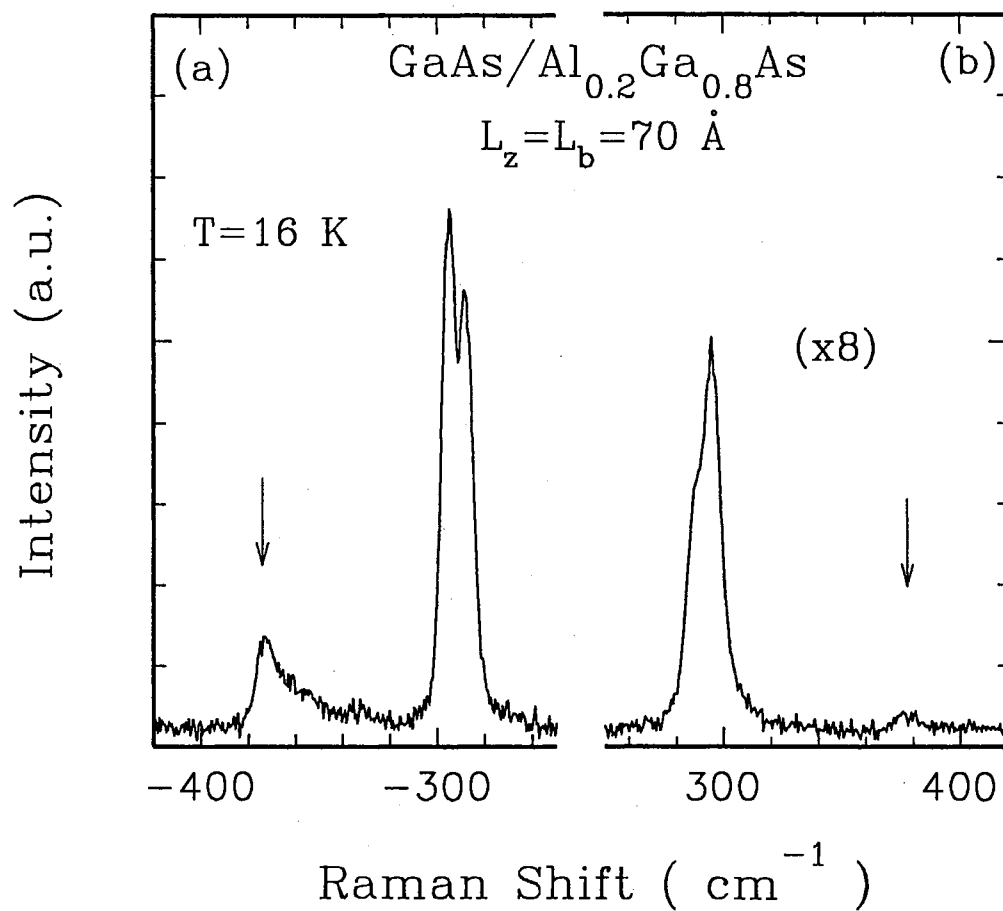


Figure 22. Picosecond Raman Stokes (a) and anti-Stokes (b) spectra obtained from a sample with $x=0.2$ and $L_z=L_b=70 \text{ \AA}$

LO phonon transition. In Figure 23 we show the non-equilibrium phonon generation rates dN_q/dt of the Raman active GaAs LO phonons as a function of L_b for the series of GaAs/ $\text{Al}_x\text{Ga}_{1-x}\text{As}$ samples with $x=0.3$. This data was obtained with our 2 ps pulses at 2.33 eV and at temperatures of 177 K and 16 K. The confined-to-propagating LO phonon transition is clearly observable in this series of samples as well. It is important to note, however that the transition occurs at a much larger barrier width compared to the results for the series of samples with $x=0.4$ and $x=1$ presented in the previous chapter. In this case, the critical barrier width is about 80 Å while for $x=0.4$ and $x=1$ this was 20 Å and 10 Å respectively. This result is consistent with the fact that by lowering x , essentially we are lowering the "phonon barrier height". Therefore, the critical barrier thickness required to confine the LO phonons in the well should increase with decreasing x . It is also important to note that the transition we observe for $x=0.3$ does not seem to be as sharp as the ones we observed for $x=0.4$ and $x=1$. From this result one might deduce that $x=0.3$ is possibly close to a critical x value where the confined-to-propagating LO phonon transition is starting to disappear.

This is exactly what we observe experimentally when we decrease the aluminum concentration below $x=0.3$. Figure 24 shows our measured hot phonon generation rates for several series of GaAs/ $\text{Al}_x\text{Ga}_{1-x}\text{As}$ samples with $x < 0.3$. As expected, we do not observe the confined-to-propagating LO phonon transition with decreasing L_b in these series of samples. The series of samples considered have $x=0.2$, $x=0.18$, and $x=0.12$. In all of these series of samples we measure hot phonon generation rates (dN_q/dt) that are comparable to that of bulk GaAs regardless of the barrier thickness considered. The results are consistent with each other and indicate that the GaAs LO phonons are no longer confined by the $\text{Al}_x\text{Ga}_{1-x}\text{As}$ barrier when x is less than 0.3. Thus, the GaAs LO phonons are in this case bulklike with wavefunctions that extend over several periods of the superlattice. To our knowledge this is the first experimental evidence of the existence of bulk-like extended LO phonons regardless of the barrier thickness in GaAs/ $\text{Al}_x\text{Ga}_{1-x}\text{As}$ QW's [80,81].

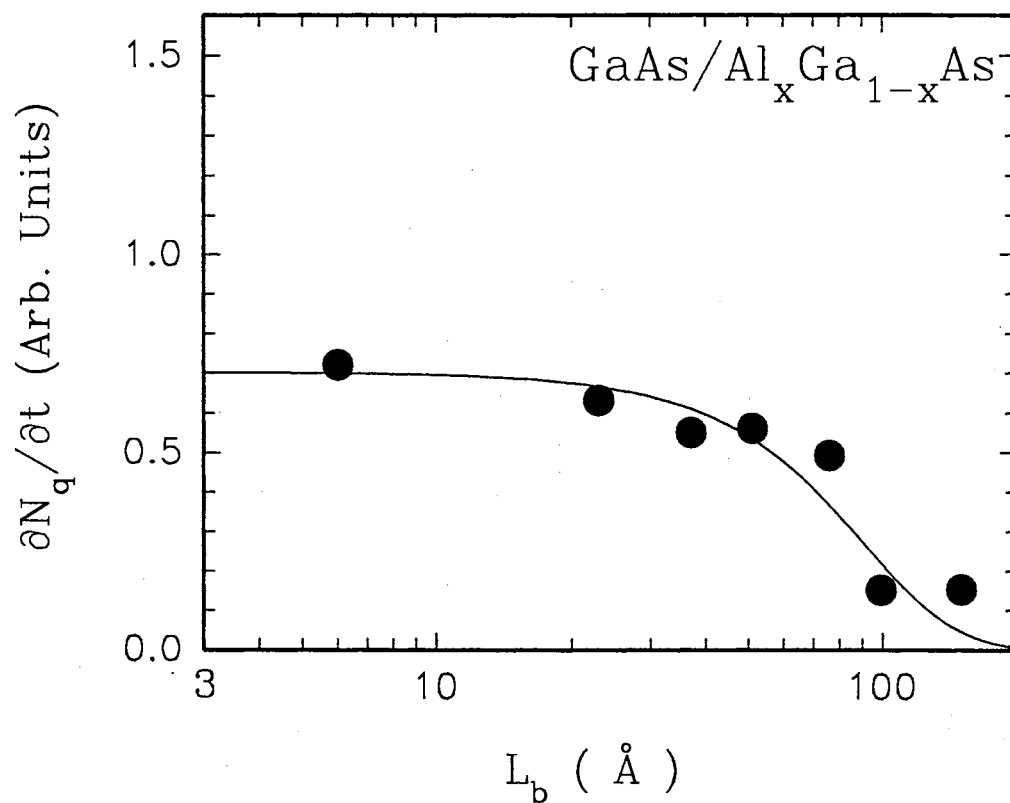


Figure 23. The generation rates of GaAs LO phonons plotted as a function of L_b for the series of samples with $x=0.3$. The curve is a fit discussed in the text

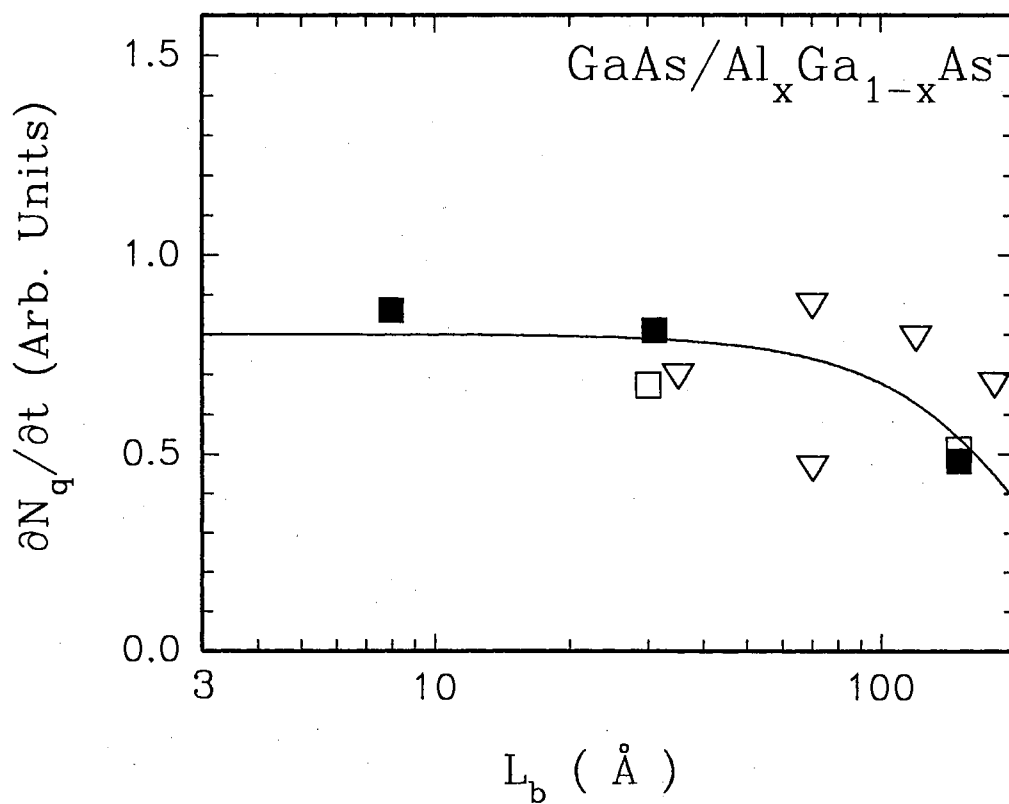


Figure 24. Hot phonon generation rates of the GaAs LO phonons as a function of L_b for several series of samples with $x < 0.3$. The individual series are denoted by open triangles ($x=0.2$), open squares ($x=0.18$), and filled squares ($x=0.12$). The curve is a fit discussed in the text

We would like to note that the two data points at $L_b = 70 \text{ \AA}$ and $x=0.2$ in Figure 24 represent two samples with different L_z 's. The lower data point is from the sample with $L_z = 70 \text{ \AA}$ and the upper one is from the sample with $L_z = 150 \text{ \AA}$. Notice in particular that the measured dN_q/dt is about a factor of two smaller for smaller L_z sample. This is consistent with the reduction in the scattering volume associated with the change in L_z .

The barrier widths at which the confined-to-propagating LO phonon transitions occur are very important experimental points. From these we are able to estimate the LO phonon penetration depth (λ) into the barriers. We do this by defining λ as 1/2 of the critical barrier thickness at which the confined-to-propagating transition is observed. This gives us $\lambda \simeq 4.5 \text{ \AA}$, $\lambda \simeq 10 \text{ \AA}$, and $\lambda \simeq 40 \text{ \AA}$ when $x=1$, $x=0.4$ and $x=0.3$, respectively. To our knowledge these are the first direct experimental estimates reported for the GaAs LO phonon penetration depth λ into the barriers of GaAs/ $\text{Al}_x\text{Ga}_{1-x}\text{As}$ superlattices and QW's. Our result for λ on the $x=1$ series is in good agreement with the theoretically known value of about 1 ML ($=2.83 \text{ \AA}$) [4,60,62]. The slightly larger value measured can be attributed to interface imperfection which is common in SL's thus making our measured value an upper estimate for λ . However, for the $x=0.4$ and $x=0.3$ series no such theoretical work is available, probably due to the complex nature of the alloy barrier. Kobayashi and Roy have predicted the existence of bulk-like propagating LO phonons using a force constant calculation on a sample with $L_z=42 \text{ \AA}$, $L_b=8 \text{ \AA}$, and $x=0.3$ [9]. This is consistent with our experimental results. On the other hand, for the series of samples with $x=0.2$, a penetration depth of 100 \AA was taken as a lower limit since the confined-to-propagating LO phonon transition was not observed up to barrier widths as large as 180 \AA .

In Figure 25 we plot the measured (circles) LO phonon penetration depth λ as a function of x for the series of samples with $L_z = 100 \text{ \AA}$. The striking new result is the unexpected sharp increase in λ as x decreased below $x=0.4$. This is clearly shown in this figure. The penetration depth for $x=0.4$ or $x=1$ is very small

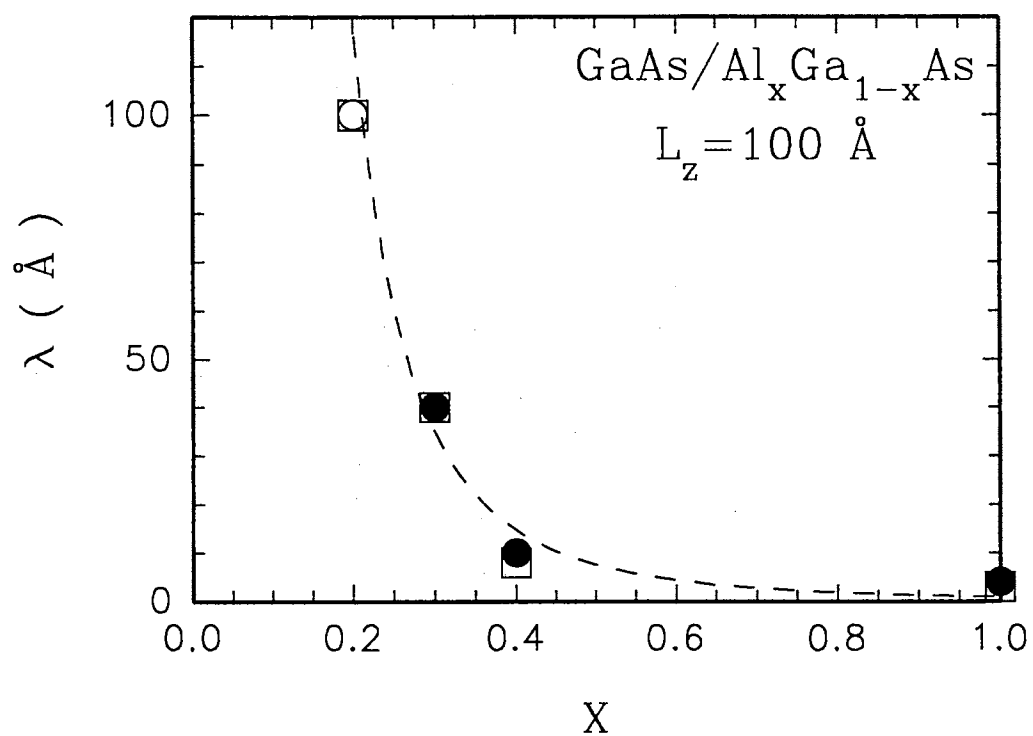


Figure 25. A plot of the GaAs LO phonon penetration depth λ into the $\text{Al}_x\text{Ga}_{1-x}\text{As}$ barriers as a function of x . The circles and squares are, respectively, the measured and calculated values. The curve is a fit to the data as discussed in the text

and sharply increases to 40 Å for $x=0.3$. Between $x=0.4$ and $x=0.3$ x changes only by 0.1 but the penetration depth increases by a factor of 4 from 10 Å to 40 Å.

Discussion and Conclusions

The rapid increase in the penetration depth with decreasing x is not expected if one uses an approach such as the Lyddane-Sachs-Teller (LST) relationship, concerning the macroscopic dielectric constant, in obtaining the spatial characteristics of LO phonons in SL's (i.e. dielectric continuum model) [5]. Essentially any small gap between the dispersions of GaAs and $\text{Al}_x\text{Ga}_{1-x}\text{As}$ optical phonons will result in confinement of the GaAs and AlAs-like modes in this type of approach. The GaAs-like LO phonons in the barriers, possessing slightly lower frequencies, have a chance of propagating via higher q modes of the GaAs well. Our results show significant penetration of the GaAs LO phonons into the barriers (40 Å) when $x=0.3$ where the frequency separation between the GaAs and GaAs-like modes is about 10 cm^{-1} . The macroscopic approach is certainly not suitable in dealing with spatial characteristics of LO phonons since the in-plane correlation length is of the order of 100 Å ($=1/q$, where q is the uncertainty of the in-plane wave vector). This is due to the fact that for the macroscopic approach to be valid, the in-plane correlation length has to be much larger than the well width.

To obtain valid spatial characteristics one has to perform a microscopic lattice dynamic calculation including the finite phonon lifetime and the interface roughness. We can then expect to obtain a strong penetration of the GaAs LO phonons into the alloy barriers roughly on the order of $\frac{a}{x^n}$, where a is the lattice constant and n is the number of Al atoms required to stop the GaAs modes from propagating. We note the good fit obtained with $\lambda(x) \sim \frac{1}{6} \cdot \frac{a}{x^3}$ as shown by the dashed line in Figure 25. Furthermore, since this is essentially a three dimensional problem, one way of looking at it might be from a purely statistical point of view. A percolation type of analysis may be a good approach since extremely sharp changes in penetration with composition are commonly observed in several

disordered systems [82]. A similar analysis is potentially suitable to predict the sharp increase in the LO phonon penetration we observe for $x < 0.4$.

At this point we would like to come back to the Fourier analysis used in the previous chapter to fit our hot phonon generation rates for $x=0.4$ and $x=1$. We have tried to fit our dN_q/dt data for $x < 0.3$ with Equation 44 of Chapter V with λ as an adjustable parameter. The result is excellent as shown in Figure 24. The best fit to the data is obtained for $\lambda \simeq 100 \text{ \AA}$. This is in good agreement with our estimated lower limit value for λ on the order of 100 \AA . It is important to note that the fit is not very sensitive to small changes in λ which is consistent with the similar values measured for dN_q/dt in all the samples with $x < 0.3$. This is easily understood since already at $x=0.2$ the GaAs and GaAs-like LO phonons of the wells and barriers, respectively, have so much energy overlap and hardly experience any phonon barriers (see Figure 22).

For the series with $x=0.3$, we were again able to obtain an excellent fit to the dN_q/dt data by using Equation 44 of Chapter V. The fit is shown by the solid curve in Figure 23. In this case the best fit is obtained for $\lambda = 40 \text{ \AA}$. Comparing the fitting values of λ to our measured values we obtained an excellent agreement between theory and experiment for all our x values. This is rather surprising considering the simplicity of the theory and the range of values of x and L_b considered. The theoretical values of λ are shown by open squares in Figure 25. We believe that at the intermediate values of x between 0.2 and 0.4 the LO phonons are possibly in a mixed state between confined ($x \geq 0.4$) and propagating ($x \leq 0.2$). The exact functional form of the phonon generation rate is more complicated especially in the intermediate values of x and could be affected by several factors which are not included in our simplified analysis. Some of these factors could include the change in the electronic band structure with x and the interface properties of the samples. The complexity of the alloy barriers involved in these systems in addition to the presence of energy subbands have challenged many theoretical physicists. This is apparent from the very slim literature available on this subject. Recently, there was an attempt by Colombo et al. to address the results

of our previous letter [14,83]. Their calculations on lattice dynamics and Raman backscattering intensities are in excellent agreements with our previous letter as well as our recent results [14,80,81]. Some other theoretical work in this area is being carried out by several groups [84,67]. More detailed theoretical studies on the phonon properties in and near the alloy barriers including the interface and bulk phonons are much needed for a complete understanding of the LO phonons and the extent of their penetration into the barriers.

Our results have immediate consequences on the problem of electron-LO phonon interaction in these GaAs/Al_xGa_{1-x}As nanostructures. This interaction is very important for ultrafast device applications and has been under a lot of investigations. Previously, it was believed that the 2-D nature of the optical phonons could significantly modify the electron-LO phonon scattering rates [5]. Recently, the more conclusive microscopic calculation by Rucker et al. (discussed in Chapter IV) showed that the total electron-LO phonon scattering rates (including GaAs and AlAs interface phonons) is essentially the same as that of bulk GaAs for GaAs/AlAs QW's with L_z=100 Å. This is consistent with our results when considering the contribution of the "confined" GaAs LO phonons probed in our experiment. Furthermore, our results show that the electron-LO phonon scattering rates for these "confined" GaAs modes are essentially the same as that of bulk GaAs phonons for x<0.3 regardless of the barrier thickness considered. This result comes directly from our experimentally measured bulklike phonon generation rates for x<0.3 as shown in Figure 24.

In conclusion, we have shown that GaAs LO phonons in GaAs/Al_xGa_{1-x}As MQW's demonstrate bulklike properties for aluminum concentrations less than 0.3. Using the time resolved Raman scattering technique discussed in Chapter III, we have determined the penetration depth of GaAs LO phonons into the Al_xGa_{1-x}As alloy barriers. By investigating several series of samples we have found a strong dependence of λ on x. We have discussed important implications of this finding on electron-LO phonon scattering rates in these MQW or SL structures. In particular, we have shown that the electron-LO phonon scattering rates for the GaAs

"confined" phonons are practically the same as that of bulk GaAs phonons when the alloy composition is lower than 0.3 regardless of the barrier width considered. Good agreement was obtained between measured λ 's and those obtained from our simple Fourier analysis discussed in Chapter V. Furthermore, we have proposed a purely statistical approach (percolation) to this complicated problem. Since many GaAs/ $\text{Al}_x\text{Ga}_{1-x}\text{As}$ MQW's or SL's are grown with x near 0.3, this work will prove useful to both physicists and device engineers.

CHAPTER VII

QUANTUM BEATS AND EXCITON DEPHASING MEASUREMENTS

Introduction

Many-body interactions in solids are of fundamental general interest. In semiconductor materials, these interactions are coulombic in nature and involve the scattering of excitons with free carriers, other excitons, and lattice vibrations or phonons. It was not until recently that experiments could be designed to study such interactions due to their extremely short time scale (on the order of few tens of femtoseconds) [16,86]. One of the most commonly used techniques is the so-called two-pulse self-diffracted degenerate four wave mixing (DFWM). A brief discussion of this technique is given in Chapter III. This technique is very well suited for the study of ultrafast carrier dynamics in semiconductors. The time resolution of this technique is only limited by the laser pulse width.

Using this technique, Schultheis et al. have investigated the dephasing of excitons and free carriers for III-V bulk and QW compounds [87–92]. Exciton-exciton interactions and the HH-LH beating have been reported first by Göbel et al. [93]. In addition, the recent experiments of Kim et al. have shown extreme details of the time evolution of the exciton-exciton and exciton-free-carrier interactions in several GaAs/Al_xGa_{1-x}As QW samples [94–96]. Up to date no results have been reported on the superlattice (SL) case where L_b is about 50 Å or less. In the SL case the electrons are no longer confined to the GaAs wells instead they have wave functions that extend well into the barriers. This allows for the coupling of electrons in the adjacent wells and the formation of minibands. The complex nature of these effects have deterred both experimentalists and theorists from the study of these structures.

In this chapter we will present our DFWM results on a GaAs/Al_xGa_{1-x}As SL sample with $L_b = 50 \text{ \AA}$. The results from several different experimental conditions will be presented. Some of the possible many-body interactions responsible for our observed signal lineshapes will be discussed in reference to the recent QW results. We will also show the new and exciting results obtained from an MBE grown ZnSe layer on a bulk GaAs substrate. The results from the two samples are then compared and some important conclusions are drawn.

Experimental Results and Discussion

The sample we use for this study is the GaAs/Al_{0.3}Ga_{0.7}As SL with $L_b = 50 \text{ \AA}$ shown in Table I. The GaAs substrate was removed from this sample following the procedure outlined in Appendix A. In Figure 26 we show the photoluminescence excitation data (PLE) of this sample taken at 10 K [74]. The figure shows the energy positions of the HH and LH excitons at 1.5549 eV and 1.5696 eV respectively. The HH energy position corresponds to a wavelength of about 797.2 nm. The figure also shows the spectrum of our laser pulses at the excitation wavelength of 798 nm. Notice in particular the broad spectrum of these femtosecond pulses.

In Figure 27 we show the measured DFWM diffracted signal from this sample as a function of time delay between the pump and probe pulses. The sample is maintained at a temperature of about 10 K. The excited carrier density is intentionally made low and is estimated to be about 10^9 cm^{-2} . The wavelength of the pump and probe pulses is set to 798 nm which is in resonance with the HH exciton of this sample. The laser pulse autocorrelation is also shown in this Figure for comparison. The first thing we notice in this figure is the slow rise of the signal at negative time delay. This is much slower than the rise of the laser pulse indicating that there is some signal which is detected by the probe pulse at short times before the arrival of the pump pulse. In principle this negative time delay signal is not predicted if one uses the simple theory involving a noninteracting two-level system. On the other hand, one observes a decrease in the diffracted signal at positive time delays. This is consistent with the prediction of the simple

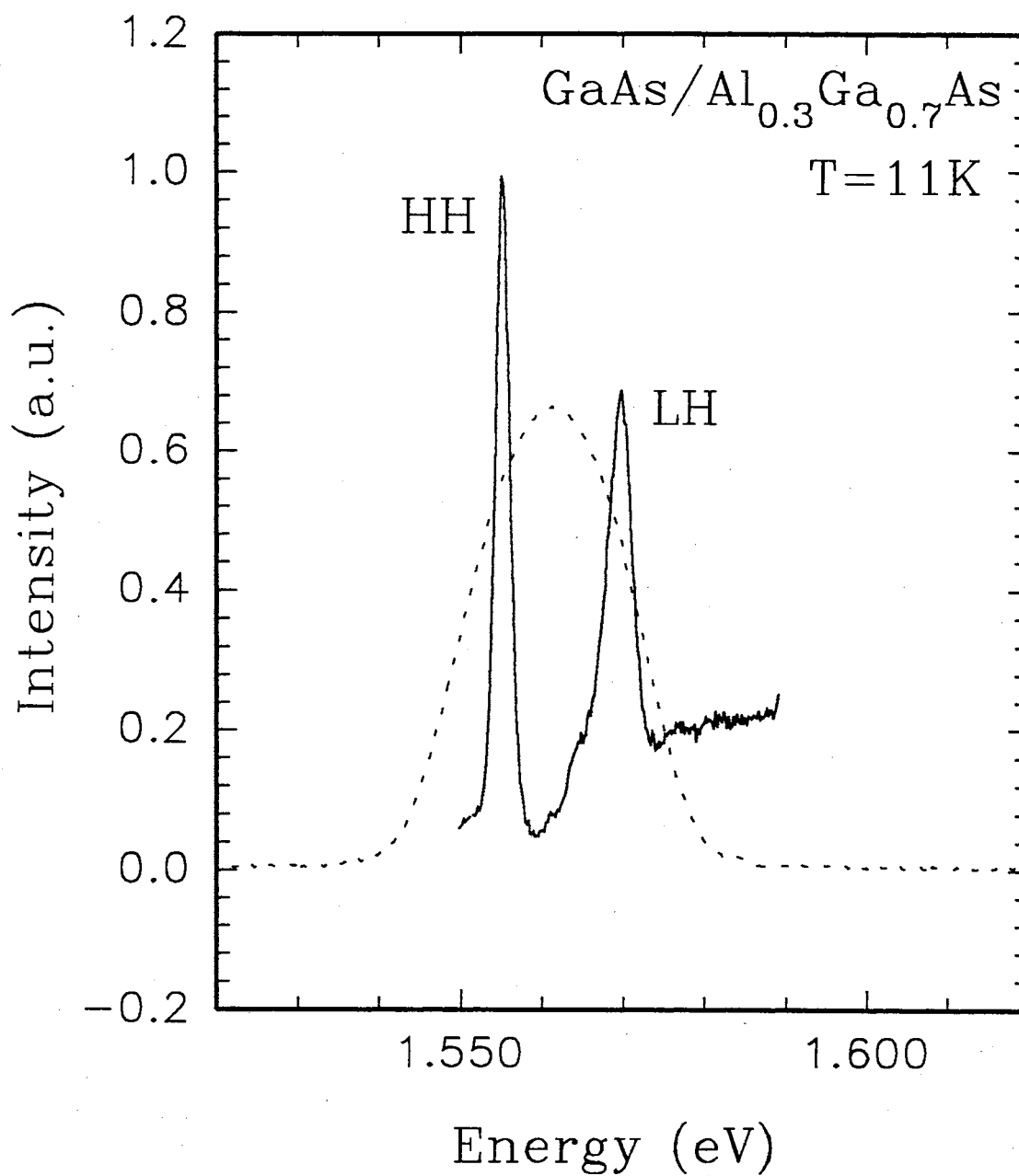


Figure 26. Photoluminescence excitation (PLE) of our GaAs/Al_{0.3}Ga_{0.7}As sample. Shown also is the spectrum of our femtosecond laser pulses (dashed curve)

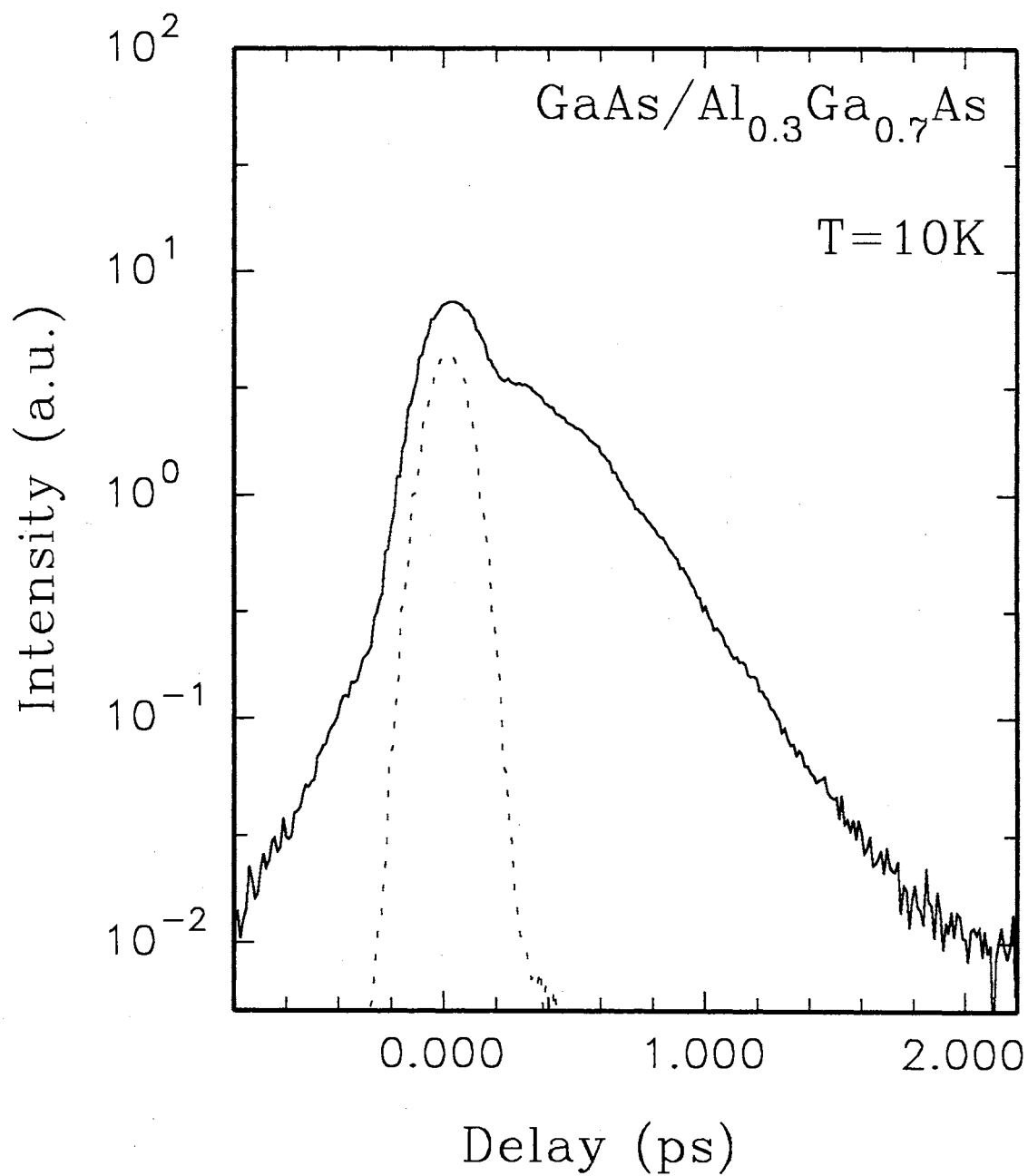


Figure 27. DFWM signal as a function of the time delay between the pump and probe pulses. The dashed curve is the autocorrelation trace of our laser pulses at 798 nm

noninteracting two-level model. This reduction in signal essentially reflects the decay of the polarization created by the pump pulse. The signal is expected to be strong at small positive time delays since the polarization created by the pump pulse is preserved when the probe pulse arrives. However, at large time delays the signal is expected to be very small since the polarization would have already decayed before the arrival of the probe pulse. This of course is dependent on the decay constant of this polarization which varies with several parameters such as the lattice temperature and the excited carrier density. This decay constant of the diffracted signal is related to the exciton dephasing time. Depending on whether the electronic transition is homogeneously or inhomogeneously broadened we can extract two different dephasing times from our data.

Yajima and Taira have performed theoretical calculations on the DFWM diffracted signal [97]. They used the noninteracting two-level system to study the temporal lineshape of the signal assuming δ -function excitation pulses. For the homogeneous transition one obtains

$$I(t) \simeq \begin{cases} 0, & t < 0 \\ \exp\left(\frac{-2t}{T_2}\right), & t > 0 \end{cases} \quad (45)$$

Where T_2 is the dephasing time which can be obtained from the data by an exponential fit using Equation 45. For an inhomogeneously broadened transition, things are more complicated due to the rapid decay of the polarization caused by the destructive interference characteristic of an inhomogeneous system. Hence, the decay time constant is expected to be much shorter than for the homogeneous case. In fact it is exactly reduced by a factor of two. In this case, the expression for the diffracted signal intensity as shown by Yajima and Taira is [97]

$$I(t) \simeq \begin{cases} 0, & t < 0 \\ \exp\left(\frac{-4t}{T_2}\right), & t > 0 \end{cases} \quad (46)$$

It is important to note that this model does not predict any signal at negative time delays in both cases. Even if the excitation pulses are given a finite duration, the signal at negative time delays will still only follow the rise time of these pulses.

Recently, it was pointed out by Stafford et al. that a detailed microscopic description of excitonic interactions is necessary to take into account the many-body interactions involved [98]. This has led to a more complicated temporal lineshape and the prediction of the signal at negative time delays. It was essentially shown that excitons not only interact with the electric field of the excitation pulses but also with the polarization of other excitations such as excitons. The diffracted signal lineshape calculated by Stafford et al. [98] for a homogeneously broadened transition is as follows:

$$I(t) \simeq \begin{cases} \exp\left(\frac{4t}{T_2}\right), & t < 0 \\ \exp\left(\frac{-2t}{T_2}\right), & t > 0 \end{cases} \quad (47)$$

This theory also predicts no signal at negative time delays for an inhomogeneously broadened system. This is because the macroscopic polarization due to the e-h pair interactions decays much faster in this system.

The sample quality is a major factor determining whether the transition is predominantly homogeneous or inhomogeneous. For very high quality QW samples it is expected to see very long dephasing times of the excitons on the order of picoseconds [87–92]. However, for poor quality samples several scattering mechanisms contribute to shortening the dephasing time. Among such mechanisms is impurity scattering due to rough QW interfaces.

In Figure 27 we can clearly see a signal from our sample at negative time delay. This indicates that our sample is of rather high quality and mostly homogeneously broadened. Our PLE data gives a HH peak linewidth of about 2 meV which is an indication of the good quality of our sample. An exponential fit to the data similar to Equation 47 leads to a time constant of 214 fs at long positive time delays and two different rise times of 147 fs and 55 fs at negative time delays. The 214 fs decay constant corresponds to a phase relaxation T_2 between 0.428 ps and 0.856 ps for predominantly homogeneously and inhomogeneously broadened transition respectively. In a DFWM experiment, one cannot discriminate between homogeneous and inhomogeneous broadening. However, a comparison of the rate

$2/T_2$ with the PLE linewidth indicates that it is possible that the transition is mostly inhomogeneously broadened. There is also another longer time constant that is restricted to short positive time delays (~ 0.5 ps). This time constant is about 464 fs leading to a phase relaxation between 0.928 ps (for homogeneous broadening) and 1.856 ps (for inhomogeneous broadening). Comparing $2/T_2$ in this case to the PLE linewidth indicates that this transition is mainly homogeneously broadened. Thus, since both time constants are present in our signal decay but the short time constant is dominant, we conclude that inhomogeneous broadening is present in our sample.

Quantum Beats

Quantum beats is an important nonlinear spectroscopic technique that has been used in the study of atoms and molecules [99–101]. However, the first observation of quantum beats from extended electronic states in condensed media was reported independently just a couple of years ago by Göbel et al. [93] in a GaAs/ $\text{Al}_x\text{Ga}_{1-x}\text{As}$ QW structure and by Langer et al. [102] in AgBr₂. In both cases the beats are due to coherent interference between excitonic states that are split either by the QW structure of the sample or by an external magnetic field. For a simple system with two closely spaced energy levels the beating period is related to the energy splitting of the two levels in the following form [103,104]:

$$T = \frac{h}{\Delta E} \quad (48)$$

Where $\Delta E = E_2 - E_1$ is the energy difference between the two levels and h is Planck's constant.

Figure 28 shows our measured DFWM diffracted signal at the excitation wavelength of 794 nm which correspond to an energy of about 1.5611 eV. The laser spectral shape at this wavelength is shown in Figure 26 together with the HH and LH PLE spectrum. Notice that both the HH and LH excitons can be excited simultaneously at this wavelength due to the broad spectrum of the laser

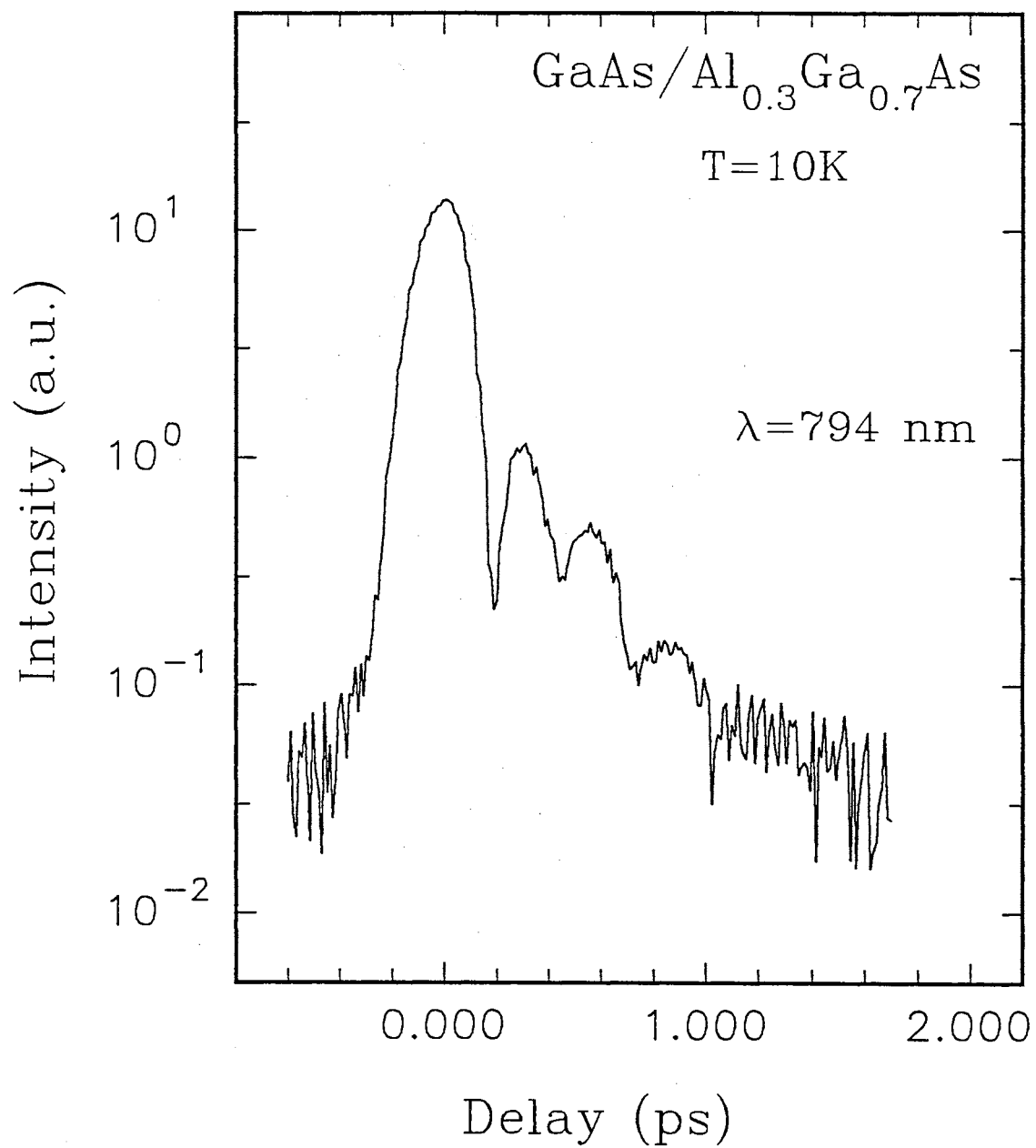


Figure 28. Diffracted signal showing quantum beats between HH and LH excitons

pulses. Thus, in this way we create a coherent superposition of these closely spaced states leading to destructive interference between them and the so-called quantum beats. These quantum beats are similar to those reported by Göbel et al. and Leo et al. [93,104]. Our results, however, show a much stronger interference between the HH and LH excitons. It is clear from Figure 28 that the signal intensity almost completely vanishes due to interference. To our knowledge, this is the first report of such strong interference between the HH and LH excitons. We interpret this result as due to the enhanced LH oscillator strength due to the superlattice structure of our sample. This is clearly observable from the LH peak intensity in the PLE data shown in Figure 26. It is well known that GaAs/Al_xGa_{1-x}As heterostructures undergo a transition from MQW to SL when the barrier thickness is decreased below about 70 Å [2,105]. In the SL case the electronic wave functions from adjacent wells overlap significantly. This overlap allows the electron to move freely from one well to the other. This is in contrast with the QW case where the electron is almost perfectly confined in the well and a well-to-well interaction is not possible.

Using Equation 48 we can estimate the energy separation between the HH and LH excitons. From Figure 28 we measure a beating period T of about 281 fs. Inserting this into Equation 48 and solving for ΔE we get :

$$\Delta E = \frac{h}{T} = 14.72 \text{ meV}$$

This is in excellent agreement with the PLE measurement that gives $\Delta E = 14.70$ meV as obtained from Figure 26. It is also important to note the inverse relationship existing between T and ΔE as shown in Equation 48. This implies that as ΔE becomes small and possibly difficult to measure with PLE experiments, T on the other hand becomes larger and clearly more visible in DFWM. Although the latter experiment is technically more involved, it can be an excellent tool to measure very small energy separations provided that the dephasing time of the elementary excitations is longer than the beating period.

Wavelength Dependent DFWM Lineshapes

Our wavelength dependent DFWM experiments on the GaAs/Al_{0.3}Ga_{0.7}As SL sample have lead us to some very interesting signal lineshapes. Figures 29 and 30 show, respectively, the logarithmic and linear plots of several diffracted signal intensities as a function of energy detuning from the HH resonance. The new and most exciting result found in this study is the appearance of a rather flat region at the top of our signal at small positive time delays. This region starts to emerge at very small energy detuning δ below the HH resonance. It becomes apparent for δ as low as -2 meV and gets larger with increased detuning below the HH resonance. It extends over a surprisingly long time of about 0.8 ps at $\delta = -16.7$ meV. One can estimate a time constant for this region to be on the order of 9 ps which is very large compared to the decay time measured after 1 ps time delay. The dephasing time corresponding to this time constant is ~ 18 ps for a homogeneously broadened transition and ~ 36 ps for an inhomogeneously broadened transition. This dephasing time is extremely long compared to all previously reported measurements in GaAs/Al_xGa_{1-x}As QW's. We attribute this long time constant to be possibly due to the long exciton coherence time expected as a result of their lowered occupancy. By detuning our laser below the HH resonance, we essentially excite fewer excitons and reduce the exciton-exciton scattering probability. The other time constant obtained after 1 ps time delay is slightly reduced at $\delta = -16.7$ meV compared to $\delta = 0$. This time constant measured is about 159 fs compared to 214 fs for $\delta = 0$.

The lineshape of the signal also shows an extremely sharp peak around $t=0$ that persists regardless of δ . The rise time of this peak is comparable to our laser pulses as can be seen in Figure 27. This is a rather important result that we believe is only possible in a superlattice case where carriers are not perfectly confined. Due to the relatively fast rise of this peak, we believe that its origin should be due to free carrier scattering which is an extremely fast process. The intensity of this peak becomes lower as the excitation energy is tuned further bellow

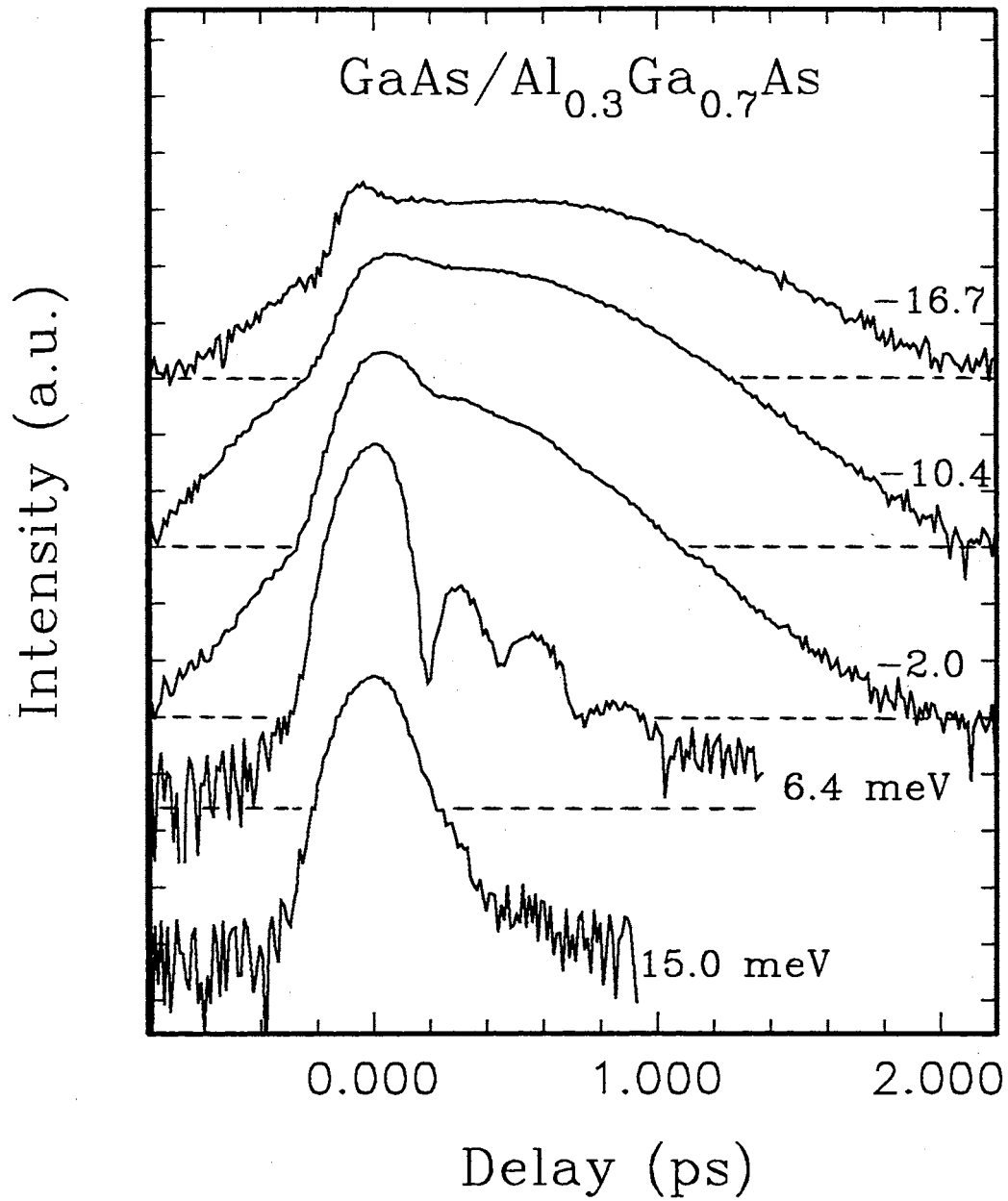


Figure 29. Log scale plot of the DFWM signal as a function of energy detuning from the HH resonance

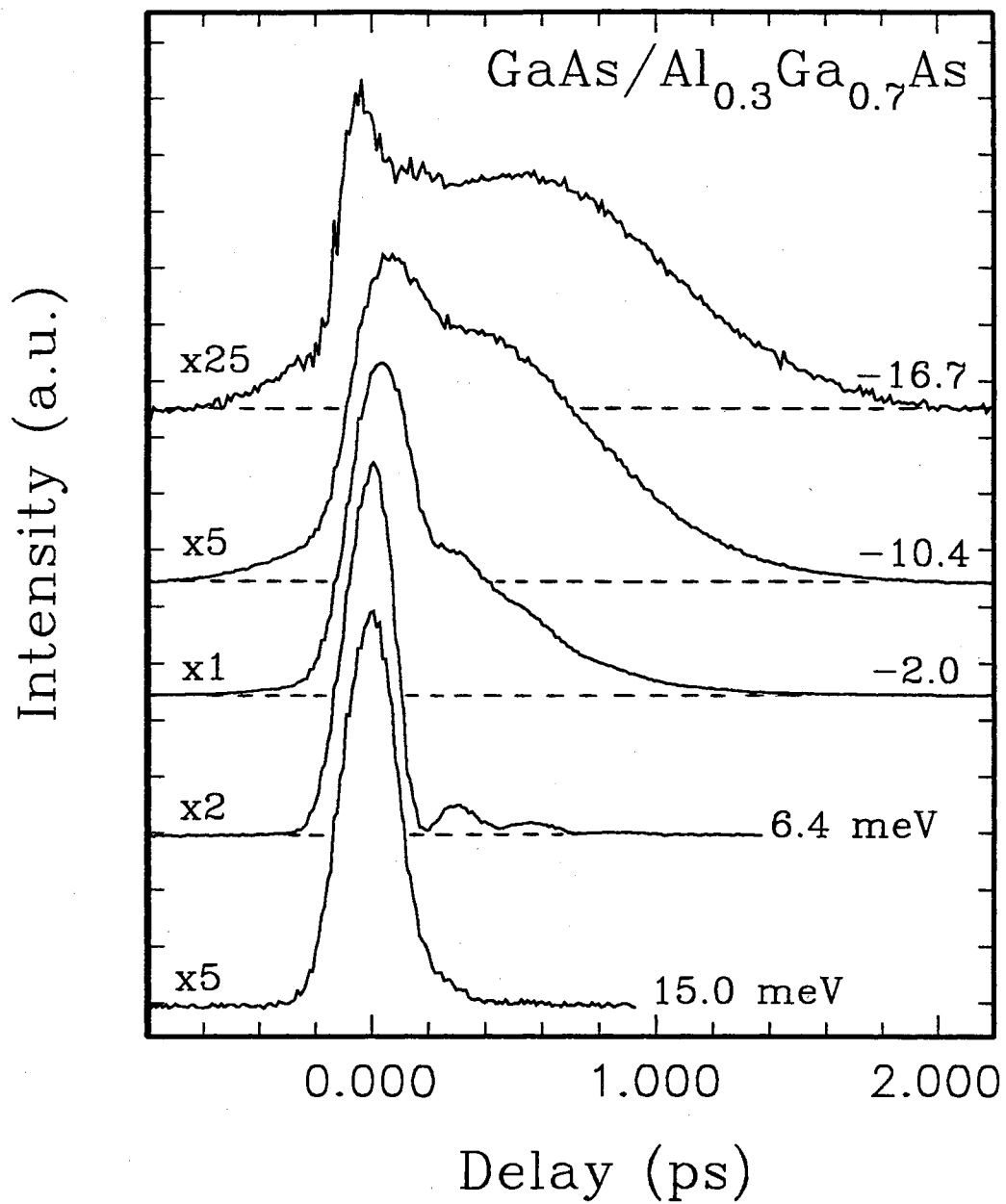


Figure 30. Linear plot of the DFWM signal as a function of energy detuning from the HH resonance

the GaAs gap (δ negative) as can be seen in Figure 30. This is consistent with the lower density of free carriers excited by these energies and further supports our interpretation. At longer times before the arrival of the pump pulse (i.e. negative delay), we observe a relatively slow rise of the signal on the order of 100 fs. The interpretation of the negative time delay signal is a complicated issue that is still controversial. In the literature, either a slow or a fast rise of the signal is reported and is interpreted by several authors as due to a coherent coulomb interaction of excitons in QW's [98,104]. This is consistent with our observations since the negative delay signal only appears when the exciton dephasing time is long (i.e. at negative δ). The value of this rise time in a homogeneously broadened system was recently shown to be about half the time constant for the decay of the signal in a QW sample [104]. In our case, however, we measure a ratio of about 1.5 at several negative detunings. We believe that the slightly lower value we measure could be attributed to the fact that our sample has some inhomogeneous broadening as discussed earlier. In addition, the microscopic theory used to derive the factor of 2 does not take into account SL effects such as minibands and the well-to-well coupling of the electronic wave functions. Furthermore, since we observe both a fast and slow rise of our signal is a good indication that both homogeneous and inhomogeneous broadening is present in our sample.

At excitation energies above the HH energy we observe drastic changes in the signal temporal lineshape. As can be seen in Figures 29 and 30 the signal decays much faster at these excitation energies. This has been observed previously in the QW case and is attributed to the increased exciton occupation number [95]. This leads to a reduction in the dephasing time due to efficient exciton-exciton collisions. This picture is further supported by the similar results obtained when the excited carrier density is increased by increasing the laser power. Our results for the SL case are consistent with the interpretations used in QW samples [104].

Power Dependence of DFWM Signal

Figures 31 and 32 show, respectively, the logarithmic and linear plot of the DFWM signal at several average pump and probe laser powers at the sample. P_0 is an average power of about 0.5 mW at the sample. At P_0 the carrier density excited is about $4 \times 10^8 \text{ cm}^{-2}$ (see Appendix B). These data are taken at 10 K with an excitation wavelength of 798 nm which is at the HH resonance. At low powers we observe similar signals as previously with long dephasing time and a negative delay signal associated with it. At excitation powers about 13 times larger than P_0 we observe a flattening of the peak around $t=0$. This is a rather new and interesting result that further supports our interpretation of this peak as due to carrier-carrier scattering. By increasing the laser power we are essentially pumping more and more carriers into the conduction band. After certain powers the excited carrier density is so large that we believe a plasma is created. In this case the carrier-carrier interaction is, perhaps, partially screened leading to the long decay constant observed (i.e. flat portion of the peak). This plasma is not going to be stable and will decay after a short time as observed. Note also that the rise and drop of this peak is very fast and comparable to our laser pulse rise time. It is also possible that higher order terms in the nonlinear polarization interfere with the third order term (or $\chi^{(3)}$). This has been observed recently by Leo et al. [106] in the form of a dip near $t=0$ in an InGaAs/InAlAs sample. In Figure 32 we can clearly observe a small dip near $t=0$. On the other hand we also observe an enhancement of the strength of the quantum beats between the HH and LH. The beat period has also shown no dependence on the laser power which is not surprising since it only depends on the HH-LH energy separation.

Temperature Dependence of DFWM Signal

In Figure 33 we show the DFWM signal at several lattice temperatures with the excitation pulses always tuned to the HH resonance. In this case we also observe a drastic reduction of the exciton dephasing time. This, however, has a completely

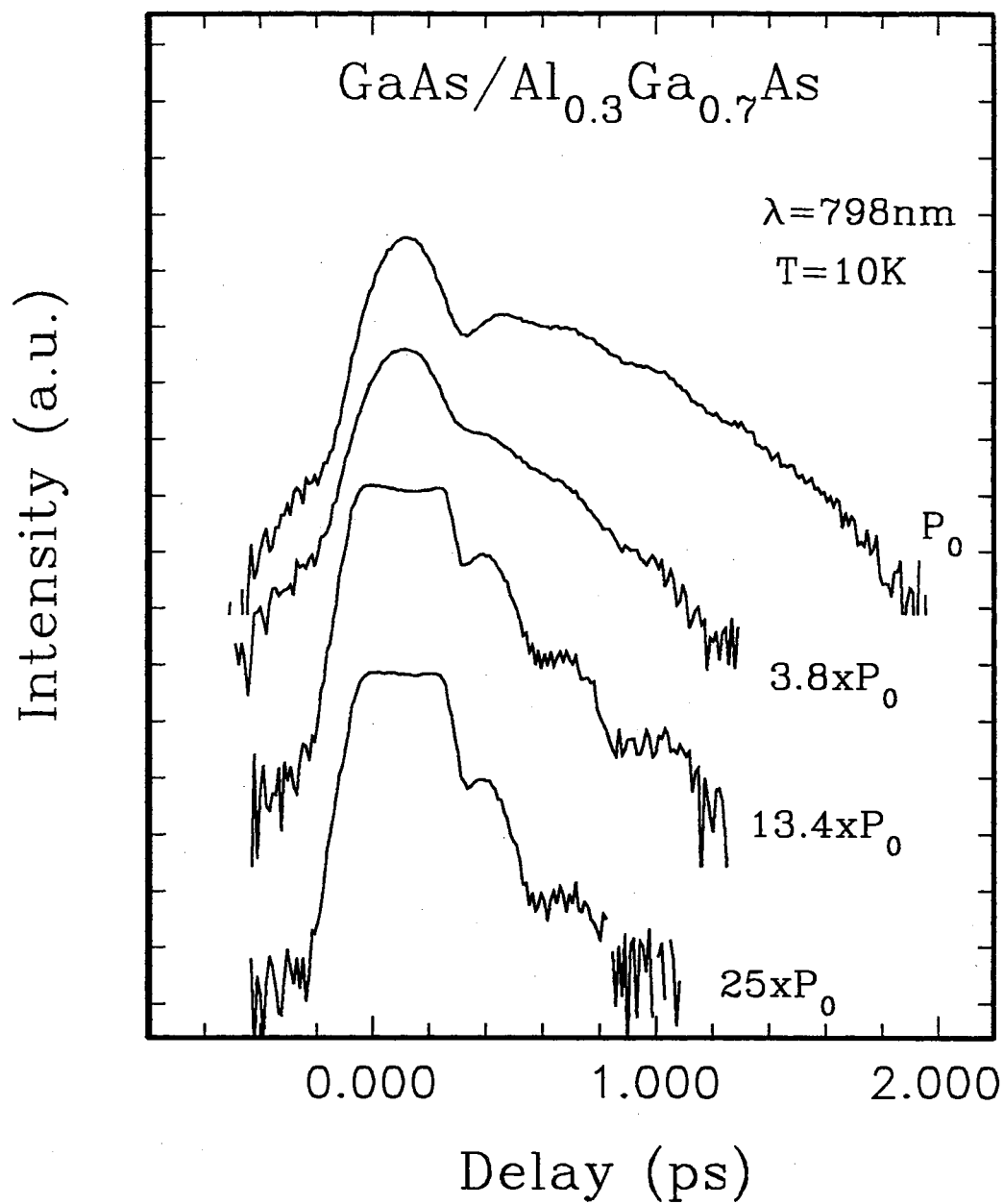


Figure 31. Log scale plot of the DFWM signal lineshape at several excitation powers ($P_0=0.5$ mW)

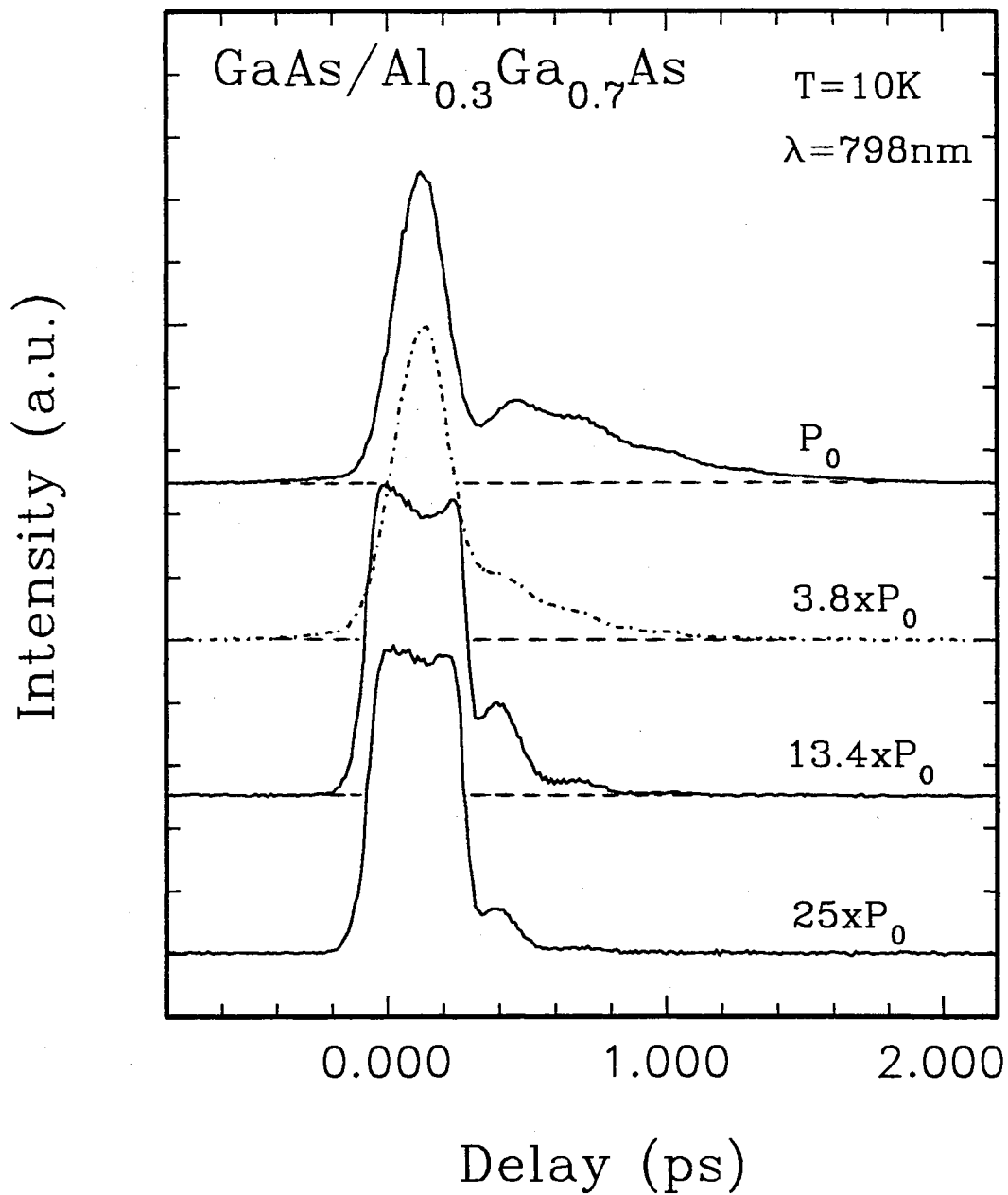


Figure 32. A linear plot of the DFWM signal as a function of the laser power ($P_0=0.5$ mW)

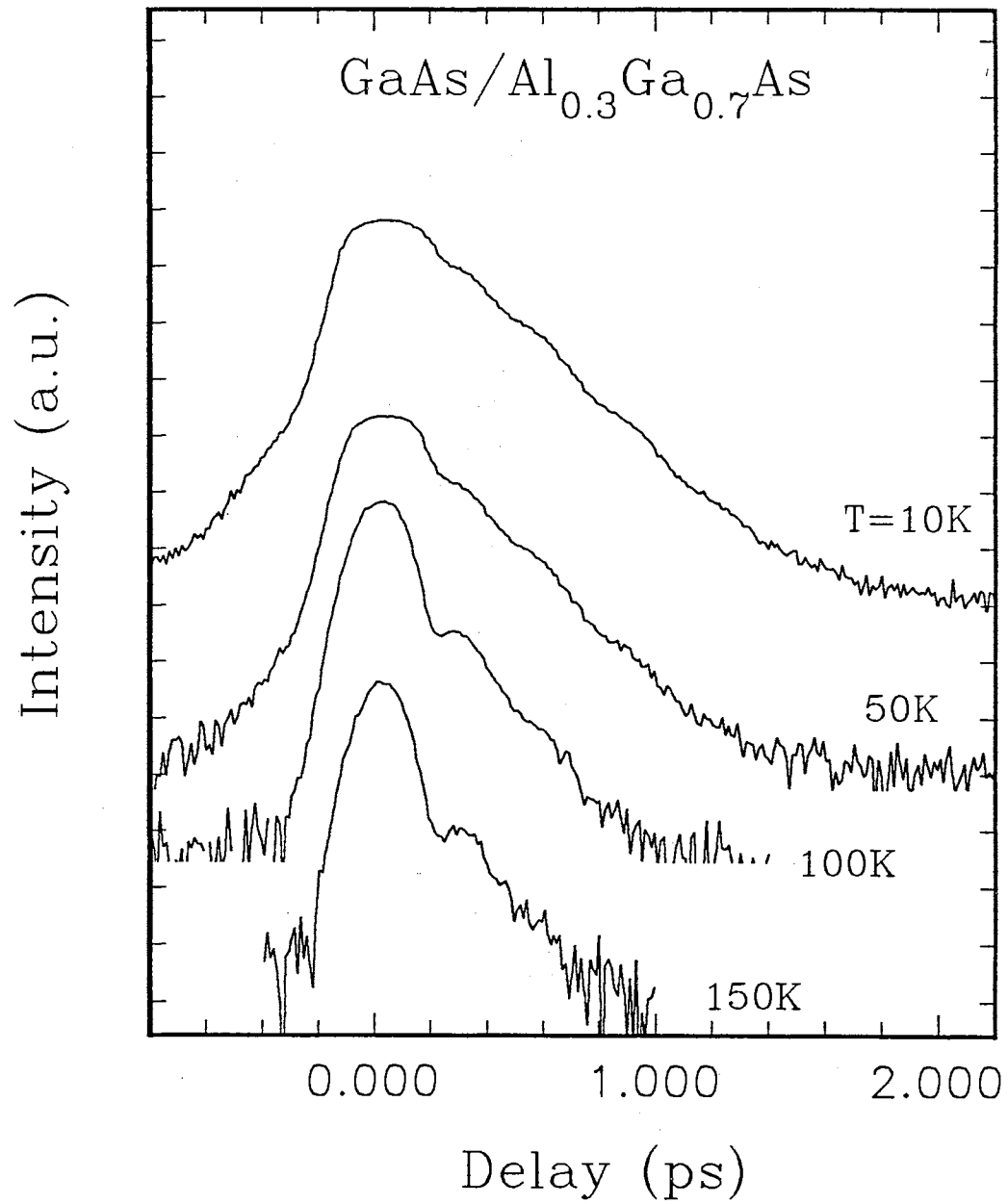


Figure 33. DFWM signal lineshape at different lattice temperatures in resonance with the HH exciton

different origin than the power or wavelength dependent spectra. In this case we are raising the temperature of the lattice which increases the thermal phonon population. It is this phonon population that ionizes the excitons and plays a major role in reducing the exciton dephasing time. In fact, at large enough temperatures the exciton binding energy (around 10 meV) [107] becomes comparable to kT leading to more exciton ionization and a large free carrier population. Again, carrier-carrier scattering becomes dominant and lead to the observed rapid decay of the signal at high temperatures. We have also checked the HH-LH beating period and it seemed unaffected by the lattice temperature variations to within our experimental uncertainty.

ZnSe Epilayer results

ZnSe and II-VI semiconductors in general have been the least studied by ultrafast laser spectroscopy. This is mainly due to their large energy gap requiring photon energies in the UV range. Just a couple of years ago it would have been almost impossible to obtain subpicosecond pulses with reasonable power tunable in the UV region. With the invention of femtosecond Ti:sapphire lasers this restriction can now be overcome with some efforts. As explained in Chapter III, these experiments require the doubling of our Ti:Sapphire frequency output in a nonlinear crystal. We are then able to tune our pump and probe wavelength to be resonant with an excitonic transition of our ZnSe sample. This sample is a 2 μm thick layer of ZnSe grown by MBE on GaAs substrate. The substrate is removed from a small area of the sample according to Appendix A to allow for these experiments. The procedure of the DFWM experiment is the same as described previously except for the added difficulties associated with the second harmonic generation and the wavelength tuning.

Figure 34 shows the photoluminescence (PL) data taken from our ZnSe sample with a HeCd laser at 10 K [108]. Shown also is the spectrum of our femtosecond excitation pulses at two different energies representing the upper and lower limits

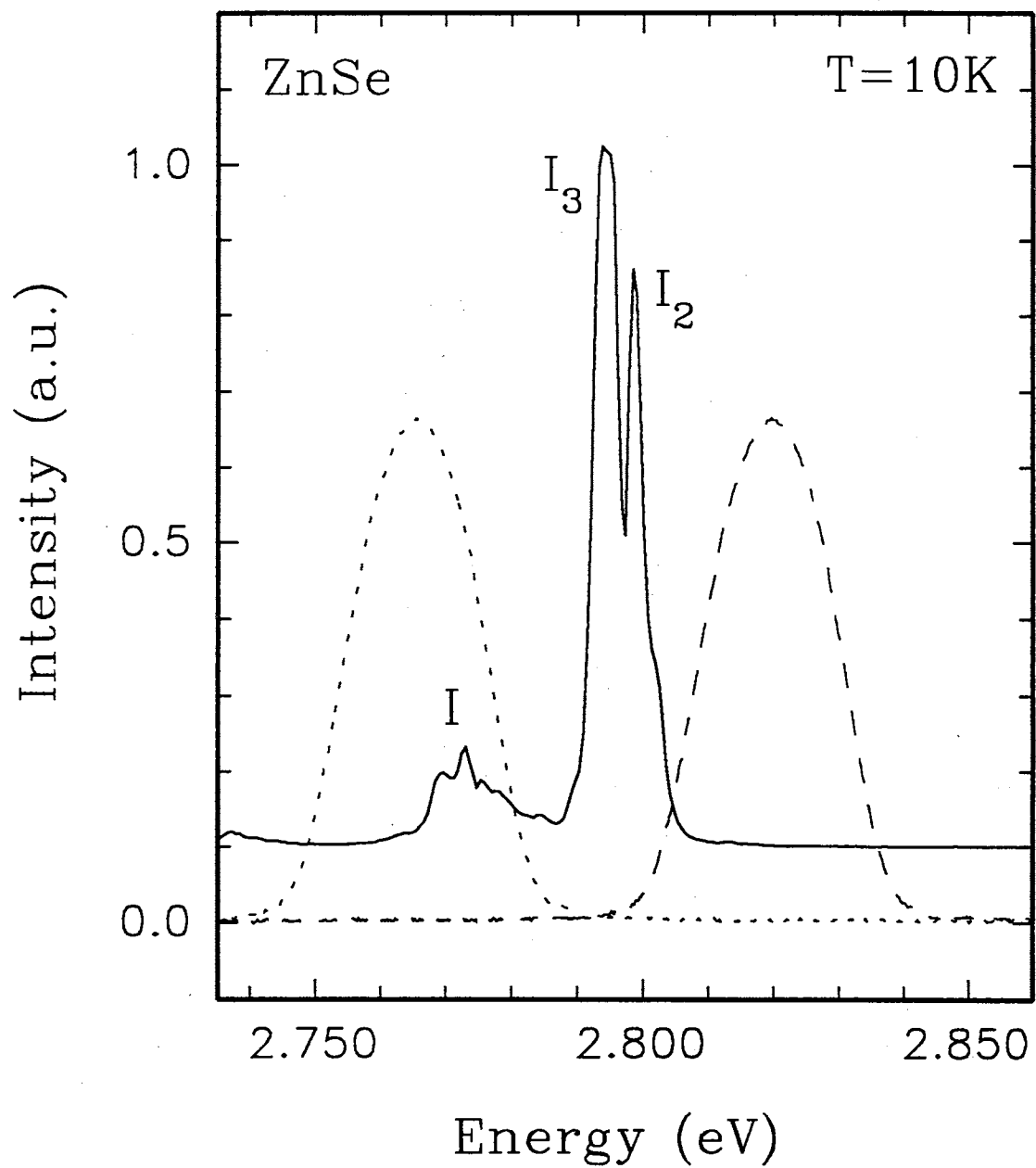


Figure 34. Photoluminescence data of the ZnSe epilayer sample obtained with a HeCd laser. Shown also is the spectrum of our femtosecond pulses at two different energies (dashed curves)

before the DFWM signal disappears. In this sample we can clearly see two excitonic peaks commonly labeled in the literature as I_2 and I_3 . These peaks are associated with a donor bound exciton (I_2) and a deep-donor bound exciton (I_3). The energy positions of these peaks are 2.798 eV and 2.794 eV respectively. The PL data also shows a third broad peak labeled I centered around 2.773 eV. This peak is much lower than the ZnSe band gap ($E_g = 2.80$ eV at 0 K) and is associated with impurity states.

A plot of a measured DFWM signal as a function of time delay from this sample is shown in Figure 35. This experiment was performed at a wavelength of 446.8 nm which is equivalent to an energy of about 2.774 eV. From a simple comparison to our previous results on GaAs/ Al_xGa_{1-x} As SL's we can immediately say that the exciton dephasing time in this sample is very short. It is important to note that these are the very first subpicosecond DFWM results reported on ZnSe epitaxial layers. The rise time and decay time of our signal are measured to be about 65 fs and 30 fs, respectively. This is rather surprising since one would expect the rise of the signal to be faster than its decay as is the case for GaAs/ Al_xGa_{1-x} As heterostructures. In fact, this is completely reversed in the ZnSe sample where we now observe a factor of two increase in the rise time relative to the decay time. Figure 35 also shows the autocorrelation of our fundamental frequency pulses. The second harmonic pulses are expected to be of the same width or narrower. Note especially that the decay of our signal is very fast and only limited by our laser pulse width. The rise time, however, is much larger than that of our laser pulses indicating that its origin is in the sample. It is not yet clear to us why the rise time is larger than the decay time and further experiments are needed to confirm this due to the very short time scale involved. However, we believe that the rapid decay of the signal observed in this sample could be attributed to the sample quality. It is well known that the growth of ZnSe on GaAs causes some induced strain in the ZnSe layer due to the relatively large lattice mismatch (on the order of 0.27 %) between the two materials. Strain is also caused by the different temperature expansion coefficients of the two materials.

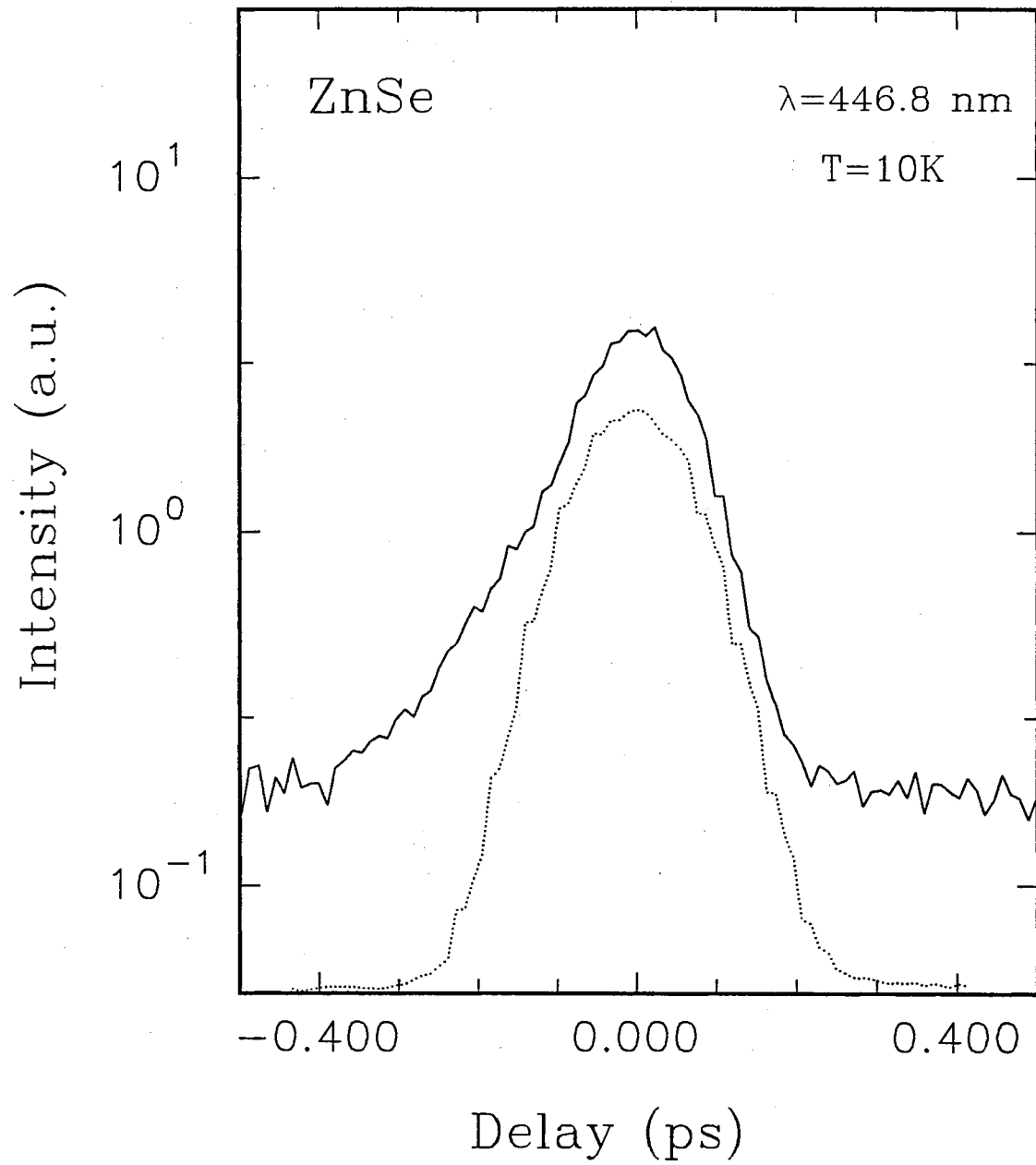


Figure 35. DFWM signal from a ZnSe epilayer sample

By removing the GaAs substrate some strain may be relieved but dislocations could also form in the sample. As clearly seen in the PL data some impurities are present in the sample even before removing the substrate. Both of these effects will contribute significantly to inhomogeneous broadening of the electronic transition in this sample. This interpretation is consistent with the fast signal decay observed in intentionally inhomogeneously broadened GaAs/Al_xGa_{1-x}As samples [104]. We believe that the transition in our sample is mostly inhomogeneously broadened. Another way to check inhomogeneous broadening is by time-resolving the diffracted signal and observing a photon echo pulse appearing at a time t after the probe pulse where t is exactly equal to the time delay between the pump and probe pulses.

Figure 36 shows a log scale plot of the DFWM signal lineshape as a function of energy detuning (δ) from the I₃ exciton resonance. Figure 37 shows the same line shapes in a linear scale. The energy separation between I₂ and I₃ is $\Delta E \simeq 4 \text{ meV}$ corresponding to a quantum beat period of about 1 ps. It is, therefore, impossible to see quantum beat between I₂ and I₃ bound excitons in this sample due to the very rapid signal decay. The most striking result of our data is the appearance of significant signal at negative time delays despite its fast decay. It is important to note that this is only observed for negative detuning δ . This is in contrast with our results and the results of others [106,104] on GaAs/Al_xGa_{1-x}As heterostructures where the negative delay signal was associated with the long exciton dephasing time. However, the fact that the negative delay signal rise time increases with increased detuning below the resonance is consistent with our observations in the GaAs/Al_{0.3}Ga_{0.7}As SL. We also observe a small decrease in the signal decay constant with increased detuning below the exciton resonance. This rapid decay of the signal can be explained by the possibility of exciting the carriers into the impurity states labeled I in the PL data of Figure 34. One would expect these states to have a faster decay time due to their low density of states. This picture is further supported by the result obtained at the largest detuning of our laser pulses ($\delta = -26.8 \text{ meV}$) where we are practically not exciting the states related to I₂ or

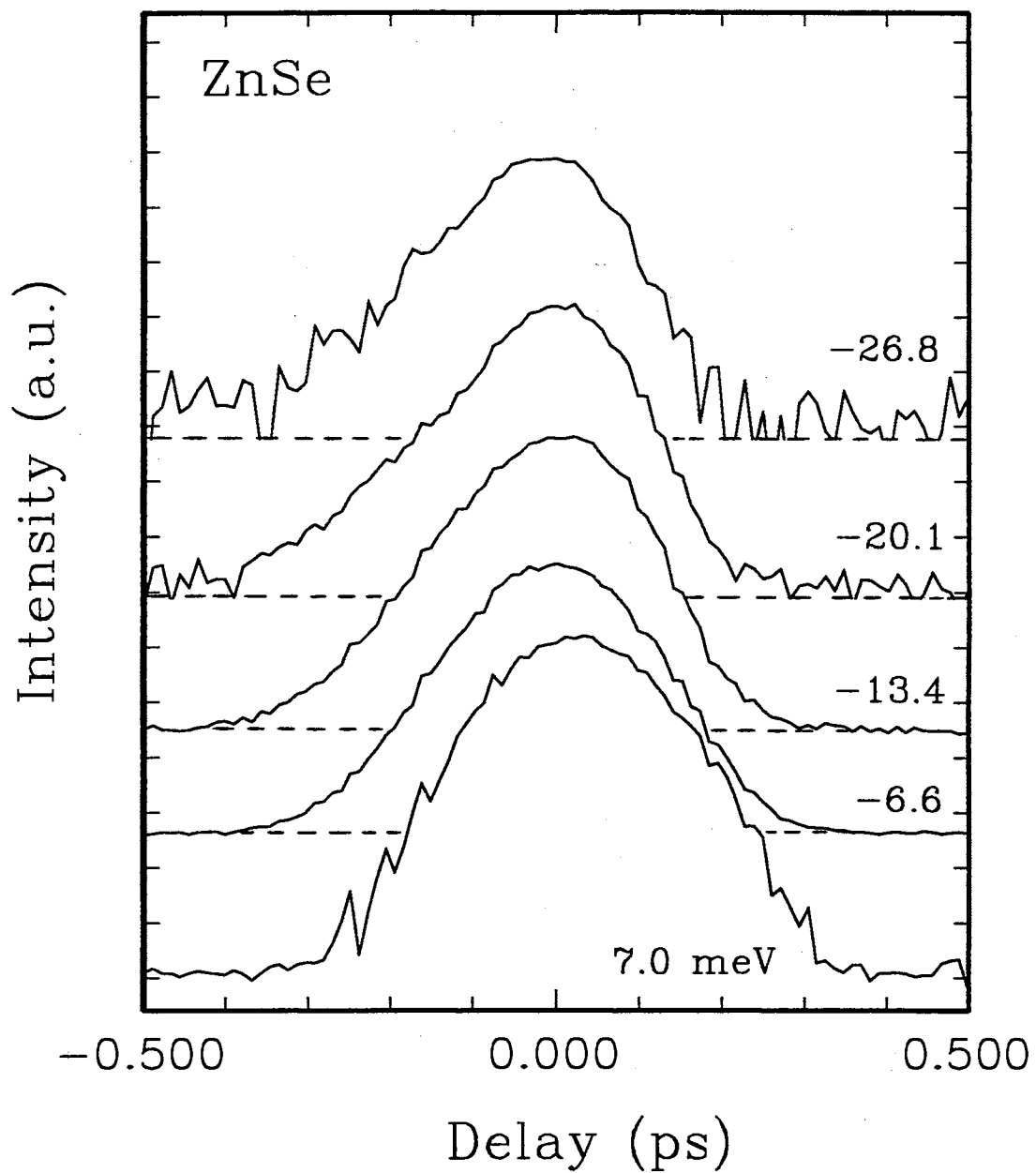


Figure 36. Log scale plot of the DFWM signal from the ZnSe sample as a function of laser detuning from the I_3 resonance

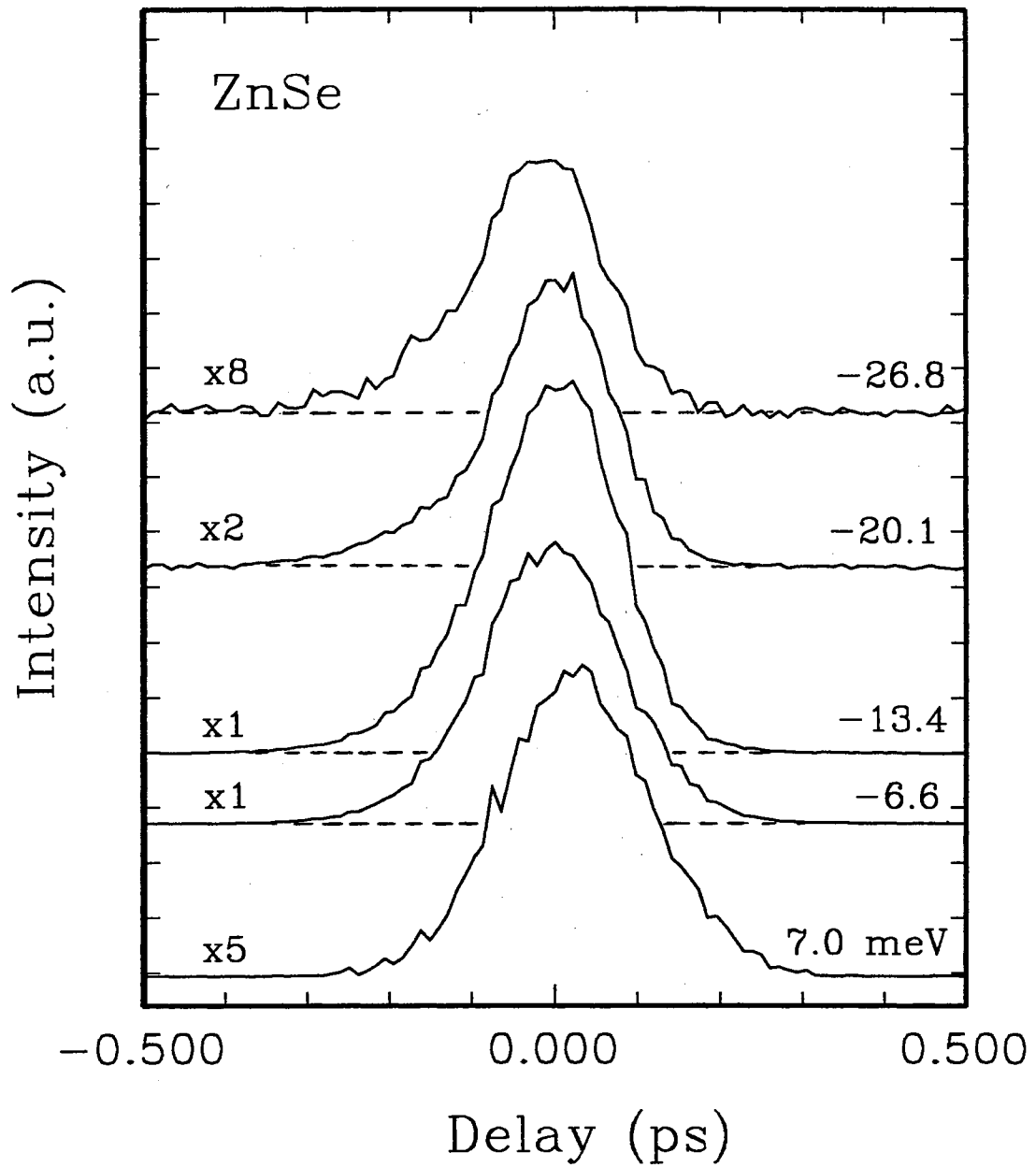


Figure 37. Linear scale plot of the DFWM signal from the ZnSe sample as a function of the laser detuning from the I_3 resonance

I₃. This is clearly shown by the dotted curve in Figure 34 where the excitation energy covers mainly the impurity peak labeled I.

Conclusions

In conclusion, we have performed subpicosecond DFWM experiments with near IR as well as UV laser pulses. The samples we studied are a GaAs/Al_{0.3}Ga_{0.7}As superlattice and a ZnSe epilayer. Both samples were grown on a GaAs substrate which we removed for the purpose of these experiments. We obtained very interesting results in both experiments. For the SL sample we observed the appearance of an extremely long time constant in the signal decay at negative detuning from the HH resonance. This time constant lasts up to about 0.8 ps at the largest energy detuning and is attributed to a possibly long exciton coherence as a result of their low occupation. The other most exciting result in this sample is the appearance of a 'plasma-like' response region around t=0 with a relatively long coherence time at high excitation densities. The temperature dependence and power dependence of the DFWM signal were also carried out and show similar behaviors which arise from different origins. We have also seen an enhancement of the quantum beat signal with increased excitation power.

Our measured negative time delay signal in the GaAs/Al_{0.3}Ga_{0.7}As SL sample was consistent with previous observations in similar QW samples but the signal from the ZnSe layer showed quite different results. The most important and new result found in this sample is the fact that the measured rise time of the signal is larger than its decay. We have suggested that this effect may be due to some contributions of impurity states in the sample present at the excitation wavelengths. The origin of the negative delay signal is still unclear and controversial. In our ZnSe sample we have shown that the recent interpretation of this signal does not apply at least to this sample. We believe that further studies are needed to resolve this issue. Furthermore, the signal decay time in the ZnSe sample was also observed to decrease with increased detuning below the exciton resonance. This is also in contrast with the results on GaAs/Al_xGa_{1-x}As SL's and QW's.

CHAPTER VIII

SUMMARY

We have conducted several picosecond and subpicosecond optical experiments on GaAs/Al_xGa_{1-x}As SL's and QW's in addition to a ZnSe epilayer. The QW samples are several series of MBE grown GaAs/Al_xGa_{1-x}As samples designed such that each series has a fixed x and well width L_z while the barrier width (L_b) varied. From series to series we only varied the aluminum concentration (x). We have performed picosecond Raman scattering experiments on all of these samples. Our most exciting results from these experiments can be summarized in three major findings. (1) The first observation of a confined-to-propagating GaAs LO phonon transition in GaAs/Al_xGa_{1-x}As SL's as L_b decreased. This was deduced from the observed sudden increase in the GaAs LO phonon generation rate to a bulk GaAs value with decreased L_b . We have interpreted this sudden increase in the hot phonon generation rate as due to a well-to-well coupling of the LO phonon wave functions in adjacent wells leading to bulklike extended phonon modes. This transition is rather sharp and extends over only ~ 5 Å for the two series of samples with $x=0.4$ and $x=1$. For $x=0.3$ we still observe the confined-to-propagating LO phonon transition but at a much larger barrier width which is consistent with the lowering of the "phonon-barrier" height by reducing x . (2) We reported the first estimates of the GaAs LO phonon penetration depth (λ) and observed a sharp increase in λ as x decreased. For instance λ changes from about 10 Å for $x=0.4$ to 40 Å for $x=0.3$. (3) Our results on the $x<0.3$ series have shown practically no LO phonon confinement up to barrier widths as large as 180 Å. This result implies that the electron-LO phonon scattering rates in these heterostructures are essentially the same as that of bulk GaAs for $x<0.3$. This is an important finding that will be beneficial in the device applications of these materials.

We have also performed subpicosecond DFWM experiments using near-IR pulses. This study included the temperature dependence, excitation energy dependence, and power dependence of the DFWM signal line shape as a function of time delay between the pump and probe pulses. The samples studied are a GaAs/Al_{0.3}Ga_{0.7}As SL with $L_b=50$ Å and a ZnSe thin layer sample grown on GaAs substrate. We have removed the GaAs substrate from both samples for the purpose of these experiments. Our major findings in this study can be summarized in four parts. (1) The observation of strong quantum beats between the HH and LH excitons in the SL sample. The increased strength of the beating was interpreted through the increased LH oscillator strength due to the SL structure. (2) We observed the appearance of long time constant at energy detunings below the HH resonance. This time constant was interpreted by the increased exciton dephasing time due to their reduced population at these energies. (3) The power dependent study has led us to some new and interesting results such as the enhancement of the HH-LH beating and the appearance of a dip and flat region around $t=0$ at high powers. We suggested the possible attribution of these results to a plasma-like formation and a higher order polarization effect. (4) In the ZnSe sample we obtained the very first subpicosecond DFWM results. Among these results are the surprisingly longer rise time compared to the decay time observed which is in contrast with the GaAs/Al_{0.3}Ga_{0.7}As SL results. The origin of the negative time delay signal is still controversial even in the well known structures of GaAs/Al_xGa_{1-x}As QW's. We have shown that the interpretation used previously to explain this signal in GaAs/Al_xGa_{1-x}As QW's does not apply, at least to our ZnSe sample. Further work is needed both in theory and experiment to help resolve this controversy.

BIBLIOGRAPHY

1. W.T. Tsang, in: *Semiconductors and Semimetals: Lighthwave Communications Technology*, ed. by W.T. Tsang, Vol. 22 part A, p. 95 (Academic, San Diego 1985).
2. C. Weisbuch in: *Semiconductors and Semimetals: Applications of Multi-quantum Wells, Selective Doping, and Superlattices*, ed. by R. Dingle (Academic, San Diego 1987), p. 1.
3. M. Jaros, *Physics and Applications of Semiconductor Microstructures* (Oxford, New York 1989).
4. B. Jusserand and M. Cardona : In *Light Scattering in Solids V*, ed. by M. Cardona, G. Güntherodt, Topics Appl. Phys., Vol. 66 (Springer, Berlin, Heidelberg 1989) p. 49 and references therein.
5. B.K. Ridley, in : *Hot Carriers in Semiconductor Nanostructures: Physics and Applications*, ed. J. Shah (Academic, San Diego 1992) p. 17 and references therein.
6. J.F. Ryan and M.C. Tatham, in : *Hot Carriers in Semiconductor Nanostructures: Physics and Applications*, ed. J. Shah (Academic, San Diego 1992), p. 345 and references therein.
7. J.A. Kash and J.C. Tsang, in : *Light Scattering in Solids VI*, eds. M. Cardona and G. Güntherodt, Topics Appl. Phys., Vol. 68 (Springer, Berlin, Heidelberg 1991), p. 423.
8. B. Jusserand, D. Paquet, and F. Mollot, Phys. Rev. Lett. **63**, 2397 (1989).
9. A. Kobayashi and A. Roy, Phys. Rev. B **35**, 2237 (1987).
10. D.J. Mowbray, M. Cardona, and K. Ploog, Phys. Rev. B **43**, 1598 (1991).
11. S. Baroni, P. Giannozzi, and E. Molinari, Phys. Rev. B **41**, 3870 (1990).
12. I. Brener, W.H. Knox, K.W. Goossen, and J.E. Cunningham, Phys. Rev. Lett. **70**, 319 (1993).
13. K.W. Goossen, J.E. Cunningham, M.D. Williams, F.G. Storz, and W.Y. Jan Phys. Rev. B **45**, 13773 (1992).

14. D.S. Kim, A. Bouchalkha, J.M. Jacob, J.F. Zhou, J.J. Song, and J.F. Klem, Phys. Rev. Lett. **68**, 1002 (1992).
15. S. Adachi, J. Appl. Phys. **58**, R1 (1985).
16. J.Y. Bigot, M.T. Portella, R.W. Schoenlein, I.E. Cunningham, and C.V. Shank, Phys. Rev. Lett. **65**, 3429, (1990).
17. J.D. Kafka, B.H. Kolner, T. Baer, and D.M. Bloom, Opt. Lett. **9**, 505 (1984).
18. R.L. Fork, B.I. Greene, C.V. Shank, Appl. Phys. Lett. **38**, 671 (1981).
19. J.A. Valdmanis and R.L. Fork, IEEE J. Quantum Electron. **QE-22**, 112 (1986).
20. E.P. Ippen and C.V. Shank, *Topics in Applied Physics*, Vol. 18, Chapter 3 (Springer-Verlag, New York 1977).
21. J.A. Kash, S.S. Jha, and J.C. Tsang, Phys. Rev. Lett. **58**, 1869 (1987).
22. J.A. Kash, J.M. Hvam, J.C. Tsang, and T.F. Kuech, Phys. Rev. B **38**, 5776 (1988).
23. K.T. Tsen and H. Morkoç, Phys. Rev. B **37**, 7137 (1988).
24. M.C. Tatham, J.F. Ryan, and C.T. Foxon, Phys. Rev. Lett. **63**, 1637 (1989).
25. J. Shah, B. Deveaud, T.C. Damen, W.T. Tsang, and P. Lugli, Phys. Rev. Lett. **59**, 2222 (1987).
26. C.L. Collins, Ph.D. thesis, University of California at Berkeley, 1984 (unpublished).
27. D.S. Kim, Ph.D. thesis, University of California at Berkeley, 1990 (unpublished).
28. D.S. Kim and P.Y. Yu, Appl. Phys. Lett. **56**, 2210 (1990).
29. W. Pötz and P. Kocevar in: *Hot Carriers in Semiconductor Nanostructures: Physics and Applications*, ed. J. Shah (Academic, San Diego 1992), p. 87 and references therein.
30. C.L. Collins and P.Y. Yu, Phys. Rev. B **30**, 4501 (1984).
31. E.M. Conwell, *High Field Transport in Semiconductors*, Solid State Physics: Advances in Research and Applications, ed. by F. Seitz (Academic, New York 1967) Suppl. 9.
32. P.G. Klemens, Phys. Rev. **148**, 845 (1966).

33. T. Elsaesser, J. Shah, L. Rota, and P. Lugli, *Phys. Rev. Lett.* **66**, 1757 (1991).
34. E.M. Conwell and M.O. Vassel, *Phys. Rev.* **166**, 3, 797 (1968).
35. J.N. Shulman and Y.C. Chang, *Phys. Rev. B* **31**, 2056 (1985).
36. J.F. Zhou, P.S. Jung, and J.J. Song, *Appl. Phys. Lett.* **56**, 1880 (1990).
37. R. Fuchs and K.L. Kliewer, *Phys. Rev.* **140**, A2076 (1965).
38. A.A. Lucas, E. Kartheuser, and R.G. Badro, *Phys. Rev. B* **2**, 2488 (1970).
39. F.A. Riddoch and B.K. Ridley, *J. Phys. C* **16**, 6971 (1983).
40. N. Mori and T. Ando, *Phys. Rev. B* **40**, 6175 (1989).
41. J.K. Jain and S. Das Sarma, *Phys. Rev. Lett.* **62**, 2305 (1989).
42. H. Rucker, E. Molinari, and P. Lugli, *Phys. Rev. B* **45**, 6747 (1992).
43. L. Wendler and R. Pechsted, *Phys. Status Solidi B* **141**, 129 (1987).
44. B.K. Ridley, *Phys. Rev. B* **39**, 5282 (1989).
45. K. Huang and B.F. Zhu, *Phys. Rev. B* **38**, 2183 (1988).
46. K. Huang and B. Zhu, *Phys. Rev. B* **38**, 13377 (1988).
47. G. Weber, *Phys. Rev. B* **46**, 16171 (1992).
48. H. Rucker, E. Molinari, and P. Lugli, *Phys. Rev. B* **44**, 3463 (1991).
49. A. Seilmeier, H.J. Hübner, G. Abstreiter, G. Weimann, and W. Schlapp, *Phys. Rev. Lett.* **59**, 1345 (1987).
50. M.C. Tatham, J.F. Ryan, and C.T. Foxon, *Solid-State Elect.* **32**, 1497 (1989).
51. U. Cebulla, A. Forchel, G. Bacher, D. Grützmacher, W.T. Tsang, and M. Razhegi, *Solid-State Elect.* **32**, 1669 (1989).
52. W. Pötz and P. Kocevar, *Phys. Rev. B* **28**, 7040 (1983).
53. K. Leo, W.W. Ruhle, and K. Ploog, *Phys. Rev. B* **38**, 1947 (1988).
54. K.T. Tsen and H. Morkoç, *Phys. Rev. B* **38**, 5615 (1988).
55. J. Shah, A. Pinczuk, A.C. Gossard, and W. Wiegmann, *Phys. Rev. Lett.* **54**, 2045 (1985).
56. J.L. Birman, M. Lax, and R. Loudon, *Phys. Rev.* **145**, 620 (1966).

57. N.F. Mott and E.A. Davis, *Electronic Processes in Non-Crystalline Materials*, 2nd ed. (Clarendon, Oxford, 1979).
58. A.K. Sood, J. Menéndez, M. Cardona, and K. Ploog, *Phys. Rev. Lett.* **54**, 2111 (1985)
59. B. Jusserand and D. Paquet, *Phys. Rev. Lett.* **56**, 1752 (1986).
60. B. Zhu and K.A. Chao, *Phys. Rev. B* **36**, 4906 (1987).
61. B. Jusserand and D. Paquet, *Phys. Rev. B* **30**, 6245 (1984).
62. T. Tsuchiya, H. Akera, and T. Ando, *Phys. Rev. B* **39**, 6025 (1989).
63. C. Colvard, T.A. Gant, M.V. Klein, R. Merlin, R. Fischer, H. Morkoç, and A.C. Gossard, *Phys. Rev. B* **31**, 2080 (1985).
64. A.K. Sood, J. Menéndez, M. Cardona, and K. Ploog, *Phys. Rev. Lett.* **54**, 2115 (1985).
65. D.Y. Oberli, D.R. Wake, M.V. Klein, J. Henderson, and H. Morkoç, *Phys. Rev. Lett.* **59**, 696 (1987).
66. D.S. Kim and P.Y. Yu in: *Proceedings of SPIE Symposium on Ultrafast Laser Probe Phenomena in Bulk and Microstructure Semiconductors*, ed. R.R. Alfano, Vol. 1282, p. 39 (SPIE, Bellingham 1990).
67. K.W. Kim, M.A. Stroscio, and J.C. Hall, *J. Appl. Phys.* **67**, 6179 (1990).
68. J.A. Kash, J.C. Tsang, and J.M. Hvam, *Phys. Rev. Lett.* **54**, 2151 (1985).
69. D.S. Kim and P.Y. Yu, *Phys. Rev. Lett.* **64**, 946 (1990).
70. A.K. Sood, J. Menendez, M. Cardona, K. Ploog, *Phys. Rev. Lett.* **56**, 1753 (1986).
71. D.S. Kim and P.Y. Yu, *Phys. Rev. B* **43**, 4158 (1991).
72. K.T. Tsen, K.R. Wald, T. Ruf, P.Y. Yu, and H. Morkoç, *Phys. Rev. Lett.* **67**, 2557 (1991).
73. Z.V. Popović, M. Cardona, E. Richter, D. Strauch, L. Tapfer, and K. Ploog, *Phys. Rev. B* **41**, 5904 (1990).
74. S.J. Hwang (private communication).
75. M.V. Klein, *IEEE J. Quantum Electron.*, **QE-22**, 1760 (1986).
76. B. Jusserand, F. Molloy, L.G. Quagliano, G. Le Roux, and R. Planel, *Phys. Rev. Lett.* **67**, 2803 (1991).

77. T. Kawamura and S. Das Sarma Phys. Rev. B **45**, 3612 (1992).
78. K.J. Nash and M.S. Skolnick, Phys. Rev. Lett. **60**, 863 (1988).
79. D.S. Kim, J.M. Jacob, J.F. Zhou, J.J. Song, C.W. Tu, H. Hou, and H. Morkoç, Phys. Rev. B **45**, 13973 (1992).
80. A. Bouchalkha, D.S. Kim, J.J. Song, and J.F. Klem in: *Proceedings of SPIE Symposium on Quantum Well and Superlattice Physics IV*, Eds. G.H. Dohler and E.S. Koteles, Vol. 1675 (SPIE, Bellingham 1992), p. 74.
81. A. Bouchalkha, D.S. Kim, J.M. Jacob, J.J. Song, and J.F. Klem, Phys. Rev. B (submitted).
82. B. Shapiro, in : *Percolation Structures and Processes*, ed. G. Deutscher, R. Zallen, and J. Adler (Adam Hilger, Bristol 1983), p. 367.
83. L. Colombo, C. Molteni, and L. Miglio, to appear in: *Proceedings of the 21th International Conference on the Physics of Semiconductors* (Beijing, August 10-14, 1992).
84. Y.C. Chang (private communication).
85. T.L. Reinecke (private communication).
86. S.M. Goodnick and P. Lugli, Phys. Rev. B **37**, 2578 (1988).
87. L. Schultheis, M.D. Sturge, and J. Hegarty, Appl. Phys. Lett. **47**, 995 (1985).
88. L. Schultheis, J. Kuhl, A. Honold, and C.W. Tu, Phys. Rev. Lett. **57**, 1635 (1986).
89. L. Schultheis, A. Honold, J. Kuhl, and C.W. Tu, Phys. Rev. B **34**, 9027 (1986).
90. A. Honold, L. Schultheis, J.Kuhl, and C.W. Tu, Appl. Phys. Lett. **52**, 2105 (1988).
91. A. Honold, L. Schultheis, J. Kuhl, and C.W. Tu, Phys. Rev. B **40**, 6442 (1989).
92. L. Schultheis, J. Kuhl, A. Honold, and C.W. Tu, Phys. Rev. Lett. **57**, 1797 (1986).
93. E.O. Göbel, K. Leo, T.C. Damen, J. Shah, S. Schmitt-Rink, W. Schäfer, J.F. Müller, and K. Köhler, Phys. Rev. Lett. **64**, 1801 (1990).
94. D.S. Kim, J. Shah, J.E. Cunningham, T.C. Damen, W. Schäfer, M. Hartmann, and S. Schmitt-Rink, Phys. Rev. Lett. **68**, 1006 (1992).

95. D.S. Kim, J. Shah, J.E. Cunningham, T.C. Damen, S. Schmitt-Rink, W. Schäfer, Phys. Rev. Lett. **68**, 2838 (1992).
96. D.S. Kim, J. Shah, T.C. Damen, W. Schäfer, F. Jahnke, S. Schmitt-Rink, and K. Köhler, Phys. Rev. Lett. **69**, 2725 (1992).
97. T. Yajima and Y. Taira, J. Phys. Soc. Jpn. **47**, 1620 (1979).
98. C. Stafford, S. Schmitt-Rink, and W. Schäfer, Phys. Rev. B **41**, 10000 (1990).
99. N. Bloembergen, *Nonlinear Optics* (Benjamin, New York 1965).
100. F.D. Colegrove, P.A. Franken, R.R. Lewis, and R.H. Sands, Phys. Rev. Lett. **3**, 420 (1959).
101. R.L. Shoemaker and R.G. Brewer, Phys. Rev. Lett. **28**, 1430 (1972).
102. V. Langer, H. Stolz, and W. von der Osten, Phys. Rev. Lett. **64**, 854 (1990).
103. Y.R. Shen, *The principles of Nonlinear Optics* (John Wiley, New York 1984).
104. K. Leo, E.O. Göbel, T.C. Damen, J. Shah, S. Schmitt-Rink, W. Schäfer, J.F. Müller, K. Köhler, and P. Ganser Phys. Rev. B **44**, 5726 (1991).
105. G. Bastard, *Wave Mechanics Applied to Semiconductor Heterostructures* (Edition de Physique, les Ulis, France 1988).
106. K. Leo, M. Wegener, J. Shah, D.S. Chemla, E.O. Göbel, T.C. Damen, S. Schmitt-Rink, and W. Schäfer, Phys. Rev. Lett. **65**, 1340 (1990).
107. D.S. Chemla, D.A.B. Miller, and P.W. Smith in: *Semiconductors and Semimetals: Applications of Multiquantum Wells, Selective Doping, and Superlattices*, ed. R. Dingle, p. 279 (Academic, San Diego 1987).
108. J.M. Hays (private communication).

APPENDICES

APPENDIX A

REMOVING THE GaAs SUBSTRATE

In order to perform some of the transmission measurements the GaAs substrate had to be removed from the SL and QW samples. This is done by selective wet etching in a hydrogen peroxide solution. The details of this procedure is the main subject of this appendix.

The SL sample and a sapphire substrate (or a piece of microscope glass) are degreased and cleaned in a trichloroethylene solution. We use an epoxy (Norland NOA-61) to glue the sample down on the sapphire substrate with the SL surface facing down on the sapphire. It is important to move the sample around on the sapphire to make sure there are no air bubbles between the sapphire and the SL area. The epoxy is then exposed to UV light from a Xenon lamp for about 20 to 30 minutes. For final curing of the epoxy, the sample is left under a regular desk lamp overnight (about 12 hrs or more). Note that after curing the thickness of the epoxy is estimated to be between 2-15 μm .

Once the sample is firmly attached to the sapphire piece, we proceed by polishing the GaAs substrate down to a thickness of about 100 to 200 μm using aluminum-graded polishing paper. For the final polishing, we used a diamond paste of 1 μm grit size to obtain a nice smooth surface. The sample and sapphire are cleaned with deionized water and gently wiped off with a lens paper soaked with acetone. It is important to note that our epoxy is dissolvable in acetone and care must be taken not to apply too much of it on the sample. If necessary, we can trim down the excess cured epoxy around the sample with a razor blade. At this point we are ready to apply photoresist to the areas that we want to protect from etching. The protected areas are the surrounding edges of the sample and the epoxy (see Figure 12 in Chapter III). The sample is then placed under a desk lamp

for at least 4 to 6 hours to allow photoresist to cure. We also note that photoresist should be kept in a fairly dark area in order for it to preserve its properties.

At this point we mix the etching solution which will be referred to as PA30. This solution contains a 30:1 to 25:1 mixture of hydrogen peroxide (H_2O_2) and ammonium hydroxide (NH_4OH) respectively. It is important to note that the solution is corrosive and one must avoid skin contact. The typical solution volume used was about 100-150 ml in a 250 ml glass container. The samples are placed on the bottom of the container with a stirrer magnet to the side. The typical stirring speed used is about 3-5 on the scale of our VWR magnetic stirrer model 320. Care is taken to occasionally remove air bubbles from the etching surface of the sample. We also rotate the sample every 10 mn or so for a more uniform etch. Every once in a while the sample surface is checked under the microscope without removing the sample from the solution. Usually some oxidation (i.e. white patches) appear on the surface of the sample. This oxidation can be removed by a slow etching solution called semico-clean. This last step can be performed as often as needed. However, it is important to note that whenever the sample is taken out of the etching solution it must be dipped immediately in deionized water for rinsing. The etching time usually takes between 2 to 3 hours per sample depending on the substrate thickness and the pH of the etching solution. The last 30 minutes of the etching process are very crucial to the success of the operation and the sample surface must be constantly monitored. This is because of the fact that GaAs etches very fast in PA30 and one has to stop the etching process immediately after a smooth and shiny brown surface appears on the sample. This surface is usually that of AlAs or $Al_xGa_{1-x}As$ etch stop layer (see Figure 3 in Chapter II) and beyond it there is the SL layers. After performing this procedure several times, we have obtained an estimated of about $1.6 \mu m/mn$ for our etching rate .

APPENDIX B

DETAILS ON THE PUMP AND PROBE EXPERIMENT

Pump and probe or two-pulse experiments are generally used in time resolved experiments where the first pulse (pump) creates changes in the sample which are detected by the second pulse (probe). There are several different experiments that employ this technique. Among these is the two beam degenerate-four-wave-mixing (DFWM) experiment used in our study. In this appendix we will try to give some details about the alignment procedure used in these experiments.

In the two beam DFWM experiments, as described in Chapter III, the pump and probe pulses propagating along the \mathbf{k}_1 and \mathbf{k}_2 directions interact coherently inside the sample. This interaction results in the creation of a transient polarization grating which self-diffracts part of the probe beam into the background-free direction $2\mathbf{k}_2-\mathbf{k}_1$. The experimental setup used for these experiments is shown in Figure 10 of Chapter III. Figure 38 shows schematically the pump and probe configuration of our DFWM experiments. The time resolution of these experiments comes from the time delay (T) between the pump and probe pulses. Thus, the resolution of these experiments is mainly limited by the duration of the laser pulses used. In our case we use subpicosecond pulses on the order of 150 fs duration to perform these experiments. This allows for a high temporal resolution but also introduces some difficulties in the technical aspect of the experiment.

In our alignment procedure, at first, we spatially overlap the pump and probe pulses on the sample. Since the pulses are very short in time and focused to a very small spot (on the order of about 50 μm) extra care must be taken to insure that their spatial overlap is close to perfect. We found that the best way to do this is by using a small pinhole (about 50 μm in diameter) in place of the sample and observe the interference pattern as each beam is aligned to go through the pinhole.

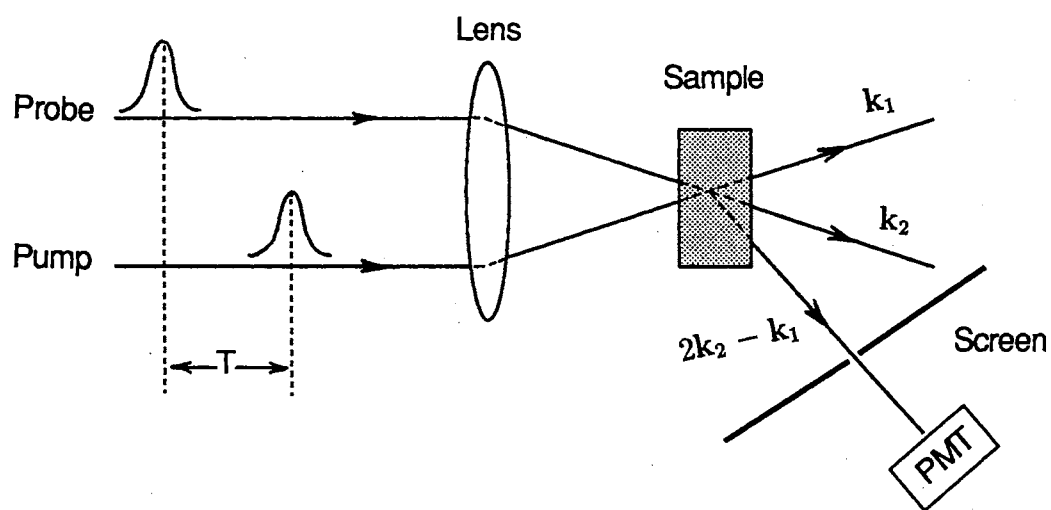


Figure 38. A schematic diagram of the pump and probe configuration used in our DFWM experiments

It is important to note that in the first setup of this experiment, the pump and probe path lengths were matched to within a few centimeters. The exact matching of the pump and probe beam path lengths is, then, controlled precisely by the delay line introduced in the probe beam path. This consists of a precise translation stage that holds two mirrors (or a corner-cube) which reflect the probe beam. By adjusting the translation stage we can accurately adjust the path length traveled by the probe beam and control the arrival time (or delay time T) of the probe pulse with respect to the pump pulse. The smallest step possible on our computer controlled delay line was carefully measured and corresponds to about 11 fs.

In order to completely overlap our pump and probe pulses in time we use a BBO crystal in place of our sample. We, then, adjust the probe delay time and observe the non-collinear second harmonic generation of our pump and probe pulses when they are perfectly overlapped in time. At this point we are ready to introduce our sample in place of the BBO crystal and find our DFWM signal. As shown in Figure 38 the signal is diffracted at an angle from the direction of the probe beam. This diffraction angle is similar to that between the pump and probe beams. We, therefore, estimate where the signal should be and place our detector (PMT) in that position. Note that the pump and probe pulses are blocked by a dark screen just after the sample to reduce the background light. At this point we adjust the wavelength of our laser pulses to match an electronic resonance of the sample. Depending on the sample used, in principle we should be able to observe the DFWM signal at this point. If the signal is not observed we usually can adjust the sample position to make sure that the pump and probe beams are overlapped in the sample. This is some times difficult to accomplish since our samples are only 1 μm to 2 μm thick usually. Once the signal is observed, we can optimize its intensity by adjusting the PMT as well as the sample positions.

The sheet carrier densities are estimated using the following approximate formula

$$n_e \simeq \frac{1}{2} \cdot \frac{\alpha P}{A f \hbar \omega} \cdot L_z$$

Where A is the laser spot area on the sample, P is the average power at the sample, f is the repetition frequency of the laser, ω is the frequency of the laser light, and α is the absorption coefficient which is given as follow for GaAs

$$\alpha(cm^{-1}) \simeq 6.2 \times 10^4 \sqrt{\hbar\omega - E_g}$$

where E_g and $\hbar\nu$ are expressed in eV.

VITA 

ABDELLATIF BOUCHALKHA

Candidate for the Degree of

Doctor of Philosophy

Thesis: PICOSECOND AND SUBPICOSECOND OPTICAL PROPERTIES
OF GaAs/Al_xGa_{1-x}As QUANTUM WELLS AND SUPERLATTICES

Major field: Physics

Biographical:

Personal Data: Born in Marrakech, Morocco, January 1, 1962, the son of Boujemaa and Fatna Bouchalkha.

Education: Graduated from Abou El Abbas Essebti High School, Marrakech, Morocco, in May, 1980; received Bachelor of Science degree in Physics/Math-minor from Central State University, Edmond, Oklahoma, in May, 1986; received Master of Science Degree in Physics at Oklahoma State University, Stillwater, Oklahoma, in July, 1989; completed the requirements for the Doctor of Philosophy Degree at Oklahoma State University, Stillwater, Oklahoma in May, 1993.

Professional Experience: Undergraduate Research Assistant, Central State University, Edmond, Oklahoma, August, 1985 to May, 1986; Teaching Assistant, Department of Physics, Oklahoma State University, August, 1986 to May, 1987; Graduate Research Assistant, Department of Physics and University Center for Laser Research, June, 1987 to present; Member of the American Physical Society, and SPIE-The International Society for Optical Engineering.